Methods and microfabrication techniques for subnanoliter magnetic resonance spectroscopy

THÈSE N^{O} 8006 (2017)

PRÉSENTÉE LE 16 OCTOBRE 2017
À LA FACULTÉ DES SCIENCES ET TECHNIQUES DE L'INGÉNIEUR
LABORATOIRE DE MICROSYSTÈMES 1
PROGRAMME DOCTORAL EN MICROSYSTÈMES ET MICROÉLECTRONIQUE

ÉCOLE POLYTECHNIQUE FÉDÉRALE DE LAUSANNE

POUR L'OBTENTION DU GRADE DE DOCTEUR ÈS SCIENCES

PAR

Enrica MONTINARO

acceptée sur proposition du jury:

Prof. S. Lacour, présidente du jury
Dr G. Boero, Prof. J. Brugger, directeurs de thèse
Prof. M. Utz, rapporteur
Prof. H. Gardeniers, rapporteur
Prof. H. Shea, rapporteur

ÉCOLE POLYTECHNIQUE
FÉDÉRALE DE LAUSANNE
Suisse
2017

Laci bácsinak, aki
örökké köztünk van.

Acknowledgments

I would like to thank my supervisors, Dr. G. Boero and Prof. J. Brugger, who gave me the opportunity to work in a unique research environment. I have appreciated their scientific guidance, support and encouragement. The members of my thesis committee, Prof. S. Lacour, Prof. H. Shea, Prof. M. Utz, Prof. J.G.E. Gardeniers for their comments and valuable feedback. The staff of the Center for Micro and Nanotechnology (CMI) at EPFL for their availability and helpful discussions. Severine Eggli, Lucie Auberson and Marie Halm for all their support during my studies.

I am grateful to my present and former colleagues and students of the lab for their collaboration and friendship. A special thought goes to Annalisa, Andrea, Mohammad and Thomas for their constant help, fruitful discussions and joyful presence. Enrica and Cristina, for having turned even the most difficult moments into happy memories. I am thankful for their scientific help, prompt assistance and valuable friendship. All the friends I met in Lausanne, in particular Elena, Giulia, Martin and Alessandro for their encouragement, reassurance and great time spent together. Sonia, the best failed tandem ever. She brought me up when I was down. Grazie per esserci stata sempre, per avermi ascoltato, consigliato e supportato. My dearest friends Valeria, Angela, Stefania and Federico who despite the distance where always so close.

Ringrazio mia madre, per la sua sicurezza e consapevolezza, per il suo supporto incondizionato ed il suo infinito amore. Mio padre, silenzioso complice di vita, compagno fedele in questo cammino, per avermi spinto a superare i miei limiti e a vincere le mie paure. Mia sorella, esempio di forza e determinazione, per il suo conforto e la sua meravigliosa presenza. A special thanks to my husband Laszlo for the limitless support, the encouragement, the sincere appreciation, the scientific assistance and helpful discussions, the patience and toleration.

Abstract

Nuclear magnetic resonance (NMR), electron paramagnetic resonance (EPR) and ferromagnetic resonance (FMR) spectroscopy can open up the possibility of studying many scientifically and biologically relevant samples at the μm and sub-μm scale. Examples of volume-limited systems include numerous species of microorganisms, mammalian zygotes, the majority of cells, proteins limited in growth, micro and nanostructured devices for the analysis of spin dynamics at the sub-μm scale.

These volume-limited samples cannot be addressed by commercially available inductive spectrometers due to their constraint in sensitivity. This limitation can be overcome by miniaturizing the dimensions of the detector, thus maximizing the filling factor and increasing the detected signal. It was previously proposed in our group that complementary metal-oxide semiconductor (CMOS) technology can be used to realize miniaturized high sensitivity inductive probes, which use integrated planar coils for both the excitation and detection of NMR and EPR signals. These novel NMR and EPR detection systems have spin sensitivities respectively of 10^{13} spins/$\sqrt{\text{Hz}}$ and 10^{8} spins/$\sqrt{\text{Hz}}$ at room temperature, i.e at least two orders of magnitude better than the commercially available spectrometers.

During my PhD work, I developed methods and microfabrication techniques to perform NMR, EPR and FMR spectroscopy at the μm and sub-μm scale by using these high sensitivity single chip CMOS detectors.

Microfluidic systems for the non-invasive handling of liquid samples and biological entities immersed in liquids were realized and combined with the CMOS single chip NMR and EPR detectors. The sample handling becomes more difficult as the size of the detector is scaled down. The extremely small detection volumes (approximately 0.2 nL) set constraints for the fabrication of microfluidic systems, with designs that enable the precise driving and trapping of the specimen in close proximity of the integrated coil and materials that guarantee a seal of the microfluidic structure. The implementation of separation layers below 10 μm between the sample and the microcoil, allows for delivering acceptable filling factors at a small expense in spin sensitivity.

Microfluidic channels were fabricated via conventional microfabrication techniques and via two-photon polymerization, a 3D printing technique with a lateral resolution of 300 nm. The former method is suitable for large scale production and for applications where there is no need of a 3D design and the resolution limit of photolithography is not a concern. The latter method is the ideal solution for the rapid prototyping of complex microfluidic devices for the trapping and culturing of biological entities of different sizes and fluidic beaviours.

We demonstrated that the 3D printing technique is an exceptional solution for NMR applications. Due to the flexibility in the design of the microfluidic systems, it is possible to minimize the dead

volume, essential for NMR experiments on volume-limited liquid samples. It is also possible to reduce the magnetic field non-uniformieties with a consequent improval in spectral resolution. We reported spectral resolutions down to 0.007 ppm for liquids having sample volumes of 100 pL.

Using 3D printed microfluidic systems we performed, for the first time, NMR studies on intact biological entities (specifically on ova of the tardigrade *Richtersius coronifer* and sections of adult *Caenorhabditis elegans* worms) submerged in liquid media of choice. We show a sensitivity of $2.5 \cdot 10^{13}$ spins/$\sqrt{Hz}$, sufficient to detect highly concentrated endogenous compounds in active volumes down to 100 pL with measurement times down to 3 h.

We showed the first example of EPR measurements on subnanoliter liquids and frozen solutions, by the combination of commercially available capillaries and EPR single chip detectors. This is a first but important step towards the study of biological samples, whose paramagnetic ions have relaxation times too short to be measured at room temperature. The same single chip detector was used to perform FMR experiments at the μm and sub-μm scale.

Moreover, we reported a novel method for the sensing of magnetic microbeads, which is based on the detection of the change of susceptibility in FMR condition by the CMOS integrated detector. Due to the frequency and field dependence of the susceptibility, the detected variation is 20 times greater than the change in magnetization measured in static conditions by other approaches. The proposed detection scheme allows for single bead sensitivity over a sensing area of about $5 \cdot 10^4$ μm^2. This is an improvement with respect to other magnetic beads detection techniques, which suffer either from limited sensitivity or from reduced sensing area.

Lastly, sub-μm scale FMR detection capabilities of the single chip CMOS detector are shown by experiments on nanopatterned single permalloy ($Ni_{80}Fe_{20}$) and YIG ($Y_3Fe_5O_{12}$) dots. As for the detection of magnetic beads, the combination of high sensitivity and large sensing area is seen as a considerable advantage with respect to other FMR detection methods.

In summary, in this thesis we report the methods and fabrication techniques developed to perform NMR of subnanoliter liquids and biological samples submerged in liquids, as well as EPR of liquids and frozen solutions at the sub-nL scale. Morever we show a new method for the detection of magnetic microbeads based on the sensing of the change of susceptibility in FMR condition. Lastly, we present the nanopatterning of NiFe and YIG films and the FMR measurements of the realized structures by a single chip CMOS detector.

Keywords

Microscale nuclear magnetic resonance, electron paramagnetic resonance, ferromagnetic resonance, subnanoliter NMR, subnanoliter EPR, sub-μm scale FMR, microfluidic channels, two-photon lithography, 3D printing.

Riassunto

I fenomeni di risonanza magnetica nucleare (NMR), risonanza paramagnetica elettronica (EPR) e risonanza ferromagnetica (FMR) possono essere utilizzati per analizzare diversi campioni di volume inferiore al nanolitro, di grande interesse nell'ambito scientifico e biologico. Alcuni esempi di sistemi a volume limitato sono la maggior parte delle cellule, numerose specie di microorganismi, zigoti di mammifero, proteine difficili da sintetizzare in grandi volumi, dispositivi micro e nanostrutturati per l'analisi delle dinamiche di spin nella scala di frazioni di μm.

Tuttavia, questi campioni a volume ridotto non possono essere analizzati da spettrometri attualmemte disponibili in commercio, i quali presentano una limitata sensitività. Questa limitazione può essere superata miniaturizzando le dimensioni del rivelatore, massimizzando così il fattore di riempimento e aumentando il segnale rilevato. In precedenza nel nostro gruppo di ricerca è stato dimostrato che la tecnologia CMOS (complementary metal-oxide semiconductor) può essere utilizzata per realizzare sonde miniaturizzate ad alta sensitività. Tale sonde sono dotate di bobine planari integrate che permettono l'eccitazione e la rilevazione del segnale NMR ed EPR. Questi nuovi sistemi di rilevamento hanno sensitività, a temperature ambiente, rispettivamente di 10^{13} spin/$\sqrt{\text{Hz}}$ and 10^{8} spin/$\sqrt{\text{Hz}}$ – almeno 2 ordini di grandezza superiore a quella degli spettrometri esistenti in commercio.

Durante il mio dottorato, ho sviluppato metodi e tecniche di microfabbricazione per eseguire la spettroscopia NMR, EPR e FMR alla scala μm e sub-μm usando questi rivelatori CMOS ad alta sensitività.

Sistemi microfluidici per la manipolazione non invasiva di campioni liquidi e entità biologiche immersi in liquidi sono stati realizzati e integrati con i rivelatori CMOS di NMR e EPR. Con la riduzione della dimensione del rivelatore, la gestione del campione si compica notevolmente. I volumi di rilevamento estremamente ridotti (circa 0,2 nl) determinano vincoli per la fabbricazione di sistemi microfluidici, con strutture che consentano una precisa conduzione e il blocco del campione in prossimità della bobina integrata, nonché materiali che garantiscano un'impermeabilizzazione della struttura microfluidica. L'implementazione di strati di separazione inferiori a 10 μm tra il campione e la micro bobbina, consente di ottimizzare il fattore di riempimento e minimizzare la perdità in sensitività rispetto al caso ideale del campione in diretto contatto con la micro bobina.

I canali microfluidici sono stati fabbricati sia con tecniche convenzionali di microfabbricazione che mediante polimerizzazione a due fotoni, una tecnica di stampa 3D con risoluzione laterale di 300 nm. Il primo metodo è adatto per produzioni su larga scala e per applicazioni dove non è necessaria una struttura 3D. Il secondo metodo è la soluzione ideale per realizzare rapidamente complessi

dispositivi microfluidici per la cattura e la coltivazione di entità biologiche aventi diverse dimensioni e comportamenti fluidici.

In questo lavoro di tesi è stato dimostrato che la tecnica di stampa 3D ad alta risoluzione è una soluzione eccezionale per applicazioni NMR. Sfruttando la flessibilità nella progettazione dei sistemi microfluidici, è possibile minimizzare il dead volume, parametron essenziale per gli esperimenti NMR su campioni liquidi a volume limitato. È inoltre possibile ridurre le disuniformità del campo magnetico con conseguente miglioramento della risoluzione spettrale. Abbiamo riportato risoluzioni spettrali fino a 0,007 ppm per liquidi aventi un volume di 100 pL.

Utilizzando i sistemi microfluidici stampati con tecnologia 3D abbiamo eseguito inediti studi NMR su entità biologiche intatte (in particolare su ovuli di tardigrado *Richtersius coronifer* e sezioni di *Caenorhabditis elegans* adulti) immerse in liquidi. Mostriamo una sensitività di $2.5 \cdot 10^{13}$ spin/$\sqrt{\text{Hz}}$, la quale è sufficiente a rilevare composti endogeni altamente concentrati in campioni con volumi fino a 100 pL e con tempi di misura fino a 3 ore.

Abbiamo realizzato il primo esempio di misure EPR su liquidi con volume inferiore al nanolitro e soluzioni congelate, mediante la combinazione di capillari esistenti in commercio e rivelatori EPR integrati su singoli chip CMOS. Questo è un primo passo verso lo studio di campioni biologici, i cui ioni paramagnetici hanno tempi di rilassamento troppo brevi per essere misurati a temperatura ambiente. Lo stesso rivelatore CMOS è stato utilizzato per eseguire esperimenti FMR con scala μm e sub-μm.

In questo manoscritto viene presentato un nuovo metodo per la detezione di microbiglie magnetiche che si basa sulla misura della variazione di suscettività in condizioni di FMR da parte del rilevatore integrato CMOS. Sfruttando la dipendenza della suscettività dalla frequenza e dal campo magnetico, la variazione rilevata è 20 volte maggiore rispetto alla variazione della magnetizzazione misurata in condizioni statiche da altri metodi presenti in letteratura. Questo nuovo sistema di rilevamento consente di raggiungere una sensitività di una singola microbiglia su un'area sensibile di circa $5 \cdot 10^4$ μm^2. Questo è considerato un vantaggio rispetto ad altre tecniche di detezione di biglie magnetiche, che sono limitate o dalla sensitività o da una ridotta area sensibile.

Infine, é stata dimostrata con esperimenti su singoli nanodot di permalloy ($Ni_{80}Fe_{20}$) e YIG ($Y_3Fe_5O_{12}$), la capacità di detezione FMR del rilevatore CMOS su scala sub-μm. La combinazione di alta sensitività e di ampia area sensibile è da considerarsi un notelove vantaggio rispetto ad altri metodi di detezione FMR.

In questa tesi sono riportati metodi e tecniche di fabbricazione sviluppate per eseguire misure NMR su liquidi e campioni biologici immersi in liquidi con volume inferiore al nanolitro, così come misure EPR su liquidi e soluzioni congelate con scala sub-nL. Viene presentato un nuovo metodo per la detezione di microbiglie magnetiche basate sulla misura della variazione di suscettività in condizioni di FMR. Infine viene presentata la nanostrutturazione di film di NiFe e YIG e la misura FMR di tali strutture effettuata dal rilevatore CMOS integrato su singolo chip.

Parole chiave

Risonanza magnetica nucleare, risonanza elettronica paramagnetica, risonanza ferromagnetica, NMR su scala sub-nL, EPR su scala sub-nL, FMR su scala sub-μm, canali microfluidici, litografia a due fotoni, stampa 3D.

Contents

List of Figures

Chapter 1 Introduction

1.1 Introduction

Nuclear magnetic resonance (NMR) and electron paramagnetic resonance (EPR) spectroscopy are powerful techniques widely used in physics, chemistry, medicine and biology. They are often the method of choice for the non-invasive extraction of detailed chemical information from a variety of samples. NMR spectroscopy allows profiling of multiple metabolite concentrations in living matter and their cellular variation in response to drugs, environment, stimuli, lifestyle. It enables metabolic profiling to reveal latent phenotypes and the determination of a representative set of protein structures, even acquired exclusively from living cells[3-20]. EPR spectroscopy provides information on local structure of large molecules by measuring long-range intermolecular distances on the nanometer scale. It permits to understand the details of the dynamics in proteins, to study in vivo pathological effects related to the presence of free radicals and to map oxygenation in living tissues[21-35].

1.2 State of the art

1.2.1 Microscale NMR

Nuclear magnetic resonance (NMR) is a powerful technique widely used in physics, chemistry, medicine and biology[36-38]. During an NMR experiment the sample is immersed in a static magnetic field and excited with electromagnetic fields at frequencies and strengths which have no biological sideffects. Due to this property and to its resolving power, NMR is successfully applied to a variety of applications, e.g., to diagnostic imaging[39] and in-vivo spectroscopy[40-42] of large living animals. The extension of NMR towards the microscopic scale is hindered by sensitivity limitations. However, the search for methods enabling this powerful technique at small scale is an active domain of research[43-46].

Various techniques permitted the optimization of NMR tools for volume scales ranging from 1 µL down to a few nL[43, 46-57]. Some of these techniques were used to perform unique pioneering studies of small collections of cells and microorganisms[12, 13, 55, 58], perfused tumor spheroids[59], and large single cells and embryos[6-8, 60-63]. NMR-based studies of intact single biological entities were, until recently, demonstrated down to volumes of 5 nL and limit of detection (LOD), reported to a field strength of 600 MHz, down to 10 nmol $s^{1/2}$ of ^{1}H spins[8, 55, 58]. Further reducing the volume of detection would open up the possibility of studying many biologically relevant systems present at the subnanoliter scale, which include the majority of cells, numerous species of microorganisms

and mammalian zygotes[64]. The main limitation in addressing sub-nL biological samples is given by the required spin sensitivity, being both a volume and concentration limited problem.

Conventional inductive NMR spectrometers are optimized for having volumes of few hundreds of μL and achieve sensitivities of 10^{15} spins/$\sqrt{Hz}$. Due to their intrinsic poor senstitivity, the investigation of subnanoliter samples is impossible. Given the broad range of applications, the development of techniques aimed at increasing the spin sensitivity of NMR is a scientific and technological hot topic. A candidate approach for fulfilling this goal is high sensitivity inductive MR probes based on microcoils or microresonators, whose small size is necessary to maximize the sensitivity of the detector[51, 56, 57, 65-73]. While the possibility to extend MR towards manually placed subnanoliter solid samples was already demonstrated[2, 68, 74], MR spectroscopy of subnanoliter liquid volumes and biological entities in a liquid environment is challenged by the need of placing and holding liquids at the sensitive region of the miniaturized detector.

A promising solution for achieving this target is the combination of miniaturized inductive probes and a microfluidic system. To this end, several approaches towards the miniaturization of coils and their integration with microfluidics were reported[75-80]. In one approach, solenoids were constructed manually, by hand-winding copper wires around capillary tubes[75, 77]. Such a manual approach is poorly reproducible and difficult to scale down. Subsequently, various microfabrication techniques were developed to shrink the size of the solenoids. Solenoids on micro-capillaries were microfabricated using microcontact printing and electroplating[76], laser lithography[78, 80], focused ion beam[81], SU-8 patterning and electrodeposition[82]. Solenoids on hollow micropillars were fabricated by wire bonding techniques[73, 83].

The main limitations of the solenoidal microcoils are related to their complex fabrication and challenging integration with chip-based microfluidics. To overcome these limitations, planar and Helmholtz microcoils were directly combined with microfluidic structures. Electroplated microcoils were integrated on glass[84, 85] or silicon[86] substrates with etched microfluidic channels for sample holding. In another approach, Helmholtz microcoils were included in SU-8 microchannels defined with photolithography[82]. To address subnanoliter samples, the detector coil has to be further miniaturized to match the sample size, thus increasing the filling factor and maximizing the sensitivity of the detectors. Scaling down the microcoil and the integrated microfluidic structures could be feasible with traditional microfabrication methods but it would considerably increase the complexity of the fabrication procedure.

Another approach to microscale NMR is the use of striplines or microslots, a good alternative in terms of field homogeneity, ease of scalability and integration with microfluidics[46, 51, 56, 57, 72, 87, 88]. A limit of detection (LOD), reported to a field strength of 600 MHz, of 1.57 nmol $s^{1/2}$ of ^{1}H spins with active volumes of 2 μL and of 390 pmol $s^{1/2}$ of ^{1}H spins with active volumes of 10 nL was obtained respectively with striplines[89] and microslots[51].

It was previously reported that complementary metal-oxide semiconductor (CMOS) technology can be used to realize a NMR miniaturized high sensitivity inductive probe[74]. This integrated system uses an integrated planar microcoil for both the excitation and the detection of the magnetic resonance signals and is optimized for the detection of sample volumes of 200 pL.

This technique has potential advantages over the conventional inductive detection technique. NMR microcoils with a large number of turns within a radius of less then 100 μm can be integrated on chip, improving considerably the detector sensitivity over subnanoliter volume. Moreover, the planar geometry of the detector coil facilitates the interfacing of microfluidic structures which permits the driving of the sample in proximity of the most sensitive area of the integrated coil. Furthermore, this approach is compatible with an implementation of an array of detectors that can be placed in the same magnet for simultaneous measurements on several samples.

1.2.2 Microscale EPR

Even in the case of electron paramagnetic resonance (EPR), whose spin sensitivity is far superior to NMR, a major drawback is the relatively low sensitivity compared to other methods. Commercial EPR spectrometers achieve spin sensitivities of about 10^{10} spins/$\sqrt{Hz}$ at 300 K.

There are many applications that require investigation of micron-size samples, such as the detection of free redicals in single cells and measurements of volume-limited samples, e.g. proteins which cannot be grown in large volumes[90]. To address microscale volumes, the improvement of conventional inductive techniques[68, 91, 92] is extensively investigated. For a given sample, spin concentration and applied static magnetic field, the sensitivity mainly depends on the quality factor (Q) of the microwave resonator and the filling factor (η). Recommended devices for the detection of microscale volumes are microwave resonators with high Q and small physical size to maximize the η of the sample. It is possible to further push the sensitivity of the inductive-detection EPR by working at higher static field [90, 93].

The use of small solenoids[65, 94, 95], planar coils[66, 67, 96] and ferroelectric inserts inside standard cavities[97] enabled reaching sensitivities down to 10^9 spins/$\sqrt{\text{Hz}}$. Dielectric resonators with miniaturized features[68, 98, 99] allowed for sensitivities down to 3 x 10^8 spins/$\sqrt{\text{Hz}}$ for E_0 centers in SiO_2 at 300 K and down to 7000 spins/$\sqrt{\text{Hz}}$ for phosphorus doped ^{28}Si at 10 K.

The positioning of the sample becomes challenging when operating with miniaturized resonators, where the precise placing of the specimen in close proximity of the detector is crucial. Few attempts to integrate microfluidics with EPR resonators were reported, involving volumes down to 1 μL[100]. Further reducing this volume would be beneficial for EPR analysis of single biological entities, enabling a non-destructive and non-invasive sample handling and providing a biocompatible liquid environment for the duration of the experiment. Moreover, EPR studies of volume-limited liquid samples would be possible.

Previous works have demonstrated the use of complementary metal-oxide semiconductor (CMOS) technology to realize EPR miniaturized high sensitivity inductive detectors. These integrated systems, whose operation principles are explained elsewhere[2, 92, 101, 102], use integrated planar microcoils for both the excitation and the detection of the EPR signal. Their integrated microcoils have a typical diameter of about 200 μm. Despite the significantly lower Q factor, the spin sensitivity achieved with the single chip method is similar or better than the one achieved with approaches based on miniaturized resonators[68]. Moreover, as mentioned in the previous paragraph, the planar geometry of the detector coil facilitates the interfacing of microfluidic structures for the precise handling of the sample in proximity of the integrated detector. Furthermore, the small size

of each chip and the on-chip direct encoding of the ESR signal would open up the possibility of creating dense arrays of independent detectors for simultaneous measurements.

1.3 Theory

The aim of this thesis is to develop methods and microfabrication techniques to perform micro and nanoscale magnetic resonance experiments using NMR and EPR single chip detectors. The NMR and EPR integrated detector microcoils are characterized by a non-uniform sensitivity that decreases with the distance from the coil and does not have cilindrical symmetry with respect to the coil axis. For this reason, the proximity of the sample with the detector coil is essential to exploit the maximum sensitivity of the detector. In the following paragraphs, we report the theory to derive the signal contribution and quantify the dependence of the local sensitivity as a function of the distance from the center of the NMR and EPR integrated microcoils.

1.3.1 NMR single chip detector: evaluation of the signal contribution

The CMOS single chip NMR detector consists of a RF power amplifier, a RF low-noise preamplifier, a frequency mixer, an audio frequency amplifier and a fully integrated transmit-receive switches. The integrated microcoil is realized using the top four copper metals of the integrated circuit technology; it has 22 turns and an outer diameter of 150 μm. The chip is realized with a 130 nm CMOS technology (STMicroelectronics) and it has a size of about 1 mm^2. Details of the single chip NMR detector are reported in Ref. 74.

As a convention valid throughout the thesis, the planar coil lies in the *yz* plane and the static magnetic field B_0 along the *z* axis (see Fig. 1.1).

Consider a sample, containg nuclei with non-zero magnetic moment. When a static magnetic field B_0 is applied, the nuclear spins precess about B_0 at the Larmor frequency $\omega_0 = -\gamma B_0$, where γ is the gyromagnetic ratio. The macroscopic magnetization M_0 of a sample at temperature T_s, placed in B_0, containing a number of spins N_s per unit of volume, for $kT_s \gg \gamma h B_0/2\pi$ (valid in most of the experimental conditions) is given by[36]

$$M_0 = \frac{N_s \gamma^2 \left(\frac{h}{2\pi}\right)^2 I(I+1) B_0}{3kT_S}. \qquad (1.1)$$

It is possible to exploit a resonant phenomenon by applying a field $2B_{1xy}\cos(\omega_0)$. The orientation of the magnetization M changes, rotating in space with angular frequency $\omega_1 = -\gamma B_{1xy}$. When the oscillating field is turned off, the magnetization relaxes towards its thermal equilibrium condition.

In a simple pulsed NMR experiment, a RF excitation is applied to the sample in a series of short pulses (τ, few μs) and n acquisitions are performed with a repetition time T_R. After an excitation τ, the flip angle Θ between the magnetization and the z axis is $\Theta = \gamma B_{1xy}\tau$. The detection of the NMR signal is carried out by detecting the electromotive force (emf) induced by the nuclear magnetization precession in the integrated microcoil, placed in proximity of the sample. Using the principle of reciprocity[103] and neglecting all the slowly varying terms, the emf induced in the coil per elementary volume dV_s is equal to

$$dS(t,\boldsymbol{r}) = -\frac{d}{dt}\left(\boldsymbol{B}_{uxy}(\boldsymbol{r})\boldsymbol{M}_{xy}(t,\boldsymbol{r})\right)dV_s \quad (1.2)$$

where $\boldsymbol{B}_{uxz}(\boldsymbol{r})$ is the magnetic field at position $\boldsymbol{r}$ produced by the detection coil.

The total electromotive force $S(t)$ induced in the whole sample V_s is equal to

$$S(t) = -\int_{V_s}\frac{d}{dt}\left(\boldsymbol{B}_{uxy}(\boldsymbol{r})\boldsymbol{M}_{xy}(t,\boldsymbol{r})\right)dV_s. \quad (1.3)$$

Consider an ideal pulse excitation (infinitely short pulse, infinitely strong induction field and perfectly resonant). From the ideal pulse solution of the Bloch equation[36, 104] we derive that

$$M_x(t) = -M_0 sin(\Theta) exp\left(\frac{-t}{T_2}\right) sin(\omega_0 t) \quad (1.4)$$

$$M_y(t) = M_0 sin(\Theta) exp\left(\frac{-t}{T_2}\right) cos(\omega_0 t) \quad (1.5)$$

$$M_z(t) = M_0\left(1 - exp\left(\frac{-t}{T_2}\right)(1 - cos\Theta)\right) \quad (1.6)$$

where T_2 is the spin-spin relaxation time.

Consequently, from (1.2), (1.4), (1.5), the signal contribution (*i.e* local sensitivity) $dS(\boldsymbol{r})$ per elementary volume dV_s is proportional to $B_{uxy}(\boldsymbol{r})sin(\Theta)$, where $B_{uxy}(\boldsymbol{r}) = \left(B_{ux}^2 + B_{uy}^2\right)^{\frac{1}{2}}$ is the amplitude of the induction field produced by the coil carrying a unitary current around the point $\boldsymbol{r}$ of the sample.This dependence is used to evaluate the sensitivity of the coil, starting from the computation of $B_{uxy}(\boldsymbol{r})$ via a Biot-Savart based code implemented in Matlab.

Being the flip angle Θ dependent on the pulse lengh τ, the modification of τ implies a variation of the spatial distribution of the sensitivity. It is thus possible to adjust the signal contribution in the volume of interest. As described in details in chapter 2, we fabricated microfluidic channels having different heights and widths. For all the fabricated geometries, considering the sample in direct contact with the 2-µm-thick oxide layer that passivates the microcoil, τ = 2.4 µs maximizes the integrated signal in the sample volume.

Figure 1.1 shows maps of sensitivity of the NMR integrated coil for τ = 3.7 µs, which is the pulse length that maximizes the integrated signal for all the microfabricated microchannels, considering a separation distance between the microcoil and the sample of 10 µm. The black lines show the position in the active volume of the detector microcoil of two biological entities analyzed, i.e. single tardigrade *Richtersius coronifer* ovum (Fig. 1.1a and Fig. 1.1b) and single nematode *Caenorhabditis elegans* worm (Fig. 1.1c and Fig. 1.1d).

Normalizing the total integrated NMR signal $S_{(d=0\mu m)} = 1$ for the ideal case of the channel volume in direct contact with the chip, the signals $S_{(d=10\mu m)}$ and $S_{(d=20\mu m)}$, evaluated in conditions of optimal τ, are respectively 0.7 and 0.5 for all the fabricated microchannels. Thus, for a sample volume placed at a distance of 20 µm from the detector surface, the loss in signal is equal to 50% with respect to the ideal case where the sample is placed in direct contact with the chip surface.

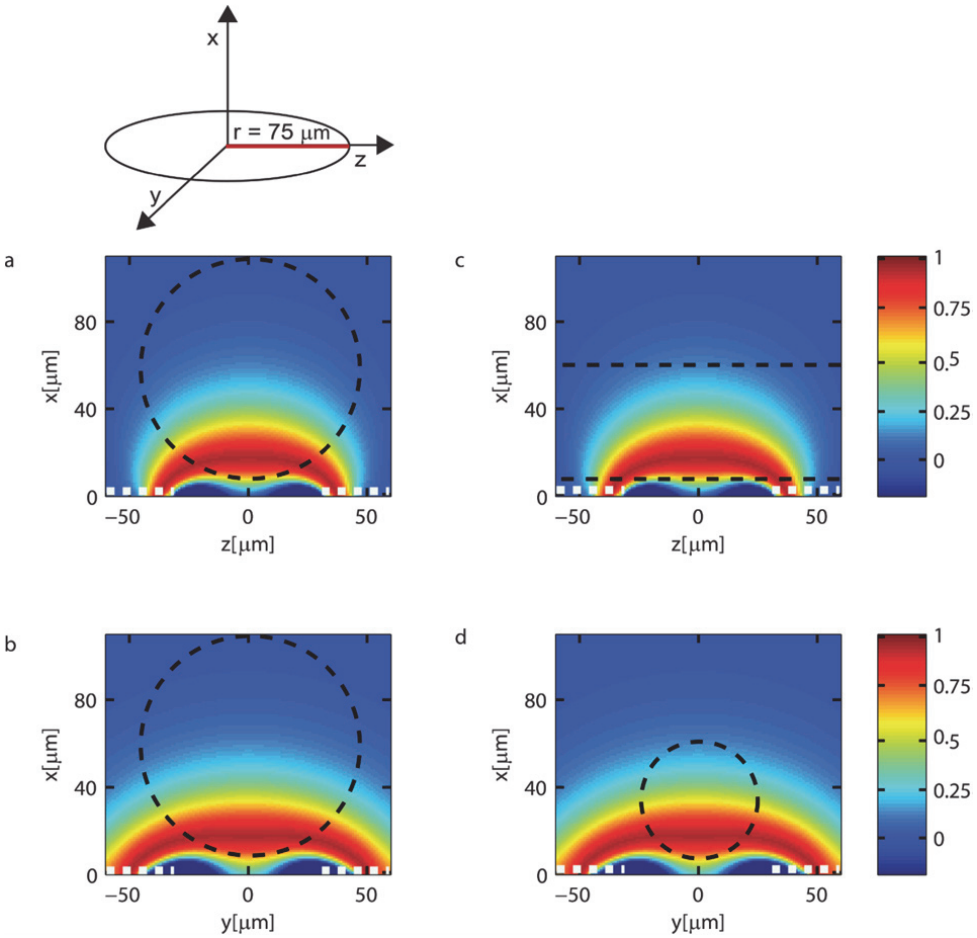

Figure 1.1: Map of the sensitivity for the NMR microcoil computed via a Biot-Savart based code implemented in Matlab. For the NMR microcoil, the local sensitivity is defined as $B_{uxy}(\boldsymbol{r})sin\left(\gamma B_{1xy}(\boldsymbol{r})\tau\right)$, where $B_{1xy}(\boldsymbol{r}) = B_{uxy}(\boldsymbol{r})I$ and I is the current in the coil. The values of local sensitivity are normalized to the maximum value of the signal contribution. The coil has 22 turns, an external radius of 75 µm, and lies in the *yz* plane, the static magnetic field B_0 is along the *z* axis. Sensitivity distribution in the *xz* (a and c) and *xy* (b and d) planes for the integrated NMR coil with excitation parameters τ = 3.7 µs and I = 9 mA. The dashed white lines indicate the position of the coil, while the black dashed lines show the location of the two biological entities analized, i.e *Rc* ovum (a and b) and *C. elegans* subsection (c and d).

A loss in sensitivity of a factor two corresponds to four times longer measurement with respect to the ideal case where the sample is placed in direct contact with the coil. From these observations we can conclude that the precise positioning of the sample in the sensitive volume of the detector is essential to maximize the signal contribution.

1.3.2 EPR single chip detector: evaluation of the signal contribution

The CMOS single chip EPR detector consists of two LC oscillators, a mixer and a frequency divider. The two LC oscillators facilitate the first downconversion of the frequency, which can be performed by a simple mixer instead of a more complicated microwave frequency divider. Being the frequency of the two oscillators 21 GHz and 17 GHz, the frequency after the mixer is equal to 4 GHz. The frequency divider implements a total division ratio of 16, therefore dividing the frequency around 4 GHz to a frequency of about 250 MHz. The chip is realized with a 130 nm CMOS technology (IBM) and has an area of about 1 mm^2. Details of the single chip EPR detector used in the experiments are reported in Ref. 2.

The detection of the EPR signal $S(t)$ is carried out by detection of the change in the frequency of the integrated LC oscillator $\Delta\omega_{LC}$, as a function of the applied static magnetic field B_0. The difference in frequency is due to an effective variation of its coil inductance caused by the resonating complex susceptibility of the sample, as explained in details in Ref. 101.

Consider a planar resonating coil in a static uniform magnetic field B_0 along z axis and a microwave magnetic field $2B_{1xy}\cos(\omega t)$ oscillating at the microwave frequency ω. From the steady state solution of the Bloch equation[105]

$$M_x = M_{x'}cos(\omega t) - M_{y'}sin(\omega t) \quad (1.7)$$

$$M_y = M_{x'}sin(\omega t) + M_{y'}cos(\omega t) \quad (1.8)$$

where

$$M_{x'} = \frac{\Delta\omega\gamma B_{1xy}T_2^2}{1+(T_2\Delta\omega)^2+\gamma^2B_{1xy}^2T_1T_2}M_0 \quad (1.9)$$

$$M_{y'} = \frac{\gamma B_{1xy}T_2}{1+(T_2\Delta\omega)^2+\gamma^2B_{1xy}^2T_1T_2}M_0 \quad (1.10)$$

with $\Delta\omega = \omega - \omega_0$, $\omega_0 = -\gamma B_0$, T_1 is the spin-lattice relaxation time, T_2 is the spin-spin relaxation time.

In condition of non-saturation ($\gamma^2B_1^2T_1T_2 \ll 1$) and introducing a complex susceptibility $\chi = \chi' - j\chi''$ we can write

$$\chi' = -\frac{1}{2}\frac{\Delta\omega T_2^2}{1+(T_2\Delta\omega)^2}\omega_0\chi_0 \quad (1.11)$$

$$\chi'' = -\frac{1}{2}\frac{T_2^2}{1+(T_2\Delta\omega)^2}\omega_0\chi_0. \quad (1.12)$$

Then, (1.7) and (1.8) become

$$M_x = \big(\chi'cos(\omega t) + \chi''sin(\omega t)\big)2H_1 \quad (1.13)$$

$$M_y = \big(\chi'sin(\omega t) - \chi''cos(\omega t)\big)2H_1 \quad (1.14)$$

where $H_{1xy} = \frac{B_{1xy}}{\mu_0}$ and $\chi_0 = \frac{\mu_0 N_s \gamma^2 h^2}{4kT_s}$ is the static susceptibility.

The impedance of a coil filled with a material having susceptibility χ is

$$Z_\chi = j\omega L_\chi + R_\chi \qquad (1.15)$$

where $L_\chi = L + L\eta\chi'$, $R_\chi = R + \omega L\eta\chi''$, L and R are respectively the inductance and the resistance of the coil without the sample, η is the filling factor defined as:

$$\eta = \frac{\int_{V_s} B_{uxy}(\boldsymbol{r})^2 dV}{\int_V B_u(\boldsymbol{r})^2 dV} \qquad (1.16)$$

where V_s is the sample volume and V is the sensitive volume of the detector coil.

Consider $\omega_{LC} = \frac{1}{\sqrt{LC}}$. In typical experimental conditions, we have that:

$\eta\chi' \ll 1$, $\eta\chi'' \ll 1$ and $Q = \frac{\omega_{LC} L}{R} \gg 1$.

Under these conditions, it can be shown[101] that the variation of the oscillator frequency due to the magnetic resonance of the sample is

$$\Delta\omega_{LC} \cong \frac{1}{2}\omega_{LC}\eta\chi'. \qquad (1.17)$$

Being

$$L = \frac{1}{\mu_0}\int_V B_u(\boldsymbol{r})^2 dV, \qquad (1.18)$$

(1.16) can be written as

$$\eta = \frac{\int_{V_s} B_{uxy}(\boldsymbol{r})^2 dV}{\mu_0 L}. \qquad (1.19)$$

Evaluating the signal contribution (*i.e.* local sensitivity) $dS(\boldsymbol{r})$ per elementary volume dV_s and considering $B_{uxy}(\boldsymbol{r})$ uniform over dV_s, from (1.17) and (1.19) the signal contribution $dS(\boldsymbol{r})$ is proportional to $B_{uxy}(\boldsymbol{r})^2$. This dependence is used to evaluate the sensitivity of the coil, starting from the computation of $B_{uxy}(\boldsymbol{r})$ via a Biot-Savart based code implemented in Matlab.

Figure 1.2 shows the map of sensitivity of the integrated EPR coil in the *xz* (Fig. 1.2a) and *xy* (Fig. 1.2b) planes. As described in detail in chapter 3, EPR measurements are performed using commercially available microcapillaries. The black lines show the position in the active volume of the detector microcoil of the liquid sample cointained in the microcapillary used for the EPR experiments.

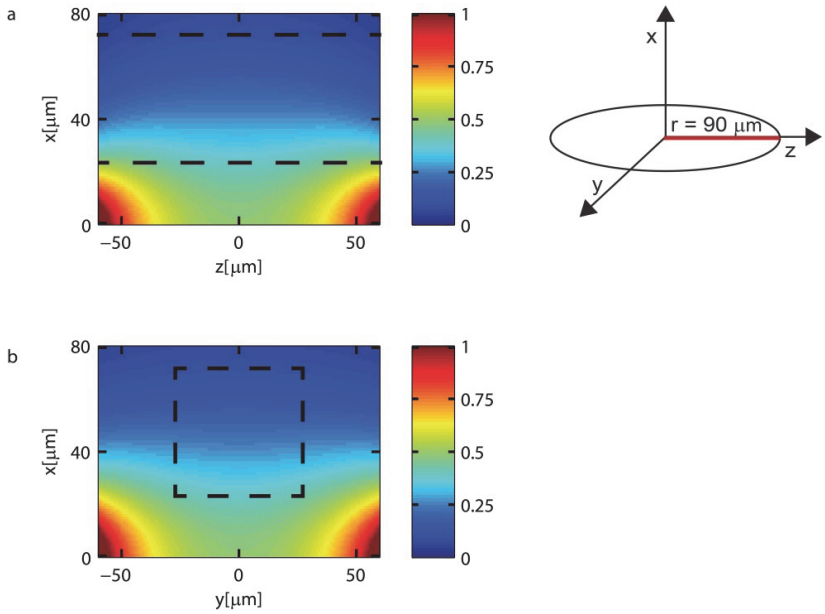

Figure 1.2: Map of the sensitivity for the EPR microcoil computed via a Biot-Savart based code implemented in Matlab. For the EPR microcoil the local sensitivity is proportional to $B_{uxy}(r)^2$. The single turn coil has an external radius of 90 μm and lies in the *yz* plane, the static magnetic field B_0 is along the *z* axis. Sensitivity distribution in the *xz* (a) and *xy* (b) planes for the integrated EPR coil. The black dashed lines indicate the position of the liquid sample cointained in the microcapillary used for the EPR experiments.

Integrating $dS(\boldsymbol{r})$ over the volume of the capillary included in the sensitive volume of the integrated EPR detector, the total sensitivity S can be determined. Considering the sensitivity $S_{(d=0\mu m)} = 1$ for the ideal case of the sample placed in direct contact with the chip, sensitivities $S_{(d=10\mu m)}$ and $S_{(d=25\mu m)}$ are respectively 0.7 and 0.5 for the capillaries employed. Thus, placing a sample at a distance of 25 μm from the surface of the detector, we experience a loss in signal equal to 50% with respect to the ideal case of the sample in direct contact with the detector coil. Also for the EPR integrated microcoil, the proximity of the sample to the detector coil is essential to exploit the volume of maximum sensitivity.

1.4 Goal of the thesis

NMR[74] and EPR[2] CMOS single chip detector opened up the possibility of performing magnetic resonance experiments at the microscale. The goal of this thesis is the development of methods and microfabrication techniques that enable MR spectroscopy of subnanoliter liquids and biological entities immersed in liquids, employing EPR and NMR integrated systems. Furthermore, the possibility of using CMOS integrated systems to detect ferromagnetic resonance (FMR) at the nanoscale is investigated. The limit of sensitivity is explored with FMR measurements of micro and nanostructured ferromagnetic materials.

1.5 Organization of the thesis

The thesis is organized as follow. In chapter 2, I describe the design and microfabrication of microfluidic structures, used to drive subnanoliter liquids and handle biological entities in close proximity of the integrated detection NMR coil. In the same chapter, a collection of ^{1}H NMR spectra obtained from sub-nL liquid samples is shown. The performance of the system is characterized in terms of sensitivity and spectral resolution. NMR measurements of subnanoliter biological entities are also presented. In chapter 3, EPR measurements of subnanoliter liquids and frozen solutions are shown. In chapter 4, FMR detection of single magnetic beads is presented. In chapter 5, the microfabrication processes used to micro and nanopattern ferromagnetic materials is described. In the same chapter FMR measurements of the fabricated structures are shown. Finally, in chapter 6 the conclusions and outlook of this thesis are present.

Chapter 2 NMR spectroscopy of subnanoliter samples

Despite the great potential of nuclear magnetic resonance (NMR), it suffers from relatively low sensitivity compared to other spectroscopic and analytic techniques, such as fluorescence and mass spectrometry. Therefore, investigations of biological entities are often restricted to collections of cells or microorganisms[12, 18, 20, 106, 107].

Individual microorganisms may differ from each other in terms of genetic composition, physiology, biochemistry or behaviour[108]. Observations made at the single-entity level are necessary to study heterogeneous phenomena which cannot be observed at the population-level[4, 109].

NMR experiments of large single cells, embryos and microorganisms were reported down to a volume of 5 nL[6-8, 58, 61-63, 109-111]. However, the typical volumes of most cells, microorganisms and mammalian zygotes are below the nL scale[64].

2.1 Introduction

Ultra-compact CMOS single-chip probes were previously developed as a convenient tools to deliver state-of-art spin sensitivities at sub-nL volumes[74]. Using these devices, NMR experiments on single untouched sub-nL ova were conducted manually placing the biological entities on top of the high sensitive planar microcoils integrated on chip[112].

Despite this study enabled the detection of highly concentrated endogenous compounds, improvements concerning the manipulation of the sample are necessary for the investigation of delicate living subnanoliter entities over longer time and in condition that better approach bio-compatibility. In this aspect, the study of biological samples in liquids would facilitate a non-invasive handling and would provide a more biocompatible environment during the experiments.

The single chip high-sensitivity sub-nL probe, constituted by a multilayer microcoil and a transceiver co-integrated on a CMOS microchip, offers a robust and planar working surface. On the other hand, the exceedingly small detection volume (about 0.2 nL) sets tough fabrication constraints for the microfluidic design, which must maintain the sample in close proximity of the coil and with negligible field distortions.

To overcome these challenges, we developed a solution that employs NMR-compatible microfluidic systems to drive and hold the samples in the sensitive region of the miniaturized detector. We show two different configurations: one is based on SU-8 microfabricated fluidic channels and another on microchannels 3D printed via a two-photon polymerization technique with a lateral resolution of 0.3 μm. Both of the solutions are suitable to implement separation layers below 10 μm between the sample and the microcoil, therefore delivering acceptable filling factors and small loss in terms of spin sensitivity.

Despite traditional microfabrication techniques are more suitable for large scale production, the exceptional versatility of the 3D printed technique is essential for the rapid implementation of microfluidic systems for the handling, trapping and feeding of samples having different sizes and behaviours. Moreover, due to the freedom in the choice of the design, it is possible to implement designs that minimize magnetic field non-uniformities.

To demonstrate the validity of the developed solutions, we report experiments on subnanoliter liquids using the SU-8 and 3D printed microchannels interfaced with the CMOS NMR detector through specific fluidic interfaces. Furthermore, we show the design and the implementation of 3D structured microfluidic systems for the spectroscopy of radically different biological entities, *i.e.* tardigrade *Richtersius coronifer* ova and *Caenorhabditis elegans* worms. Our approach allows for a non-invasive sample handling and an efficient trapping of the living entities during the NMR investigation.

2.2 SU-8 microfluidic channels

The microfluidic system has to provide a stable sealing throughout the duration of the experiments (hours). Polydimethysiloxane (PDMS) cannot be used as microfluidic structural material due to its intrinsic porosity[113], which would make sealing impossible for microchannel walls as thin as 10 μm (thin layers are needed to minimize the sample to detector distance). Another limitation in the use of PDMS is its NMR background signal. The transparency of the fluidic structure is essential for the alignment of the microchannel with the coil.

SU-8 negative epoxy photoresist (Gersteltec) is used as the structural material of microfluidic channels, fabricated to precisely deliver subnanoliter liquid samples onto the integrated detector coil. This material allows for a good sealing of the microfluidic structure, it is transparent and gives flexibility in structuring the channel. The geometry of the channel is designed to exploit the volume of maximum sensitivity, therefore confining the sample in close proximity of the surface of the detector. A 10-μm-thick SU-8 layer separates the liquid specimens from the detector coil (Fig. 2.1); this value is an acceptable compromise between the loss of sensitivity and the fabrication difficulties (see section 1.3.1 for details).

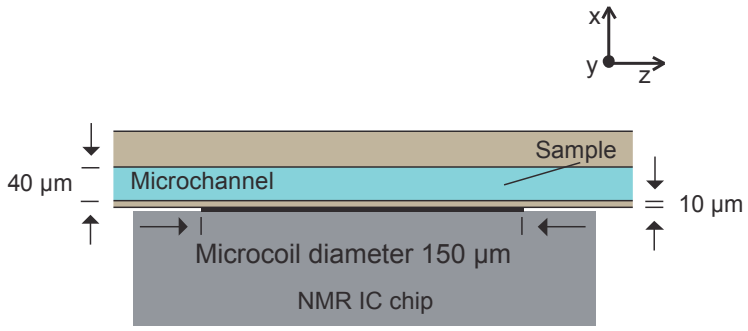

Figure 2.1: Illustration of the approach used to place the liquid sample in close proximity of the most sensitive area of the on-chip excitation/detection microcoil. The coil lies in the *yz* plane with the static magnetic field B_0 along the *z* axis. The microfabricated SU-8 fluidic system is placed on top of the IC chip and aligned with the integrated detector coil. A 10-µm-thick SU-8 layer defines the actual spacing between the sample and the chip surface.

2.2.1 Design and fabrication

The microchannels are fabricated using SU-8 negative epoxy photoresist, a propylene-glycol-monoether-acetate developer (PGMEA, Gersteltec), single-side polished 4 inch <100> silicon (Si) wafers with 525 µm thickness, and 4 inch Borofloat 33 wafers with 500 µm thickness. Photolithography masks are printed on a chromium plate by a direct writer system (VPG 200, Heidelberg Instruments).

The microfabrication process developed to fabricate the microfluidic structure is described in Fig. 2.2. The proposed method is based on the bonding of a Si wafer with photolithographic patterned SU-8 bilayer and a Borofloat 33 wafer with a partially soft baked SU-8 layer.

The fabrication process has increased versatility and reproducibility compared to previous approaches[114-116]. One major improvement is given by the fact that the tedious alignment step before the bonding is not needed, and the bonding quality is largely improved as it is less dependent on subsequent process parameters.

The Si and Borofloat wafers are treated with oxygen plasma to improve the adhesion of the SU-8 films. No further cleaning procedures are needed. For the release of the SU-8 structures, a 500-nm-thick Dextran layer from Leuconostoc (Sigma-Aldrich, 31390-25G) is spin coated onto both the Si and the Borofloat wafers. This sacrificial layer is subsequently dissolved in water, enabling the release of the structures at the end of the fabrication process.

Following the sacrificial layer coating, a 10-µm-thick SU-8 layer is spin coated. For an improved uniformity of the thickness, a relaxation time of 30 min is respected. A drying step (soft bake) is performed at 130 °C for 5 min. The temperature is increased linearly from room temperature at a rate of 4 °C min^{-1}; the same rate is also used for the cooling down of the wafer. The photoresist is then exposed to UV using a Suss MJB4 manual aligner; for the 10-µm-thick SU-8 layer, a 184 mJ cm^{-2} UV exposure dose is used. The post exposure baking is performed gradually increasing the temperature: it is ramped linearly from 30 °C to 90 °C at a rate of 2 °C min^{-1} and kept for 30 min. Then it is slowly decreased at 1 °C min^{-1}.

UV exposure dose and post bake parameters are optimized to ensure a good SU-8 crosslinking, to avoid delamination problems, and to minimize the stress in the SU-8. To finish the photolithography, the Si wafer is developed in PGMEA for 1 min to define the bottom part of the microfluidic structure (Fig. 2.2a).

On the top of the patterned SU-8, a second 40-µm-thick layer of SU-8 is spin coated and subjected to an overnight relaxation to improve the uniformity of the thickness. The soft bake is performed at 90 °C and the exposure dose is 365 mJ cm^{-2}; the post exposure bake is performed at 90 °C for 40 min following the same slow ramp used for the 10 µm layer. The Si wafer is then developed in PGMEA for 3 min to define the walls of the microchannel; the patterning of the SU-

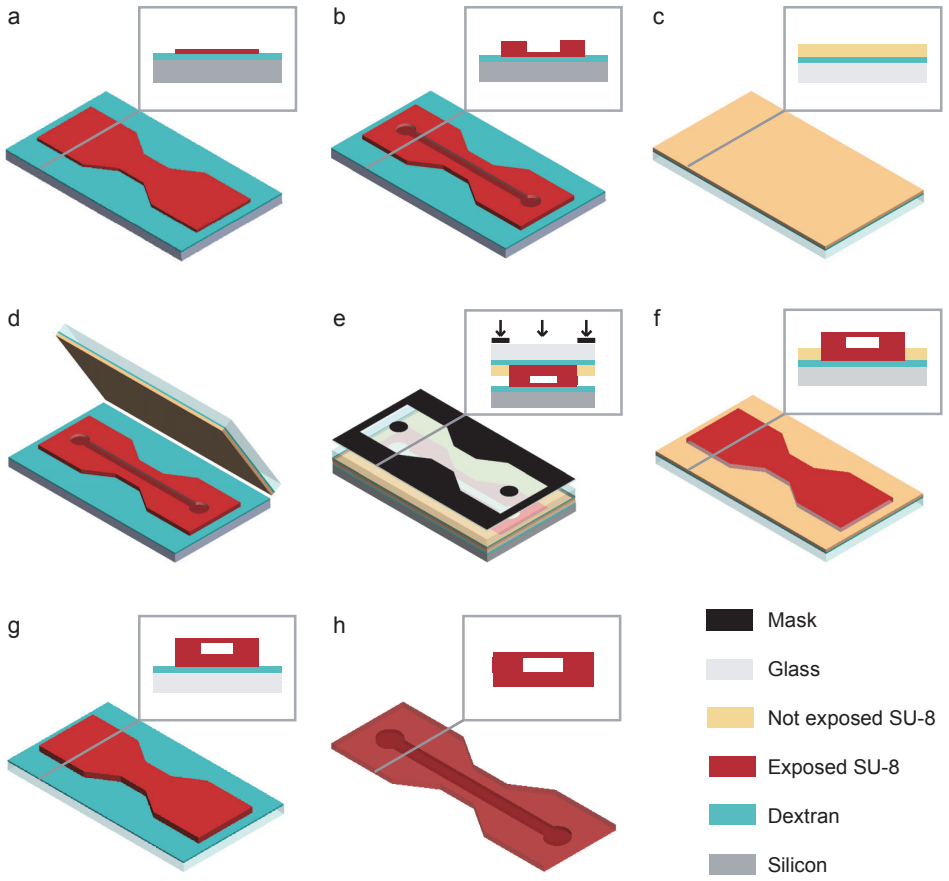

Figure 2.2: Process flow for the fabrication of the SU-8 microchannel. Test grade silicon (Si) wafer <100> and Borofloat 33 glass wafers are used as substrates on which dextran is spin coated as a sacrificial layer for structure release. (a) On the Si wafer a 10-µm-thick layer of SU-8 is patterned to define the bottom part of the microfluidic structure. (b) On the top of the patterned SU-8, a 40-µm-thick layer of SU-8 is spin coated and patterned to create the walls of the microchannel. (c) A 40-µm-thick layer of SU-8 is spin coated onto the glass wafer and partially soft baked. (d) The two wafers are brought into contact at 68 °C, slightly above the glass transition temperature of the non-cross-linked SU-8. (e) The soft bake is continued and the 40-µm-thick layer of SU-8 is polymerized via a UV exposure through the glass wafer to define the structure and the shape of the inlets. The ensemble is again placed on the hotplate to complete the SU-8 processing. (f) The silicon wafer is removed through dextran dissolution in water, (g) the 40-µm-thick SU-8 patterned layer is developed and (h) the final structures are released after dextran removal on the glass wafer.

8 bilayer structure is so created (Fig. 2.2b). To create the sealing layer, a 40-µm-thick SU-8 layer is spin coated onto a Borofloat glass wafer, previously coated with a 500-nm-thick dextran layer (Fig. 2.2c). The SU-8 layer is partially soft baked at 130 °C for 5 min and progressively cooled to 68 °C, slightly above the glass transition temperature of the non-cross-linked SU-8. The resist is pressed into contact with the patterned silicon wafer (Fig. 2.2d) and the soft bake is continued, cooling down to room temperature at the rate of 2 °C min^{-1}. The resist is UV exposed through the glass wafer with the use of a mask to define the inlets and the shape of the sealing layer of the structure (Fig. 2.2e). The ensemble is again placed on the hotplate to perform the post exposure bake at 85 °C for 40 min, following the same small ramp used for the 40 µm layer, described above for the silicon wafer. The silicon wafer is removed through dextran dissolution in water (Fig. 2.2f); the 40-µm-thick SU-8 layer patterned on the glass substrate is developed in PGMEA for 3 min to finish the photolithography (Fig. 2.2g). The final structures are then released with dextran removal from the glass wafer and developed for 3 min to create the inlets of the microchannel (Fig. 2.2h).

Different variables can contribute to the final SU-8 thickness uniformity such as speed and acceleration in the coating process, relaxation time, crosslinking of the resist and structure geometries[115]. For this reason, these parameters have been optimized to obtain a planarity which is needed for a good bonding.

Figure 2.3a shows the complete fabricated microfluidic structure. In Fig. 2.2b, a SEM picture of the microchannel cross section is shown. The good quality of the bonding is confirmed by the lack of a visible interface between the two SU-8 layers. Dummy structures (Fig. 2.2c) are introduced to increase the planarity of the SU-8 layer, thereby improving the quality of the bonding.

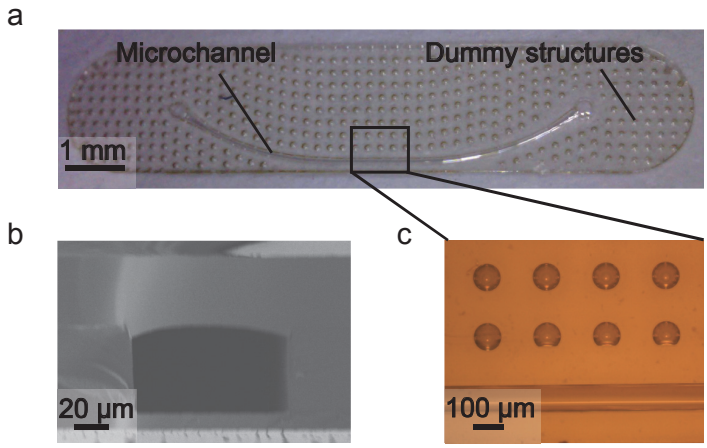

Figure 2.3: Pictures of the SU-8 microfluidic channel. (a) Picture of the SU-8 microchannel. The dummy structures around the SU-8 microchannel are inserted to increase the planarity of the SU-8 layer, thereby improving the quality of the bonding. (b) SEM picture of the SU-8 microchannel cross section. (c) Optical microscope picture of the microchannel and dummy structures.

2.2.2 Fluidic interface

In order to interface the microfabricated SU-8 microchannel with the integrated CMOS circuit (IC chip), we developed a dedicated fluidic interface. The main constraints for the choice of the materials are dictated by the need of having a non-magnetic setup.

The micro-to-macro interface between the SU-8 microchannel and the IC chip is schematically shown in Fig. 2.4. The interface bottom part, the microfluidic channel and the interface top part are pressed together, using brass screws and nuts to create a well-sealed microfluidic path (top right inset).

A system of tubes is connected to the microchannel inlets through plastic needles which are fitted in holes into the interface top part. The printed circuit board (PCB), containing the IC chip, provides the structural basis of the system. Four elongated holes in the PCB allow for sufficient free planar movement for the channel-to-coil alignment under an optical microscope.

The top part of the interface is made of a 5 mm Acryl photopolymer layer. This part is patterned by photopolymer jetting (3Dlabs) and hosts placeholders for two O-rings (0.039x0.02070Buna-N, Apple Rubber Products) that seal the fluidic path.

The bottom part is a 250-µm-thick alumina layer cut with a CO_2 laser. The central squared aperture provides the necessary opening for the IC chip and the bonding wires. The alumina layer is robust enough to apply the necessary sealing pressure. The assembled micro-to-macro interface is manually brought into contact and aligned with the integrated microcoil using a second system of screws that locks the structure in the desired position.

With this system we repeatedly achieve a good sealing, an easy handling of the liquid, and a positioning of the sample within a 10 µm precision.

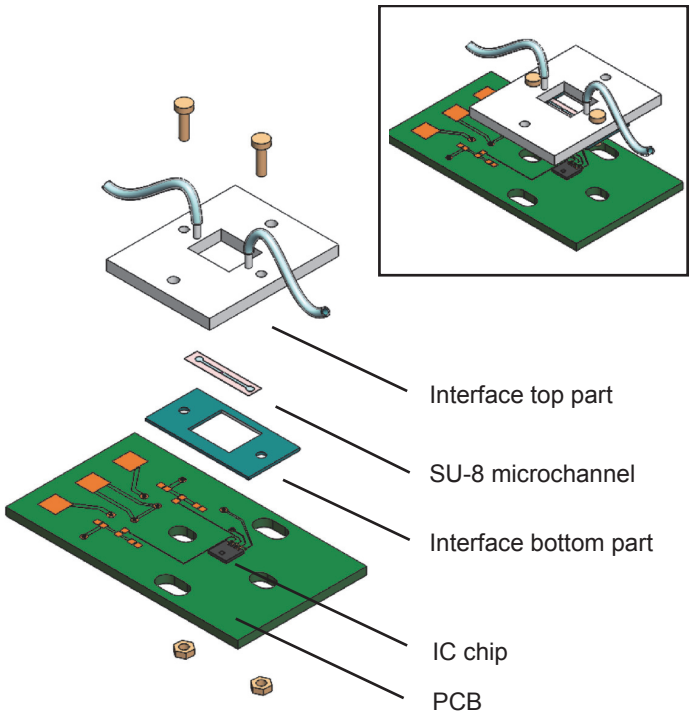

Figure 2.4: Illustration of the fluidic interfaces developed for the SU-8 microchannels. The exploded view of the system assembly. The IC chip is wire bonded on a PCB. The sealed fluidic device is created by assembling the microfabricated SU-8 channel with the interface bottom and top parts (top right inset). The sealed structure is then aligned with the IC detector coil and locked with screws and nuts.

2.3 3D printed microfluidic channels

The fabrication method developed for the fabrication of the SU-8 microchannel suffers from the lack of versatility and difficulty in scaling down, which are essential features to address subnanoliter samples having different sizes and geometries. To overcome these limitations we fabricated the microfluidic structure by two-photon polymerization, a 3D printing technique with 300 nm lateral resolution. The exceptional versatility of this 3D printed technique is essential for the rapid implementation of microfluidic systems for the handling, trapping and feeding of samples having different dimensions and fluidic behaviours.

The structural material of the microchannels is IP-S photoresist (Nanoscribe GmbH), which allows for a good sealing of the structure, is transparent, and gives flexibility in structuring the channel. The geometry of the channel is designed to maximize the field homogeneity (i.e., smooth long channels with walls parallel to the static magnetic field direction) and optimize the filling factor, thereby matching the volume of the sample with the sensitive volume of the detector coil.

For a sample placed at a distance of 10 µm from the detector surface, the loss in signal is about 30%, with respect to the ideal case where the sample is placed in direct contact with the chip surface (see section 1.3.1). This acceptable loss justifies the choice of fabricating a microfluidic channel with a wall of 10 µm, which is the actual separation layer between the sample and the chip (Fig. 2.5).

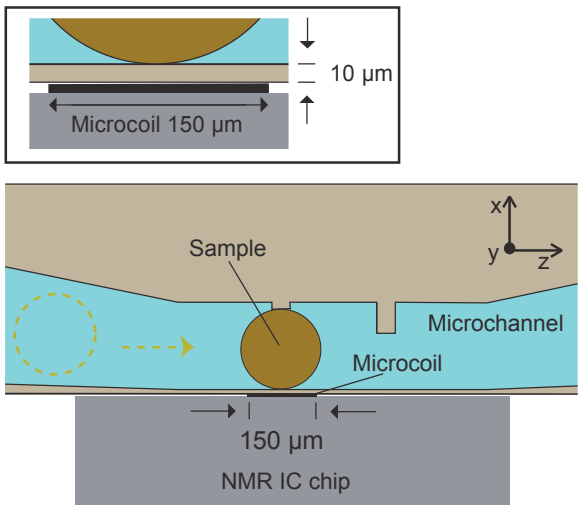

Figure 2.5: Illustration of the approach used to place the sample in close proximity of the most sensitive area of the on-chip excitation/detection microcoil. The coil lies in the *yz* plane with the static magnetic field B_0 along the *z* axis. The dashed lines indicate the direction of the insertion of a single ovum, which is trapped by two 10-µm-high pillars. A 50-µm-high pillar is employed to block the sample in case of accidental over-pressure. The microfluidic system is placed on top of the IC chip and aligned with the integrated detector coil. A 10-µm-thick IP-S photoresist layer defines the actual spacing between the sample and the chip surface (see inset).

2.3.1 Design and fabrication

We present two microfluidic devices designed for driving and trapping the living entities in the most sensitive area of the NMR integrated detector. Two customized microchannels are developed respectively for NMR investigations of single tardigrade *Richtersius coronifer (Rc)* ova and of single *C. elegans* worms.

The design of the microchannel for the *Rc* ovum consists of a cylindric inlet and outlet with a diameter of 240 μm. The microchannel gradually narrows in its centre to form a rectangular cross section with a height of 130 μm and a width of 140 μm. In correspondence of this narrowing, two 10-μm-high pillars are placed to trap the ovum for the duration of the experiment (Fig. 2.6a). A second larger and taller pillar is implemented to prevent the loss of the ovum in case of accidental overpressure during the loading of the sample. The trapping of the ovum in the location of interest does not prohibit the flow in the channel, which is essential if we want to apply reverse flow to recover the specimen or direct flow to refresh or change the medium.

Figure 2.6b shows the optical microscope picture of the top view of the central part of the microchannel. To better visualize the cross section of the microchannel and the system of pillars used to trap the ovum, a section of the microfluidic structure is 3D printed and inspected by SEM (Fig. 2.6c). The microfluidic chip designed for the *C. elegans* is configured with one inlet and one outlet, featuring a main entrance that splits into three channels and re-join at the outlet (Fig. 2.7a). The central microchannel is designed to match tightly the size of an adult worm, being 60 μm wide, 50 μm high and 1.3 mm long. 50-μm-high pillars at the end of this channel are placed in a V-shape and at a distance of 12 μm to block either the tail or the head of the *C. elegans*. The other two 55-μm-wide lateral channels are designed to deliver nutrients to the living trapped worm, being in fluidic connection with the two extremities of the central channel. To prevent the undesired trapping of other worms in the lateral feeding channels, one pillar is placed at their entrance.

Top view optical microscope pictures of the trapping pillars and the central part of the microfluidic structure are shown respectively in Figures 2.7b and 2.7c. Sections of the microfluidic device are 3D printed and inspected with the SEM to better visualize the V-shaped pillars (Fig. 2.7d) and the part of the microfluidic structure constituted by a central trapping microchannel and two lateral feeding microchannels (Fig. 2.7e).

In both of the designs, the gradual narrowing of the channel facilitates the hydrodynamic trapping of the samples. The size and shape of the inlet and outlet parts match the capillaries used for the fluidic connection with the external pumps, limiting the presence of dead volumes (see section 2.5). Similarly, the thickness of the separation layer gradually changes over the microchannel length, with a thickness of only 10 μm in proximity of the most sensitive region of the detector (i.e., above the excitation/detection microcoil). This strategy simultaneously implemets the requirements of proximity for the maximization of the NMR signal amplitude and robustness of the structure.

The microchannels are fabricated by a two-photon polymerization technique, using a high resolution 3D printed (Photonic Professional GT, Nanoscribe GmbH). This additive manufacturing technique provides 300 nm lateral resolution in a more versatile manner compared

to traditional microfabrication methods. The 3D printing of the fluidic structures is performed by L. Pethö (Laboratory for Mechanics of Materials and Nanostructures, EMPA, Thun).

The structures are patterned into IP-S photoresist, proprietary to Nanoscribe GmbH. This resist is a negative tone cross-linking type polymer designed for mesoscale applications. An indium tin oxide (ITO) coated glass slide serves as a substrate. The refractive index difference between the two materials facilitates interface detection. For the release of the microchannels, a 500-nm-thick Dextran layer from Leuconostoc (Sigma-Aldrich, 31390-25G) is spin coated onto the substrate. This sacrificial layer is subsequently dissolved in water, enabling the release of the structures at the end of the fabrication process.

A Carl Zeiss 25x objective (LCI Plan-Neofluar 25/0.8 Imm Korr DIC M27) is used in direct immersion mode into the photoresist. The refractive indices of the objective and the photoresist are matched to ensure high resolution. The voxel diameter is determined by a preceding test exposure, and the results are fed into the modelling software which imports Solidworks STL files to generate machine specific data. Using 50 m/s writing speed, the voxel diameter has been verified to be in the 0.3-0.4 μm range. In this configuration, the aspect ratio of the voxel is typically (5-6):1.

A droplet of IP-S resist is placed onto the substrate and the objective is immersed into the resist droplet. The objective is fixed in space, while the positioning of the substrate is given by the combination of galvanometer MEMS mirrors and a piezoelectric unit. In the *xy* plane, the galvanometer mirrors travel within a 200 μm radius at each fixed position of the piezoelectric stage. A slicing distance of 1 μm is defined to split the structure into equal distance horizontal planes which are defined by the piezoelectric stage. This parameter is set to ensure proper overlapping and adhesion in between the horizontal planes.

To decrease the writing time, a scaffolding technique is implemented within bulk volumes. A triangular support structure is used, with a 20 μm spacing between planes and scaffolding wall thickness of 3 μm. The writing time for single microfluidic structure is approximately 5 hours. To provide control over the resist-air interface, and to maintain mechanical resistance over an extended period of development, a 18-μm-thick outer shell is defined, which is patterned as a bulk area.

The accessible area of the galvanometer mirrors is limited by the beam deflection and it is confined in a 200 μm radius circle. The block is a volume which can be written at a single *xy* piezoelectric stage position, only by moving the galvanometer mirrors and the piezoelectric stage in the *z* direction. The block has a hexagonal shape to optimize the volume accessible by the galvanometer mirrors and to facilitate stitching by having large neighbouring block surfaces. The blocks are written in a consecutive manner: a piezoelectric stage *xy* position is chosen, which gets exposed by the combination of the galvanometer mirrors and the piezoelectric stage in the *z* direction. When the block writing is finished, the piezoelectric stage moves to the next neighboring position and restarts exposure as before. A block shear angle of 13° is used in the *z* direction to avoid a shadowing effect, which occurs at overlapping block edges due to increased exposure. A block overlap of 2.5 μm enhances the stitching by reinforcing the adhesion between blocks. The block size is chosen to be *x*: 220 μm, *y*: 190 μm, *z*: 250 μm. Applying the shear angle and overlap, the total block dimension becomes *x*: 259.5 μm, *y*: 259 μm, *z*: 250 μm.

The laser power is 65 mW at the point of entering the objective. For writing the shell of the structure, this is reduced to 42%. For the internal scaffolding, to increase robustness at the cost of resolution, it is increased to 50%.

Following exposure, the objective is removed from the photoresist, and the substrate is placed into PGMEA (Sigma-Aldrich) for development. The substrate is positioned in a way that the channels stand vertically. There is a slow but continuous stirring in the beaker, to enhance the removal of developed photoresist residues from inside the channel. The development duration is typically 6 hours. When development is finished, the substrate is immersed into isopropanol in an identical configuration for one hour. A second rinse step, with ultra-high purity isopropanol (99.99 %+) is used to further clean the inside of the channels, for a duration of 30 min. Finally, the substrate is left to naturally dry in a vertical position.

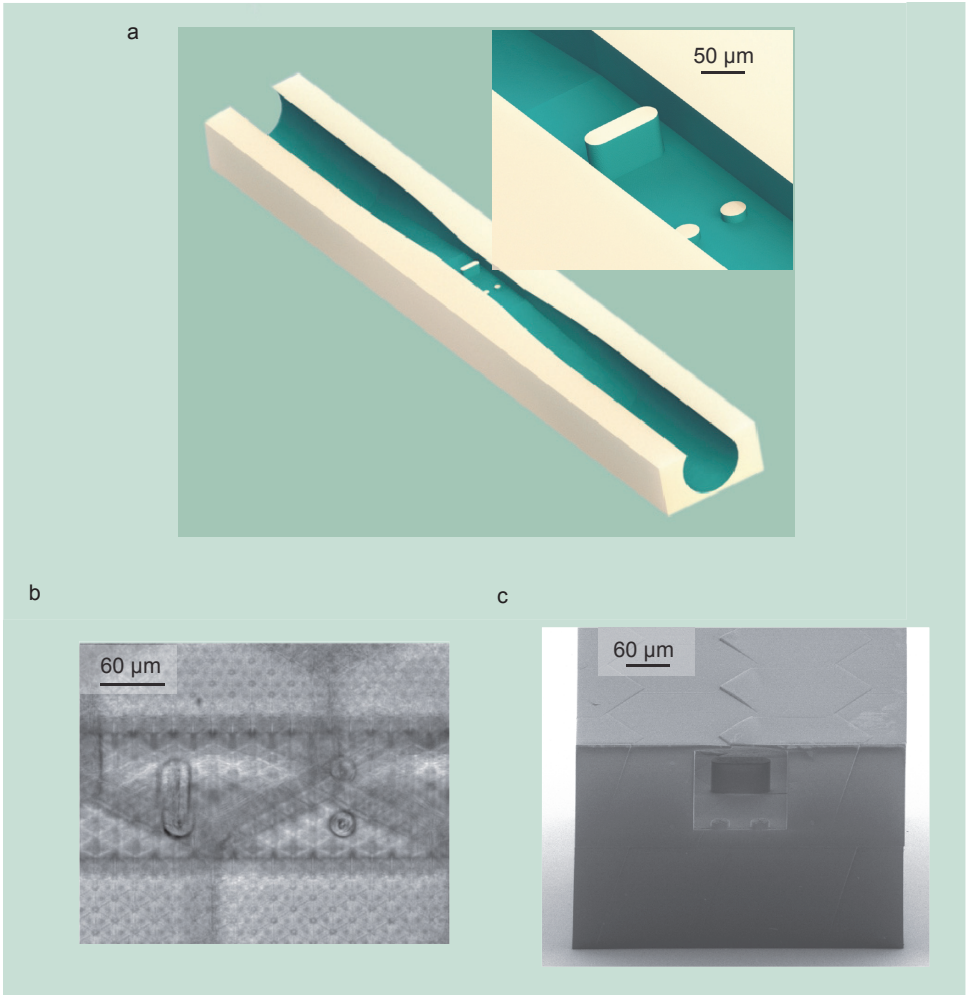

Figure 2.6: Pictures of the microfluidic system designed for the trapping of a single *Rc* ovum. (a) Rendering of the microchannel used to trap *Rc* ova. A close up view of the trapping pillars is shown. (b) Top view optical microscope picture of the central part of the microchannel. (c) SEM picture of a microchannel section, 3D printed to better visualize the trapping system. Two 10-µm-high pillars trap the ovum, while a second pillar is implemented to prevent the loss of the ovum in case of accidental overpressure.

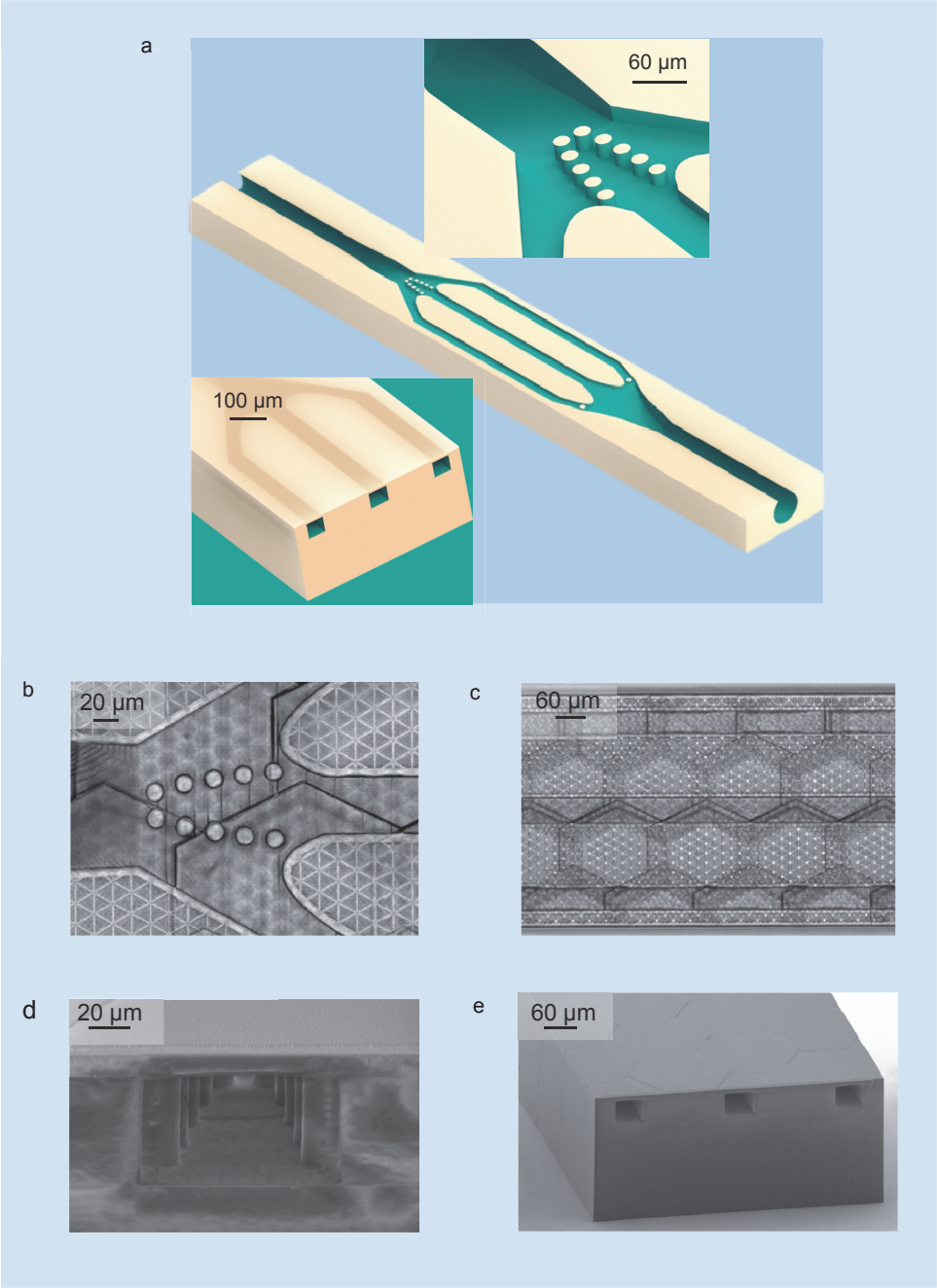

Figure 2.7: Pictures of the microfluidic system designed for the trapping of a single *C. elegans* worm. (a) Rendering of the microchannel used to trap the *C. elegans* worms. Close up views of the trapping pillars and the central part of the microfluidic structure are shown. (b) Top view optical microscope picture of the pillars used to trap the head or tail of the *C. elegans*. (c) Top view optical microscope picture of the three microfluidic channels. The central microchannel traps the worm while the two lateral ones provide food to the trapped *C. elegans*. (d) SEM picture of a 3D printed channel section showing the trapping pillars. (e) SEM picture of a 3D printed channel section showing the central trapping microchannel and two lateral feeding microchannels.

2.3.2 Fluidic interface

In order to precisely position and tightly hold the high resolution 3D printed microfluidic chips in contact with the single-chip integrated CMOS detector (and to connect its microchannels to the external pump) an interfacing structure is fabricated.

The 3D printed microfluidic chips are first glued on a 200 µm x 2 cm PMMA rod for support using a cyanoacrylate adhesive (ECS500, 3M). After, PMMA capillaries (Paradigm Optics) are fitted in the inlet and the outlet of the 3D printed microchannels.

The realized assembly, shown in Fig. 2.8a, is introduced into a 3D printed plastic holder (Fig. 2.8b) fabricated by a conventional stereolithographic 3D printer (Form+1, Formlabs). The holder is patterned out of a photosensitive resin (Clear FLGPCL02, Formlabs) and is constituted of two complementary parts to facilitate the insertion of the fluidic assembly.

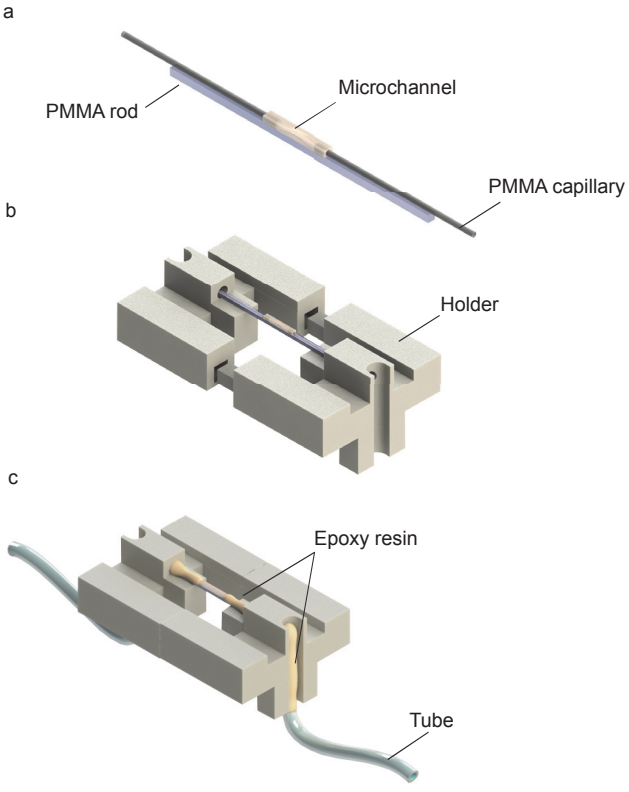

Figure 2.8: Illustration of the fluidic interface developed for the 3D printed microchannels. (a) The microfluidic channel is attached to a PMMA rod and connected to PMMA capillaries to create a fluidic assembly. (b) The fluidic assembly is mounted in the holder. (c) Micro-to-macro interface is completed by connecting tubes to the PMMA capillaries and performing the casting of epoxy resin to create the sealing and give robustness to the fluidic system.

A system of tubes is connected to the fluidic assembly through the PMMA capillaries and a casting of epoxy resin (Araldite) is performed to seal the fluidic system and to give robustness to the structure.

The assembled fluidic interface (Fig. 2.8c) is manually brought into contact and aligned to the integrated excitation/detection microcoil under an optical microscope. Wax is used to maintain the interface in position.

A central squared aperture in the holder provides visibility for the alignment. The printed circuit board (PCB), containing the single-chip integrated NMR detector, includes two elongated holes to allow for sufficient free planar movement for the microchannel-to-microcoil alignment. With this system, we repeatedly achieved a good seal, easy handling of the liquids, and a positioning of the sample within 10 μm precision.

2.4 NMR electronic set-up

Figure 2.9 shows an illustration of the NMR experimental set-up. The single-chip CMOS integrated NMR detector is glued onto a printed circuit board (PCB) and electrically connected by wire bonding.

A single RF generator is used to provide the RF signal for the transmission (Tx) and as local oscillator (LO) for the on-chip frequency down-conversion. The frequency down-converted and amplified signal and the output of the single-chip NMR detector is further amplified by an external amplifier and sent to a multifunctional board for acquisition.

The PCB is inserted in the 54 mm room temperature bore of a 7.05 T superconducting magnet (Bruker, 300 MHz). The 3D printed microchannel lies along the direction of the static magnetic field B_0 to reduce the effect of susceptibility mismatches by having the walls of the microchannel parallel to the direction of B_0. In this configuration, the NMR linewidth is about a factor of two narrower with respect to the configuration where the channel is perpendicular to the static magnetic field.

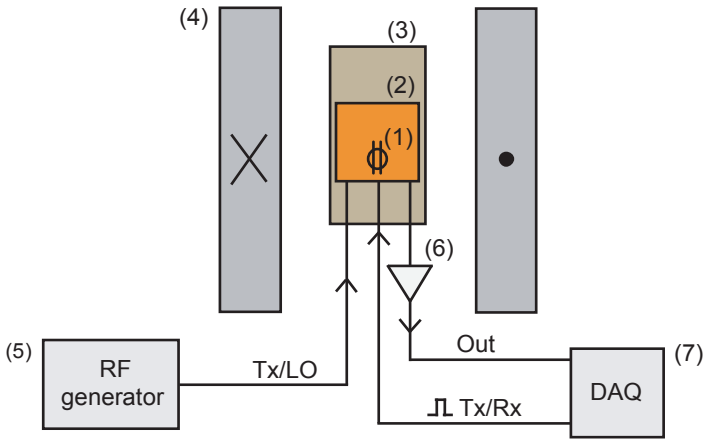

Figure 2.9: Schematic of the electronics setup used for the NMR measurements. (1) Integrated excitation/detection coil interfaced with the microfluidic structure. (2) Single chip NMR detector (see details in Ref. 1). (3) Printed circuit board (PCB). (4) Superconductive magnet (Bruker, 7 T). (5) RF source (MG3633A, Anritsu). (6) AF amplifier (SRS560, Stanford Research Systems) (7) Multifunctional board (PCIe-6259, National Instruments) for the generation of TX/RX switching pulse and the signal acquisition.

2.5 Fluidic set-up for sample loading and trapping

Figure 2.10 shows an illustration of the fluidic set-up. The 3D printed microfluidic chip (together with its fluidic interface) is placed into an inverted microscope (Axio Observer, Zeiss) equipped with a High-Power LED Illumination system (precisExcite, Visitron) for brightfield imaging. The microscope is equipped with a motorized *xyz* stage that has a piezo controller for *z* displacement (ASI, Visitron). The microfluidic operations are controlled using syringe pumps and its software (Nemesys, Cetoni GmbH).

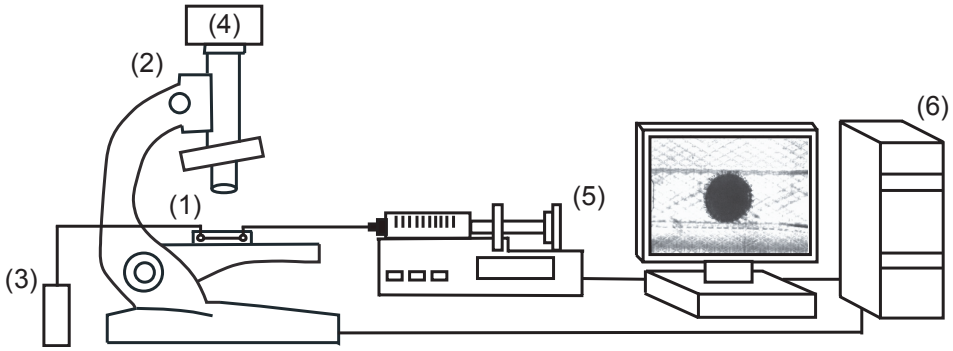

Figure 2.10: Schematic of the fluidic set-up used for the loading and trapping of biological samples. (1) Microfluidic chip and its fluidic interface. (2) Inverted microscope (Axio Observer, Zeiss), High-Power LED Illumination system (precisExcite, Visitron) for brightfield imaging. (3) Liquid waste. (4) High resolution digital camera (ORCA-ER C4742-80, Hamamatzu). (5) Syringe pumps (Nemesys). (6) Desktop computer.

2.6 NMR spectroscopy of subnanoliter liquid samples

In this section we show a collection of spectra obtained from subnanoliter liquid samples at 7 T (300 MHz) using the SU-8 microchannels (details in section 2.6.1) and the 3D printed microchannels (details in section 2.6.2). These measurements are performed to characterize the spectral resolution limits of the setups and to calibrate the sensitivity of the detector. All chemical shifts are expressed in ppm deviation from the resonance frequency of a standard reference sample, tetramethylsilane (TMS). Since this reference compound is not present in our samples, we assigned a chemical shift of 4.8 ppm to the peak of water (present in all the samples investigated), inferring the chemical shifts of the other peaks based on the frequency shift.

The excitation pulse length used in the reported experiments corresponds to the experimental condition of maximum sensitivity, in good agreement with the value computed with simulations via sensitivity maps (see section 1.3.1). In all the spectra, the amplitude of the peaks is normalized to the one of the peak of pure water contained in the microchannels used for the measurements.

2.6.1 Measurements performed with SU-8 microchannels

Figures 2.11 shows a collection of spectra obtained from liquid samples, using the SU-8 microfluidic channel, the fluidic interface and the electronic set-up described respectively in section 2.2.1, 2.2.2 and 2.4. The excitation pulse length used in the reported experiments corresponds to the experimental condition of maximum sensitivity (τ = 4 μs).

Figure 2.11a shows the ^{1}H NMR spectrum of water after averaging over 10 min. A lorentzian fit to the data indicates a spectral full width at half-maximum (FWHM) of 15 Hz. The baseline width, defined as the peak width at 0.55% height of the peak of water, is instead 240 Hz. The achieved spectral resolution is probably caused by imperfections in the mounting of the channels and by their non-ideal geometry (as shown in the section 2.6.2, a spectral resolution of 2 Hz is achieved employing microchannels fabricated using a high resolution 3D printer). The developed microfabrication process does not allow complete freedom for the choice of the design of the microfluidic structure.

Figure 2.11b shows the ^{1}H NMR spectrum obtained from 300 mM betaine in D_2O (BO300-1vl betaine solution 5M, Sigma), after averaging over 30 min. The peaks at 3.9 ppm and 3.3 ppm correspond, respectively, to the ^{1}H in the CH_2 and CH_3 group. Integrals have a 9:2 ratio as expected for betaine ($(CH_3)_3N^+CH_2COO^-$). The betaine concentration used is similar to the one observed in a single giant neuron from *Aplysia Californica*[8].

Figure 2.11c shows the ^{1}H NMR spectrum of 500 mM sucrose in D_2O (84099 D(+)-Sucrose Fluka Biochemika) after averaging over 3 h. We assigned a chemical shift of 4.8 ppm to the main peak as reported in Ref. 75. The peak at 5.3 ppm refers to the proton in the CH group linked to the oxygen bridge. The peak due to the ^{1}H content in the CH_2 compound in the glucose and fructose ring is visible at 3.7 ppm and the CH_2 compound at 3.6 ppm. Unresolved peaks are due to the presence of ^{1}H in multiple CH compounds around the two ring-shaped structures of the sucrose molecule.

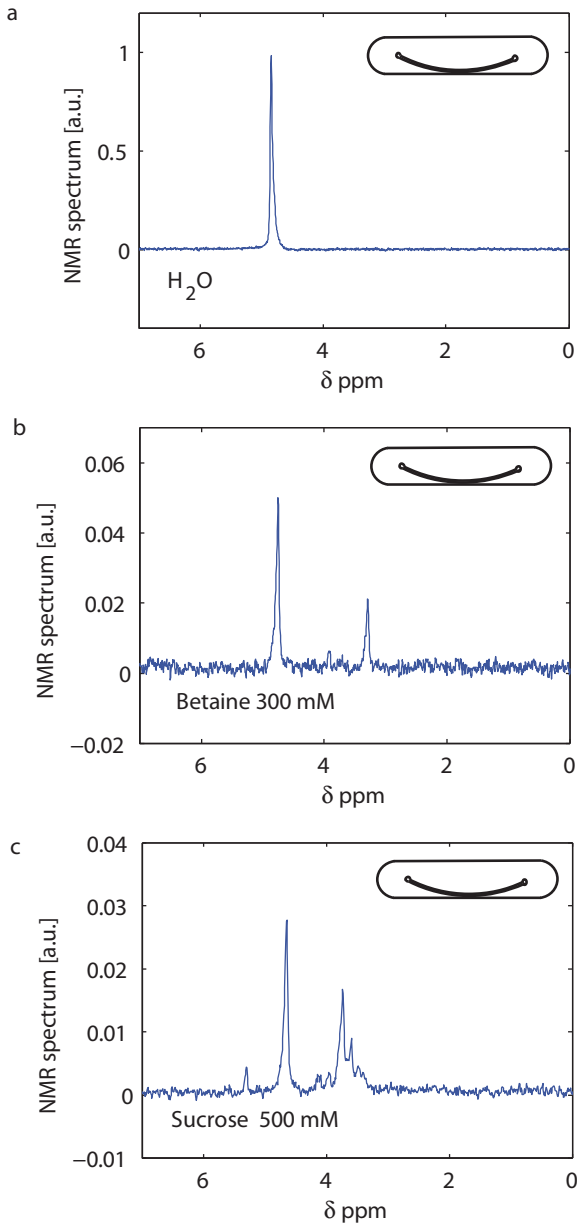

Figure 2.11: NMR measurements on liquids, performed using the SU-8 microchannels. The spectra are acquired at 7 T (300 MHz) and are FFT real parts. Experimental condition notation: V is the active volume, Avg is the number of averaged measurements, T_R is the repetition time, τ is the pulse length, T_m is the matching filter decay time constant. (a): ^{1}H spectrum of water: $V \sim 170$ pL; $Avg = 600$; $T_R = 1$ s, $\tau = 4$ µs, $T_m = 250$ ms. (b): ^{1}H spectrum of 300 mM betaine in H_2O/D_2O: $V \sim 170$ pL; $Avg = 1800$; $T_R = 1$ s, $\tau = 4$ µs, $T_m = 120$ ms. (c): ^{1}H spectrum of 500 mM sucrose in D_2O: $V \sim 170$ pL; $Avg = 10800$; $T_R = 1$ s, $\tau = 4$ µs, $T_m = 120$ ms.

2.6.2 Measurements performed with 3D printed microchannels

Figures 2.12 shows a collection of spectra obtained from liquid samples (water and lactic acid in water) using the *C. elegans*-dedicated microchannels, the fluidic interface and the electronic set-up described respectively in section 2.3.1, 2.3.2 and 2.4. The excitation pulse length corresponds to the experimental condition of maximum sensitivity (τ = 3.5 µs), in good agreement with the value of 3.7 µs computed with simulations via sensitivity maps (Fig. 1.1).

Figure 2.12a shows the ^{1}H NMR spectrum of water after averaging over 66 min. The lorentzian fit to the data indicates a spectral full width at half-maximum (FWHM) of 2 Hz. The baseline width, defined as the peak width at 0.55% height of the peak of water, is instead 24 Hz. These values of spectral resolution are systematically achieved in six separated experiments employing six different microchannels with the same nominal design.

Figure 2.12b shows the ^{1}H NMR spectrum obtained from 1.3 M of lactic acid (L1750 Lactc acid ≥ 98%, Sigma-Aldrich), after averaging over 6 h. The FWHM in this spectrum is also 2 Hz. As shown in the inset, the achieved spectral resolution is sufficient to show the 7 Hz J-splitting within each of the two chemically shifted signals of the lactic acid. The two peaks at about 1.3 ppm arise from the ^{1}H nuclei in the CH_3 group, J-split by the ^{1}H nucleus of the nearby CH group. The four peaks at about 4.08 ppm arise from the ^{1}H nucleus of the CH group, and show the 1:3:3:1 J-split due to the ^{1}H spins in the CH_3 group.[117]

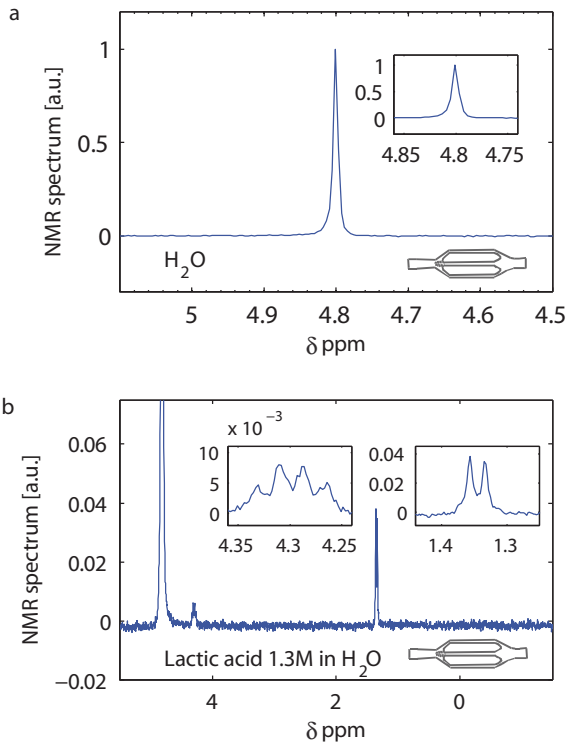

Figure 2.12 : NMR measurements on liquids, performed using the 3D printed microchannels. The spectra are acquired at 7 T (300 MHz) and are FFT real parts. See definition of notations in figure 2.11. The active volume is equal to 100 pL. (a): ^{1}H spectrum of water: Avg = 1000; T_R = 4 s, τ = 3.5 µs, T_m = ∞. (b): ^{1}H spectrum of 1.3 M lactic acid in H_2O: Avg = 10800; T_R = 2 s, τ = 3.5 µs, T_m = 500 ms.

Better spectral resolutions (down to 0.6 Hz) have been reported in literature,[69, 76, 118, 119] but with probes having a limit of detection (LOD), reported to a field strength of 300 MHz, down to 1.2 nmol $s^{1/2}$ and active volumes down to 10 nL.

Fig. 2.13a shows the spectrum of pure water obtained using the *Rc* ova-dedicated microchannel described in section 2.3.1. In this microchannel we inserted pillars in close proximity to the sensed volume, in order to trap the *Rc* ova (Fig. 2.6). The mismatches in susceptibility are larger than in the microchannel designed for the trapping of the *C. elegans*, resulting in an experimentally measured spectral resolution of 10 Hz FWHM (*i.e.*, 5 times worse with respect to the other design) and a baseline width of 75 Hz.

The approach proposed in this chapter (*i.e.*, 3D printed microchannels combined with single-chip CMOS integrated detectors) allows for sub-nL NMR spectroscopy with spectral resolutions consistently limited by the specific design of the microfluidic structure, with an experimentally demonstrated spectral resolution of 0.007 ppm for one of the two implemented designs.

These data are used to calibrate the sensitivity of the sensor, which is experimentally found to be $2.5 \cdot 10^{13}$ spins/$\sqrt{\text{Hz}}$. Such value of sensitivity corresponds to a frequency-domain limit of detection LOD_f, of 600 pmol of ^{1}H nuclei with a FWHM of 2 Hz expressed per single scan (for details see section 2.7.6).

Study of the background

When performing spectroscopy on intact biological entities, it can be useful to suppress the strong (and broad) water peak that may cover peaks at neighbouring frequencies. A solution to this problem is to submerge the sample in D_2O. However, various materials (polymers included) can easily exchange ^{1}H and ^{2}D nuclei. To characterize the background signal due to proton exchange between the microchannel material and D_2O, we monitored a sample of D_2O + 2% H_2O over 60 h.

Figure 2.13b shows the ^{1}H NMR spectrum of D_2O + 2% H_2O after averaging over 15 min. The spectra in blue and in red are acquired respectively after 1 h and 60 h from the filling of the microchannel. We detect a gradual increase of the amplitude of the peak at 4.8 ppm. We attribute this phenomenon to a release of hydrogens from the structural material of the microchannel and the consequent proton exchange with the D_2O and the formation of HDO and H_2O.

Figure 2.13c shows the evolution of the amplitude of the peak of H_2O and HDO over 60 h. All the spectra are normalized to the amplitude of the peak of pure water. The actual increase in the concentration of H_2O and HDO in D_2O is equal to a factor 3.5, from an initial concentration of 2% up to 7% after 60 h. A saturation is observed after approximately 40 h.

This would suggest that we can eliminate the peak at 4.8 ppm by further flushing the microchannel with D_2O. Additional measurements are necessary to confirm this statement. The peak at 4.8 ppm contributes to the only background signal present in our experimental condition.

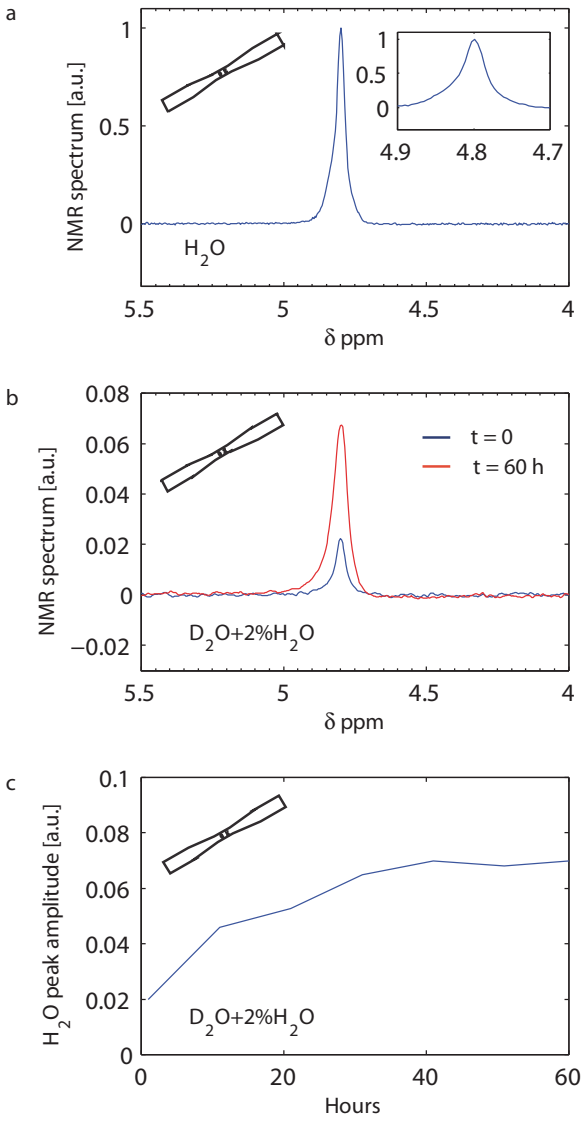

Figure 2.13: NMR measurements on pure water and D_2O + 2% H_2O performed using the 3D printed microchannels. The spectra are acquired at 7 T (300 MHz) and are FFT real parts. See definition of notations in figure 2.11. The active volume is equal to 250 pL. (a): ^1H spectrum of water: Avg = 1800; T_R = 2 s, τ = 3.5 µs, T_m = ∞. (b) ^1H spectrum of D_2O + 2% H_2O after averaging over 15 min; in blue the spectrum acquired during the first hour of measurement, in red the spectrum acquired after 60 h from the filling of the microchannel: Avg = 450; T_R = 2 s, τ = 3.5 µs, T_m = 100 ms. (c): Amplitude of the peak at 4.8 ppm vs hours: Avg = 1800; T_R = 2 s, τ = 3.5 µs, T_m = 100 ms.

2.6.3 SU-8 microfabricated microchannels versus 3D printed microchannels.

The microfabrication process, developed to pattern SU-8 microchannels, is compatible with large scale production of microfluidic devices. It allows for complex 2D shaping of the microchannels, having lengths up to the centimeter-scale. It is the ideal solution for the patterning of large structures (above 10 mm^3 of bulk material), where there is no need of a 3D design and the resolution is not an issue. The resolution is limited by the diffraction limit and strongly dependent on the thickness of the SU-8 layer and the aspect ratio of the structures to be patterned.

The two-photon polymerization technique permits a lateral resolution of 300 nm independently on the final thickness of the structure, which can be as thick as 1 mm. Despite the 3D printing technique is not suitable for large scale production, it allows for the rapid prototyping of complex microstructures, which could not be fabricated with traditional microfabrication methods. The exceptional flexibility in the choice of the design enables the realization of complex microfluidic systems for the handling, feeding and trapping of subnanoliter biological samples having different geometries, sizes and fluidic behaviours. With a printing time of about 5 hours per single microfluidic system, of about 0.5 mm^3 of bulk material, the patterning timescale would be unimaginable for traditional microfabrication techniques. The close to zero operational cost is also seen as a considerable advantage. Moreover this technique is an excellent candidate for NMR applications; a reduction of susceptibility mismatching is possible thanks to the flexibility in the design of the microfluidic system, chosen to decrease magnetic field non-uniformities. A minimization of the dead volume is also possible, which is crucial for NMR experiments on mass-limited liquid samples.

2.7 NMR spectroscopy of subnanoliter biological samples

In this section we show a collection of ^1H NMR spectra obtained at 7 T (300 MHz) from intact static biological samples. NMR spectra obtained from a single *Rc* ovum are reported in section 2.7.4, while in section 2.7.5 we show NMR spectra obtained from a subsection of a *C. elegans* worm.

Rc ova have typical volume of 500 pL, while adult *C. elegans* worms have typical volume of 5 nL. The most sensitive region of the NMR integrated detector corresponds to a semi-ellipsoid with a volume of approximately 300 pL (see Fig. 1.1). In the experiments, the sensed portion of the microorganisms is given by the intersection of the sensitive region of the detector with the volume of the sample. Defining the active volume as the fraction of the sample that contributes to the 70% of the total signal and considering the geometries in play and their position with respect to the microcoil, we estimate active volumes of about 250 pL in the case of the *Rc* ovum and 100 pL in the case of the *C. elegans* worm.

We assigned a chemical shift of 4.8 ppm to the peak of water contained in the samples under investigation, thus determining the chemical shifts of the other peaks.

In both *Rc* and *C. elegans* spectra, the linewidths are one order of magnitude broader than the ones measured with liquid samples (as shown in Fig. 2.12 for pure water and lactic acid). Previous studies suggest that the spectral resolution may be limited by microscopic constituents in the samples, which introduce susceptibility mismatches which are difficult to compensate by field shimming[6, 7]. As shown below, the linewidths observed in this study are of 35 Hz FWHM for the *Rc* ovum and 30 Hz FWHM for the *C. elegans*.

Thanks to the freedom in the design of the microchannels, the stable trapping, and the robustness of the fluidic interface, the duration of our experiments depends only on the viability of the biological sample under investigation. The successful implementation of long measurements (up to two weeks) allows to improve the signal-to-noise ratio and to perform continuous observations on the same single entity on a time scale that can be comparable to the biological development of the sample.

As explained in details in section 2.7.3 we could reduce, with respect to previous contributions[112], the repetition time T_R from 2 s down to 200 ms with no relevant changes in the amplitude of the peaks. Such improvement corresponds to a factor 3.3 in experimental time at parity of SNR.

2.7.1 Preparation of *Rc* ova and microfluidic operation

Preparation of Rc ova

Eggs of *Rc* were extracted from a moss sample collected in Öland (Sweden) by washing the substrate, previously submerged in water for 30 min, on sieves under tap water and then individually picking up eggs with a glass pipette under a dissecting microscope. The eggs were shipped within 24 h in sealed Eppendorf tubes with water and subsequently stored at -20 °C before use. All experiments were carried out within a week after tube opening.

Operation of the microfluidic platform

We report to section 2.5 for the description of the fluidic set-up used for the handling and trapping of the sample.

The microfluidic chip and tubes are first filled with the chosen medium (D_2O or H_2O according to the experiment). A group of ova is first transferred from the Eppendorf into a Petri dish prepared with 3% H_2O-based agarose gel. A single *Rc* ovum is transferred from the agarose plate to the medium reservoir using a manipulation pipette (Vitrolife). At this point the ovum is sucked up into the tube connected to the microfluidic system directly from the pipette.

Later, with a flow of 500 nL/s, the ovum is injected in the microfluidic chip through the inlet. In order to place the ovum on top of the two trapping pillars (see Fig. 2.14), a flow of 3 µL/s is applied. Once trapped, the flow is stopped and the tubes are clamped. The whole operation and the following experiments are performed at 20 °C.

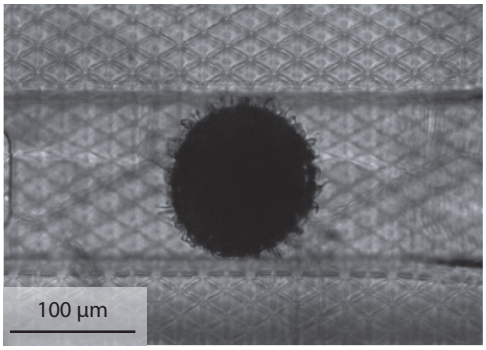

Figure 2.14: Optical microscope picture of a *Rc* ovum trapped in the 3D printed microfluidic structure.

2.7.2 Preparation of *C. elegans* and microfluidic operation

Preparation of C. elegans

The *C. elegans* wild type worms are cultured at 20 °C on nematode growth media (NGM) 90 mm Petri dishes seeded with Escherichia coli (strain OP50). Worms are provided by the Caenorhabditis Genetics Center (University of Minnesota).

E. coli culture

HT115 *E. coli* bacteria are grown in Luria Broth (LB) with 100 µg/mL ampicillin and 12.5 µg/mL tetracycline overnight in a thermal shaker at 37 °C. The following day, 50 µL of the confluent bacterial cultures are used to inoculate freshly prepared LB medium containing only ampicillin. The new cultures are grown until reaching an optical density between 0.6 and 0.8, and 90 µL are used for seeding the experimental plates. The *E.coli* culture was performed by Prof. Auwerx's group (Laboratory of integrative systems physiology, EPFL).

Operation of the microfluidic platform

We refer to section 2.5 for the description of the fluidic set-up used for the handling and trapping of the sample. The microfluidic chip and tubing are first filled with S medium, prepared by Prof. Gijs's group (Laboratory of Microsystems 2, EPFL) following the protocol reported in Ref. [120].

By using a worm picker, a worm of the desired size is transferred from the agarose plate to an S medium reservoir, from which it is sucked up into a tube connected to the device. Afterwards, the worm is injected in the microfluidic chip from the inlet with a flow of 500 nL/s. In order to insert the animal in the trapping channel, a flow of 1 µL/s is applied.

Once trapped (see Fig. 2.15), a gentle flow of 50 nL/s of *E. coli* bacteria is used to replace the S medium in the chip and therefore provide nutrients to the worm through the lateral channels. After observing the pharyngeal pumping in the worm, which confirms that it is eating properly, the flow is stopped and the tubes are clamped. The whole operation, and the following NMR experiments, are performed at 20 °C.

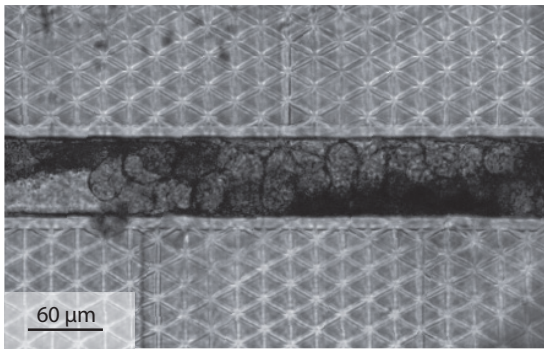

Figure 2.15: Optical microscope picture of a *C. elegans* trapped in the 3D printed microfluidic structure.

2.7.3 Optimization of the experimental parameters

We report ^{1}H NMR measurements of a single *Rc* ovum in H_2O performed employing different values of repetition time (T_R). Table 1 shows the amplitude of the signal at 4.8 ppm and at 1.3 ppm for different values of T_R and normalized to the signal amplitude obtained with a T_R equal to 2 s.

Table 1: Amplitude of the signal at 4.8 ppm and 1.3 ppm for different value of repetition time T_R, normalized to the amplitude obtained for $T_R = 2$ s.

T_R	$S_{4.8ppm}$	$S_{1.3ppm}$
2 s	1	1
200 ms	0.9	0.9
50 ms	0.1	0.2

Fig. 2.16 shows the ^{1}H NMR spectra obtained from a single *Rc* ovum in H_2O, with a T_R of 2 s (Fig. 2.16a), 200 ms (Fig. 2.16b) and 50 ms (Fig. 2.16c) after averaging over 12 h. For all the spectra, the signal amplitude is normalized to the amplitude of the peak at 1.3 ppm obtained with a T_R of 2 s. The pulse length is equal to 3.5 µs for all the measurements.

Decreasing the T_R from 2 s down to 200 ms the NMR signal (water peak included) does not change relevantly, while a T_R of 50 ms results in a significant loss in signal. This observation can be associated to:

1. The effective spin-lattice relaxation times of the compounds inside the sample.
2. The B_1 field non-uniformities, which imply a variation of the effective flip angle all over the sample.

In case of NMR measurements done on a sample of pure water, the employment of a T_R equal to 0.2 s implies a decrease of an order of magnitude in the signal amplitude, which is not experimented in the NMR measurements of a single *Rc* ovum. From this observation we can

exclude the dominance of the second effect and assume that the compounds inside the samples have a reduced spin-lattice relaxation time with respect to the case of pure water. However, these measurements do not allow determining the actual value of the relaxation time. To precisely evaluate the value of the spin-lattice relaxation time and eliminate the effect of magnetic field non uniformities, an inversion recovery experiment would be needed. The efficient application of a pulse sequence is complicated by the non-uniform distribution of the B_1 over the sensitive volume of the integrated detection microcoil. The determination of local values of flip angle could probably facilitate the estimation of the spin-lattice relaxation time of the sample under investigation. From a pragmatic point of view, the reduction of the T_R permits an improvement in the experimental time. Decreasing, with respect to previous contributions[74], the T_R from 2 s down to 200 ms we have an improvement of a factor 3.3 in experimental time at parity of SNR.

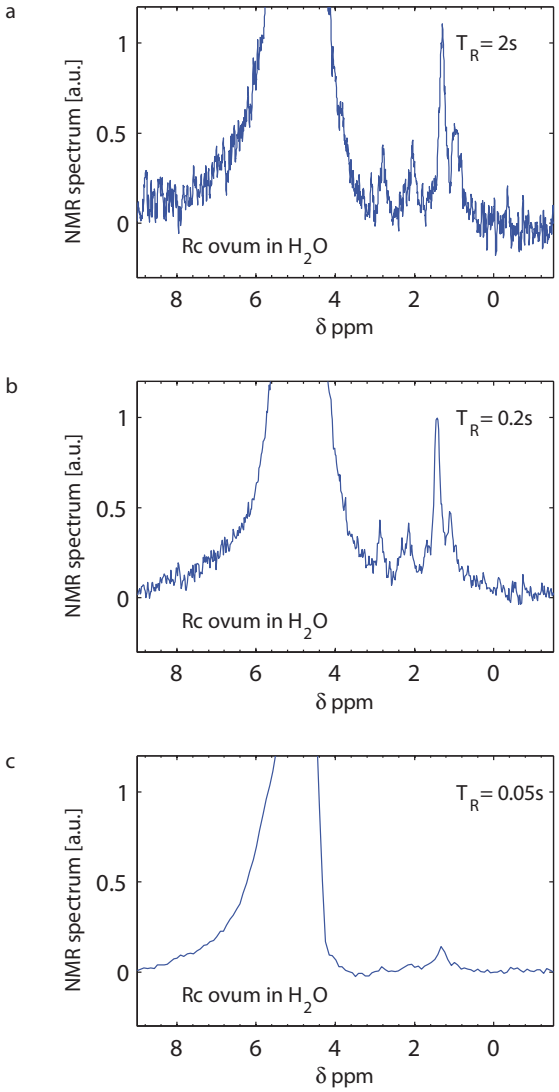

Figure 2.16: NMR measurements of a single *Rc tardigrade* ovum in H_2O performed at 7 T (300 MHz). The spectra are FFT real parts. Experimental condition notation: V is the active volume, *Avg* is the number of averaged measurements, T_R is the repetition time, τ is the pulse length, T_m is the matching filter decay time constant. (a): V ~150 pL; *Avg* = 21600; T_R = 2 s, τ = 3.5 µs, T_m = 30 ms. (b): V ~150 pL; *Avg* = 216000; T_R = 200 ms, τ = 3.5 µs, T_m = 30 ms. (c): V ~150 pL; *Avg* = 864000; T_R = 50 ms, τ = 3.5 µs, T_m = 30 ms.

2.7.4 NMR measurements of a single *Rc* ovum

Fig. 2.17a and 2.17b shows NMR spectra obtained at 7.05 T (300 MHz) from a single *Rc* ovum in H_2O after averaging respectively over 3 and 75 h. Measurements in water provide the best conditions in terms of biocompatibility. However, with a linewidth of about 35 Hz, the baseline of the water peak can overlap significantly with eventual small nearby signals.

To suppress the strong water peak that originates from the carrying medium, we suspended the sample in a D_2O-based environment. NMR spectra obtained from a single *Rc* ovum in D_2O after averaging over 3 and 75 h are shown respectively in Fig. 2.17c and 2.17d. As noticeable from figure 2.17d we have an increase over time of the residual background signal at 4.8 ppm, with a consequent broadening of the peak baseline that overlaps with nearby signals. As mentioned in the section 2.6.2, the release of hydrogens from the microchannel material contributes to the residual water background signal.

Acceptable SNR can be obtained averaging only over 3 h as shown in Fig. 2.17a and 2.17c. The same *Rc* ovum is used to perform measurements in H_2O and D_2O. In between the two experiments, the liquid is easily exchanged without repeating the trapping procedure.

Due to the relatively low SNR (caused by the very small number of spins contained in the sample) and the relatively poor spectral resolution, a detailed proton peak assignment is currently impossible. Nevertheless, some information can be obtained from previous studies on *Xenopus*

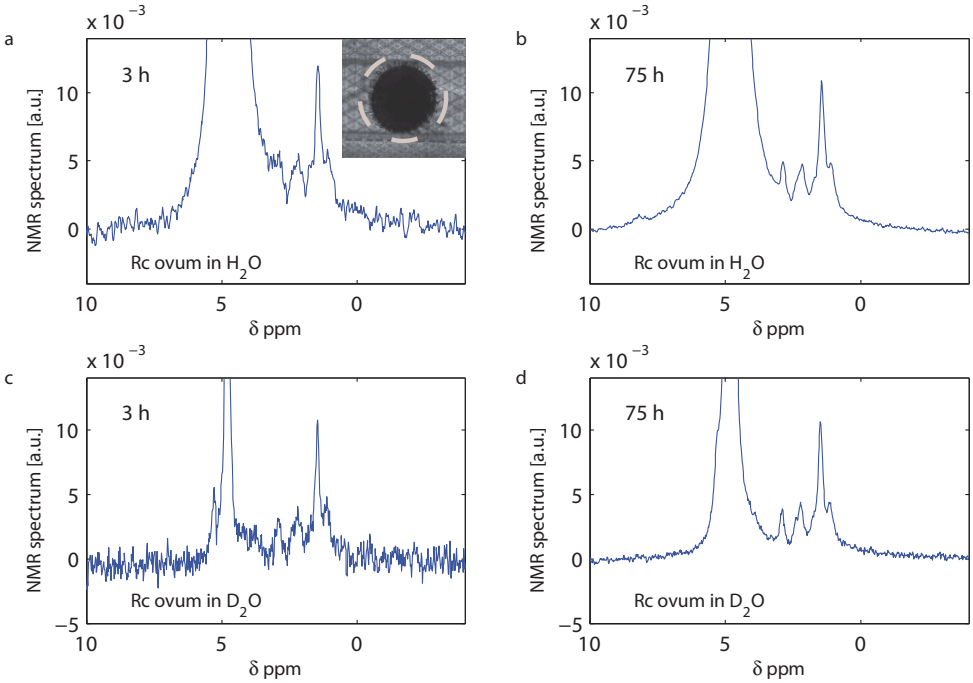

Figure 2.17: NMR measurements of a single *Rc tardigrade* ovum, performed at 7 T (300 MHz). The spectra are FFT real parts. The dashed circle indicates the 150 µm outer diameter of the integrated coil. See definition of notations in figure 2.16. (a): ^{1}H spectrum of a single *Rc tardigrade* ovum in H_2O: V ~150 pL; Avg = 28416; T_R = 200 ms, τ = 3.5 µs, T_m = 30 ms. (b): ^{1}H spectrum of a single *Rc tardigrade* ovum in D_2O: V ~ 150 pL; Avg = 1350000; T_R = 200 ms, τ = 3.5 µs, T_m = 30 ms. (c): ^{1}H spectrum of a single *Rc tardigrade* ovum in D_2O: V ~ 150 pL; Avg = 28416; T_R = 200 ms, τ = 3.5 µs, T_m = 30 ms. (d): ^{1}H spectrum of a single *Rc tardigrade* ovum in D_2O: V ~ 150 pL; Avg = = 1350000; T_R = 200 ms; τ = 3.5 µs; T_m = 30 ms.

laevis[110, 121] and hen eggs[122]. The spectra showed in Fig. 2.17 indicate that we can associate the nature of the dominant peaks in the *Rc* ovum (i.e. the peaks at 0.9, 1.3, 2.1, 2.8 ppm) to the yolk lipid content of the sample. Curiously, signals at the SNR limit are visible in the aromatic region (at about 8 ppm) only when the sample is submerged in H_2O. However, the SNR is still too weak to estimate any feature of the signals present in this chemical shift region.

2.7.5 NMR measurements of a single *C. elegans* subsection

After trapping the worm using S medium[120], a gentle flow of S medium and *E.coli* (1.5 x 10^9 cell/mL) is applied to provide food to the *C. elegans*. At this point the flow is stopped and the fluidic connection clamped for sealing.

The *C. elegans* goes through a squeezing process to be able to enter the microchannel whose size tightly matches the one of the worm. It follows that, in good approximation, only the worm is present in the active area of the detector. Nevertheless, a measurement of the *E. coli* solution is performed to characterize the background signal that may contribute to the spectrum obtained from the *C. elegans* subsection. Figure 2.18 shows the ^{1}H NMR spectrum of *E. coli* in S medium at a concentration of 1.5 x 10^9 cell/mL, obtained after 11 h of average. The peaks at 1.3 and 3.7 ppm may be associated respectively to the glucose and lactate content, as suggested in Ref. 123.

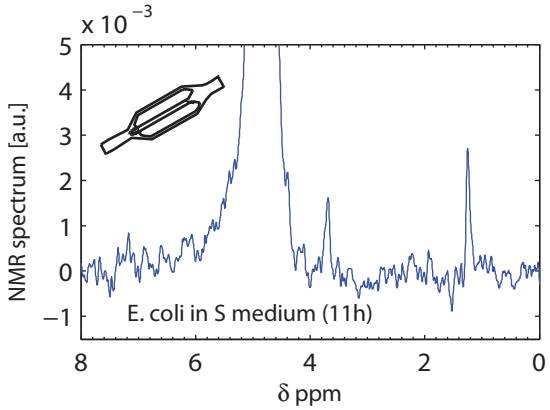

Figure 2.18:^{1}H NMR spectrum of *E-coli* (1.5 x 10^9 cell/mL) in S medium performed at 7 T (300 MHz). See definition of notations in figure 2.16. $V \sim 100$ pL; $Avg = 19800$; $T_R = 2$ s , $\tau = 3.5$ µs, $T_m = 60$ ms.

Fig. 2.19 shows NMR spectra obtained from a single *C. elegans* subsection with active volume of 100 pL. All the spectra are acquired from the same worm. For this experiment, we decided to align the subsection of the worm containing ova with the integrated detection microcoil. As shown in Fig. 2.19a (inset), most of the sensitive region is indeed occupied by about eight eggs contained in the *C. elegans* abdomen. The resulting spectrum has features which are similar to those measured in the *Rc* eggs.

Acceptable SNR can be obtained averaging over 12 h as shown in Fig. 2.19a. Figure 2.19b shows the spectrum obtained after averaging over 60 h. A zoom of the same spectrum is shown in Fig.

2.19c. Figure 2.19d shows ^{1}H NMR spectra acquired after 12 h of averaging. The spectrum in blue is acquired soon after the trapping of the worm, the spectrum in red is acquired after 12 h of measurement, while the spectrum in green is obtained from the measurement performed after 24 h from the loading of the *C. elegans*.

The three spectra are slightly different; this may be due to degradation of the sample as well as to a reallocation of the worm subsection with respect the sensitive area of the detector. However, the SNR is too weak for any claim on the spectra evolution. To clarify this point an improvement of the filling factor and further measurements on different worms would be needed.

The peaks assignment is challenging due to the reduced size of the samples combined with the relatively poor spectral resolution. The peaks observed at about 0.9, 1.3, 2.1, 2.8 ppm may be mainly associated to yolk lipids. Some qualitative information can be obtained from previous ^{1}H HRMAS NMR studies on a collection of *C. elegans*[12] and on a single worm[58].

A prominent signal arises at a chemical shift of about 3.7 ppm. As shown in the Fig. 2.18, the same resonance appears in the spectrum of *E.coli* in S medium, which is used as a base to feed the worm during the experiment. Therefore, we suspect that such resonance may result from the ingestion of nutrients operated by the microorganism.

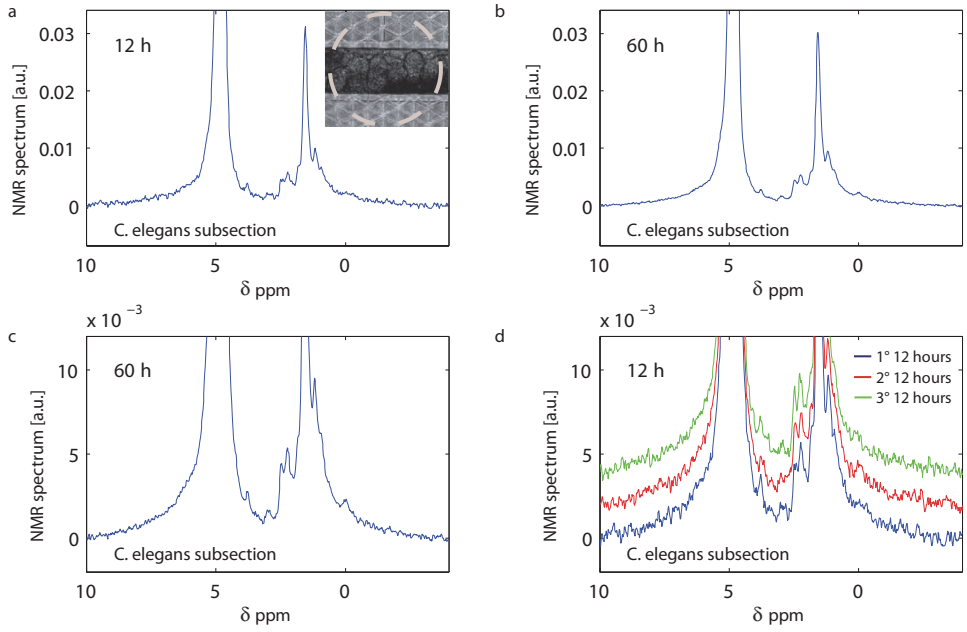

Figure 2.19: NMR measurements of a single *C. elegans* subsection performed at 7 T (300 MHz). The dashed circle indicates the 150 µm outer diameter of the integrated coil. The spectra are FFT real parts. See definition of notations in figure 2.16. (a): $V \sim$ 100 pL; Avg = 216000; T_R = 200 ms; τ = 3.5 µs; T_m = 30 ms. (b): $V \sim$ 100 pL; Avg = 1080000; T_R = 200 ms; τ = 3.5 µs; T_m = 30 ms. (c): $V \sim$ 100 pL; Avg = 1080000; T_R = 200 ms; τ = 3.5 µs; T_m = 30 ms. (d): $V \sim$ 100 pL; Avg = 216000; T_R = 200 ms; τ = 3.5 µs; T_m = 30 ms.

2.7.6 Sensitivity of the single-chip probe and limit of detection

The time-domain free-induction decay signal after an excitation pulse can be written as[124]:

$$S(t) = S_0 e^{-i2\pi\upsilon_0 t} e^{\frac{-t}{T_2^*}}, \quad (2.1)$$

where υ_0 is the Larmor frequency and S_0 is the signal amplitude at $t = 0$, T_2^* is the effective transversal relaxation time resulting from dipolar interactions and field non-uniformities.

$$\frac{1}{T_2^*} = \frac{1}{T_2} + \gamma \Delta B_0, \quad (2.2)$$

where T_2 is the transversal relaxation time and ΔB_0 is the inhomogeneity of the static magnetic field over the sample volume.

The linewidth FWHM $\Delta\upsilon$ corresponds to

$$\Delta\upsilon = \frac{1}{\pi T_2^*}. \quad (2.3)$$

The Fourier transform of the time domain signal resulting from the acquisition over a time T_{acq} is equal to

$$S(\upsilon) = S_0 \int_0^{T_{acq}} e^{-i2\pi\upsilon_0 t} e^{-i2\pi\upsilon t} e^{\frac{-t}{T_2^*}} dt, \quad (2.4)$$

The maximum line amplitude is obtained at resonance ($\upsilon = \upsilon_0$) and is equal to

$$S(\upsilon_0) = S_0 T_2^* \left(1 - e^{\frac{-T_{acq}}{T_2^*}}\right). \quad (2.5)$$

The time domain root mean squared noise (n_{RMS_t}) is[124]

$$n_{RMS_t} = n_{SD}\sqrt{\Delta F}, \quad (2.6)$$

where n_{SD} represents the noise spectral density and ΔF the detection bandwidth.

The frequency domain root mean squared noise (n_{RMS_f}) is[124]

$$n_{RMS_f} = n_{SD}\sqrt{T_{acq}}. \quad (2.7)$$

The signal-to-noise ratio in the time-domain (SNR_t) and in the frequency-domain (SNR_f) can be defines as[124]:

$$SNR_t = \frac{S_0}{n_{RMS_t}} = \frac{S_0}{n_{SD}\sqrt{\Delta F}} \quad (2.8)$$

$$SNR_f = \frac{S_i(0)}{n_{RMS_f}} = \frac{S_0 T_2^* \left(1 - e^{\frac{-T_{acq}}{T_2^*}}\right)}{n_{SD}\sqrt{T_{acq}}} \quad (2.9)$$

The time-domain spin sensitivity N_{min_t} is

$$N_{min_t} = \frac{N}{SNR_t\sqrt{\Delta F}} \quad (2.10)$$

where N is the number of nuclear spins contained in the sample under investigation. From (2.8), (2.10) becomes

$$N_{min_t} = \frac{Nn_{SD}}{S_0} = \frac{N_s V_s n_{SD}}{S_0}, \quad (2.11)$$

where N_s is the spin density and V_s is the sample volume. N_{min_t} can be defined as the number of nuclear spins, contained in a volume V_s, that gives an SNR of 1 considering an equivalent detection bandwidth $\sqrt{\Delta f}$ of 1 Hz. It is expressed in spins/$\sqrt{\text{Hz}}$ or mol/$\sqrt{\text{Hz}}$.

The limit of detection (LOD_f) or frequency-domain spin sensitivity defines the number of spins that are detectable with a SNR_f of 3, is expressed in spins $* \sqrt{\text{s}}$ or mol $* \sqrt{\text{s}}$ and is equal to:

$$LOD_f = 3\frac{N_i}{SNR_f}\sqrt{T_{acq}} \quad (2.12)$$

Where N_i represents the number of spins in the sample which contributes to the frequency-domain signal of the chosen peak *i*. From (2.9), (2.12) becomes

$$LOD_f = 3\frac{N_i n_{RMS_f}}{S_i(0)}\sqrt{T_{acq}}. \quad (2.13)$$

The sensitivity can be optimized by applying an exponential time-domain filter with time constant T_m=T_2^* (*i.e.*, a multiplication by $exp(-t/T_2^*)$). Under this condition, (2.9) becomes[124]

$$SNR_f = \frac{S_0\sqrt{T_2^*}\left(1-e^{\frac{-2T_{acq}}{T_2^*}}\right)^{\frac{1}{2}}}{n_{SD}} \cong \frac{S_0\sqrt{T_2^*}}{n_{SD}}, \quad (2.14)$$

where the approximation holds for $T_{acq} \geq T_2^* = T_m$.

From (2.12) and (2.14), the limit of detection for a single acquisition such that $T_{acq} = T_2^*$ and using a match filter is equal to

$$LOD_f = 3N_i\left(\frac{S_0\sqrt{T_2^*}}{n_{SD}}\right)^{-1}\sqrt{T_{acq}} \cong 3N_{min_t} \quad (2.15)$$

In these conditions, the difference between the two definitions of sensitivity is only the factor 3 introduced, quite arbitrarily, in the definition of limit of detection in the frequency-domain.

For a number of acquisitions equal to N_{acq} spaced by a time $T_R > T_{acq} = T_2^*$, such that the magnetization recovers before a new excitation, LOD_f becomes

$$LOD_f = 3N_i\left(\frac{S_0\sqrt{T_2^*}}{n_{SD}}\right)^{-1}\sqrt{T_{Nacq}} = 3N_i\left(\frac{S_0\sqrt{T_2^*}}{n_{SD}}\right)^{-1}\frac{\sqrt{N_{acq}T_R}}{\sqrt{N_{acq}}} = 3N_{min_t}\sqrt{\frac{T_R}{T_2^*}}. \quad (2.16)$$

We determined the time-domain spin sensitivity N_{min_t} experimentally from the time-domain SNR_t of the spectrum of pure water acquired using the microchannels designed for the trapping of the *C.elegans*. The SNR_t of the peak of water, shown in Fig. 2.12a, considering an equivalent detection

bandwidth of 1 Hz, is equal to 250 for a single scan. In the case of pure water, the spin density N_s is equal to $6.68 \cdot 10^{25}$ spins/L. Considering an active volume V_s of 100 pL at a distance of 10 μm from the detector coil, the spin sensitivity N_{min_t} (calculated following (2.11)) is $2.5 \cdot 10^{13}$ spins/$\sqrt{\text{Hz}}$. For a cubic volume of 30 pL in direct contact with the surface of the chip, and included in the region of maximum sensitivity of the detector, the spin sensitivity N_{min_t} is about $1.5 \cdot 10^{13}$ spins/$\sqrt{\text{Hz}}$.

The time-domain spin sensitivity for a sample with an active volume of 100 pL and placed 10 μm away from the surface of the coil is 1.7 times smaller than the spin sensitivity calculated for a sample with active volume of 30 pL and placed in direct contact with the chip. This is in a good agreement with the expected reduction of sensitivity computed via the sensitivity maps shown in Fig. 1.1, for a sample-to-detector distance of 10 μm.

In the case of the NMR measurements of pure water ($T_1 \cong T_2 \cong 3$ s), performed using the microchannel designed for the trapping of the *C. elegans* worm, we have a linewidth FWHM of 2 Hz. From (2.3) the effective spin-spin relaxation time T_2^* is 0.16 s. The repetition time T_R is set to 4s. Under these conditions the frequency-domain limit of detection LOD_f, calculated from (2.16), is approximately 600 pmol $\sqrt{\text{s}}$ of ^{1}H nuclei.

For the measurements of pure water, performed employing the microchannels designed for the trapping of *Rc* ova, the LOD_f is approximately 1.3 nmol $\sqrt{\text{s}}$ of ^{1}H nuclei with a T_2^* of 0.03 s (*i.e.*, a 10 Hz FWHM line) and repetition time $\text{T}_R = 4s$.

For NMR measurements performed on biological entities (*i.e. Rc ova* and *C. elegans*), having linewitdhs of 30 Hz FWHM (*i.e.*, $T_2^* \cong 0.01\, s$) and measured with a repetition time $T_R = 0.2\, s$, the LOD_f is approximately 500 pmol $\sqrt{\text{s}}$ of ^{1}H nuclei, which correspond to 5 pmol of ^{1}H nuclei in an averaging time of 3 h.

2.7.7 Beyond the limit of sensitivity: single *C. elegans* egg

In this section we report the NMR spectrum on a single *C. elegans* egg in H_2O, obtained using the SU-8 microfluidic channel, the fluidic interface and the electronic set-up described respectively in section 2.2.1, 2.2.2 and 2.4. This measurement is performed to show the limit of sensitivity of the system. Possible solutions to address such a tiny sample (20 pL) are discussed in the paragraph.

C. elegans embryos were extracted from gravid worms using the following protocol (re-adapted from Ref. 120):

1. Wash the worm plate full of gravid worms with 750 μL of H_2O to collect all the worms and transfer them in an Eppendorf tube. Repeat this step twice on the same plate.

2. Add to this volume 150 μL of bleach and 280 μL of NaOH. This solution will kill and dissolve all the worms not protected by the egg shell.

3. Manually shake for about 4 min. Pour a droplet on a glass slide and check that no adult worms are left. Otherwise, repeat step 3.

4. Centrifuge at 5000 rpm, 3 min, 21 °C. The sedimented eggs are now at the bottom of the tube. Remove with a pipette 1400 µL of supernatant from the very top of the Eppendorf tube, to remove bleach and NaOH. Replace the same amount with S medium or H_2O. Repeat step 4 three times.

The SU-8 microchannel and tubing are filled with H_2O and *C.elegans* eggs are sucked up from the reservoir into a tube connected to the microfluidic device. In order to insert the eggs in the channel, a flow of 100 nL/s is applied. Being the height of the microchannel comparable with the egg dimensions, once the flow is stopped some of the eggs remain locked in the channel (inset Fig. 2.20).

Figure 2.20 shows a NMR measurement on a single *C. elegans* egg in H_2O, after averaging over 1 h. The excitation pulse length used in the reported experiments corresponds to the experimental condition of maximum sensitivity (τ = 4 µs). This sample, whose typical volume is about 20 pL, is clearly beyond the current limit of sensitivity of our detector. Although it is impossible to perform a peak assignment due the reduced signal-to-noise ratio (S/N), it is worth to mention that the weak peak at 1.3 ppm could be associated with lipids and lactate as suggested in Refs [8, 121, 125].

The extraction of the eggs from the adult *C. elegans* and the loading of the sample in the microchannel is time comsuming (approximately 3 h). Moreover, the *C. elegans* eggs in H_2O hatched after a few hours. These aspects preclude the use of longer measurement times to obtain a better SNR.

For a systematic study of this specimen, the development of a specific microfluidic structure is required. The device should contain a filtering system for the removal of beaching residues and a trapping system for blocking the egg in correspondence of the detector coil for the duration of the experiment. Moreover, a miniaturisation of the detector coil would be needed to maximize the filling factor, thus the sensitivity. With the implementation of this system we would expect an improvement of the SNR ratio of a factor 2 from the miniaturisation of the detector coil and a shortening of the sample preparation procedure that would enable longer measurement times (about 3 h). Furthermore, as explained in section 2.7.3, the repetition time can be decreased by a factor of 10; which implies 3 times shorter measurement time. The application of the modifications explained above would contribute to a total improvement of a factor of 10 in the SNR, which could be sufficient to detect highly concentrated endogenous compounds in a single *C. elegans* egg.

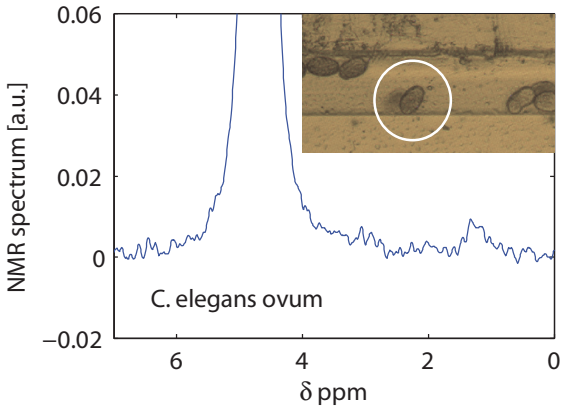

Figure 2.20: ^{1}H spectrum of a single *C. elegans* egg cell in H_2O: $V \sim 20$ pL; $Avg = 3600$; $T_R = 2$ s; $\tau = 4$ µs; $T_m = 20$ ms. The inset shows an optical microscope picture of *C. elegans* eggs trapped in the microfluidic channel. The circle indicates the coil external diameter (150 µm); a single egg is in the active sensitive area of the integrated coil.

2.8 Conclusion and outlook

In this chapter, we presented nuclear magnetic resonance (NMR) experiments on subnanoliter liquids and biological samples immersed in liquid enviroments. These measurements constitute a preliminary significant step towards the study of a multitude of biological entities present at the subnanoliter scale such as single cells, embryos and small living microorganisms[64]. The experiments were enabled by the fabrication of microfluidic structures, specifically conceived to guide and confine sub-nL samples in the sub-nL most sensitive volume of a single-chip integrated NMR probe.

We suggested two methods for the fabrication of microchannels, the former based on traditional microfabrication techniques, and the latter based on two-photon polymerization, a 3D printing technique with lateral resolution of 300 nm. Both of the methods allow for the realization of microfluidic structures that confine samples at distances smaller than 10 µm from the detector. The proximity between the microcoil and the sample confined in the microfluidic channel is crucial to preserve high effective spin sensitivity.

3D-printing-based microfabrication process is not suitable for large scale production, it allows to rapidly fabricating complex microfluidic structures tailored to position, hold, and feed microorganisms, with a design that maximizes the NMR signals amplitude and minimizes the static magnetic field inhomogeneities.

We reported NMR measurements on sub-nL samples (and sub-nL portion of larger samples) having significantly different size, geometry, and nature. We showed experiments on liquids, where we showed spectral resolutions down to 0.007 ppm FWHM (*i.e.*, about 2 Hz at 300 MHz) in liquid samples of 100 pL. Additionally, we reported experiments on two radically different biological entities, *i.e.* tardigrade *Richtersius coronifer* ova and *C. elegans* worms. Despite the tiny size (about 100 pL) and the broad intrinsic linewidth (about 30 Hz at 300 MHz) of these samples,

the achieved sensitivity ($2.5 \cdot 10^{13}$ spins/$Hz^{1/2}$) is sufficient to detect highly concentrated endogenous compounds with measurements times down to 3 hours.

The microfluidic channels are connected to a robust fluidic interface that tolerates the application of flows as strong as 7 μL/s and guarantees an efficient sealing for several days (tested up to two weeks). The results of the reported experiments indicate that the approach proposed here allows for the non-invasive and efficient handling and trapping of living entities for NMR investigations at the sub-nL volume scale, in conditions of high sensitivity and sample limited spectral resolution.

In our experimental conditions, using a 7 T field, a microcoil with active volume of 0.25 nL, a spectral resolution of about 30 Hz FWHM and repetition time equal to 200 ms, the frequency-domain limit of detection is approximately 18 pmol in 60 min. Working at 23.5 T (the highest field commercially available) would improve the sensitivity by a factor 6[112], with a LOD_f of about 3 pmol in 60 min.

Previous studies of extracellular culture media report that the uptake or production rate of metabolites in human oocytes (e.g. glucose, pyruvate and lactate) change during the developmental stages and can reach 50 pmol/h per single oocyte[126]. These results suggest that, with the employment of a higher field, the sensitivity of our detector may be high enough to address NMR analysis on a single oocyte. These investigations could contribute to the in-vivo study of metabolic processes and the development of a single embryo, essential for the amelioration of in vitro fertilization.

The combination of CMOS integrated NMR detectors with high spatial resolution 3D printed microfluidic structures is compatible with the implementation of arrays of miniaturized probes, which would enable simultaneous studies on a large number of single biological entities in the same magnet. This would, in turn, allow for systematic investigation of the heterogeneity among individuals or among different subsections of a single organism (such as a *C. elegans* worm), as well as of their response to different environmental conditions or drugs.

Chapter 3 EPR spectroscopy of sub-nanoliter liquid samples and frozen solutions

Electron paramagnetic resonance (EPR) spectroscopy studies molecular systems with unpaired electrons (paramagnets). Although there are more molecules without unpaired electrons (diamagnets) than with unpaired electrons, paramagnets of particular interest exist. EPR spectroscopy is an important and extensively used tool in chemistry, biology, medicine, physics, and materials science. This technique is, for example, the method of choice to determine distances between paramagnetic centers in enzymes, to measure the oxygen concentration in living tissue, to study the dynamics of proteins or to analyse in vivo pathological conditions caused by the presence of free radicals[25, 27-35].

Though EPR spectra of biologically relevant samples should be ideally acquired from an acqueous solution at physiological temperatures, bio EPR spectroscopy is often performed on frozen samples. In fact, paramagnetic relaxation of many transition ions is usually fast at ambient temperature, leading to spectra broadened beyond detectability. Lowering of the temperature reduces the relaxation rate, and this leads to a sharpening of the spectra.

3.1 Introduction

EPR investigation of subnanoliter volumes would open up the possibility of studying volume-limited liquid samples available only in small quantities (e.g. proteins which cannot be grown in bigger sizes) and single biological entities. Addressing samples at the microscale involves two main challenges: (i) the sensitivity of the EPR detector and (ii) the handling of the sample.

- The sensitivity of the detector: a miniaturization of the detector is needed to match the size of the sample, thus maximizing the filling factor and increasing the sensitivity. Previous work demonstrated the use of complementary metal-oxide semiconductor (CMOS) to realize electron paramagnetic resonance (EPR) miniaturized high sensitive inductive probes[2, 101]. These integrated systems use integrated planar coils with a diameter of 180 μm and are optimized for the detection of sample volumes of approximately 300 pL.

- The handling of the samples: with the miniatiurization of the detector, the positioning of the specimen becomes more difficult. A precise placement of the sample in close vicinity

of the detector is necessary to fully exploit the high sensitivity of the integrated detector coil. Interfacing a microfluidic structure with the CMOS single chip EPR detector would permit EPR experiments on subnanoliter liquid samples and biological entities immersed in a liquid environment.

In this chapter we report an approach to place and hold liquids in proximity of a miniaturized EPR detector, allowing experiments on subnanoliter active volumes. EPR experiments on frozen solutions are implemented, to demonstate the capability of the system to perform measurements at cryogenic temperatures. All the EPR measurements are performed at 21 GHz.

3.2 Experimental set-up

Microfabricated and 3D printed microfluidic structures can be interfaced with the CMOS single chip EPR detector following the same procedure reported in the previous chapter. Differently, in this section we present a third approach that is based on the use of a capillary combined with the EPR integrated detector. Microcapillary of several shapes, dimensions and materials are commercially available and can be evaluated as an alternative approach to microfabricated microfluidic systems. This solution does not require microfabrication processes, but the fixed geometry of the microcapillary prevents the optimization of the filling factor, as well as further customization of the detection system.

Details of the single chip EPR detector used in the experiments are reported in Ref. 2. The chip is realized with a 130 nm CMOS technology (IBM) and it has an area of about 1 mm^2. The single turn excitation/detection coil integrated on the chip has an outer diameter of 180 μm.

Figure 3.1a shows the rendering of the EPR single chip detector with a capillary positioned on top of the detector coils.

Fig 3.1b shows an illustration of the approach used to drive the liquid sample to the sensitive area of the detector. A commercially available borosilicate glass capillary (CM scientific Ltd) is used; it has a squared 50 x 50 μm^2 cross-section and 25-μm-thick walls, which correspond to the distance between the sample and the surface of the detector. The coil lies in the *yz* plane and the static magnetic field B_0 is applied along the z axis.

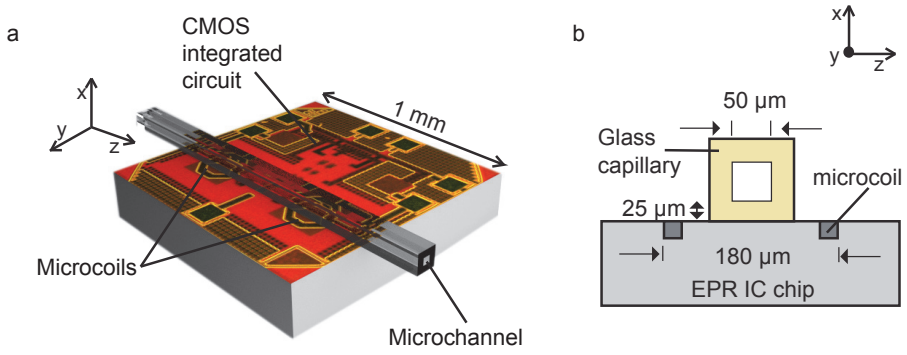

Figure 3.1: Illustration of the approach used to place the liquid sample in close proximity of the most sensitive area of the on-chip excitation/detection microcoil. The coil lies in the *yz* plane with the static magnetic field B_0 along the *z* axis. (a) Rendered image of the CMOS integrated circuit combined with a microcapillary. (b) A glass capillary is placed on top of the EPR IC chip. The separation between the sample and the detector planar coil is 25 µm, corresponding to the wall thickness of the capillary.

3.2.1 Fluidic interface

The micro-to-macro interface between the commercially available glass capillary and the IC chip is shown in Fig. 3.2. To complete the fluidic system, the capillary is connected to tubes through plastic needles (560105-1/2, Sicher & Praziser) and silicone glue (RTV118, Momentive Performance Materials Inc.).

The fluidic system is mounted onto an inverted microscope (Axio Observer, Zeiss) equipped with a precisExcite High-Power LED Illumination system (Visitron, Puchheim) for brightfield imaging. The microfluidic operations are controlled using Nemesys syringe pumps and relative control software (Cetoni, Korbussen). Once the sample is loaded in the capillary, the flow is stopped, the tubes are clamped and the fluidic system is aligned under a microscope and then blocked above the excitation-detection coil using silicone glue, as shown in Fig. 3.1a.

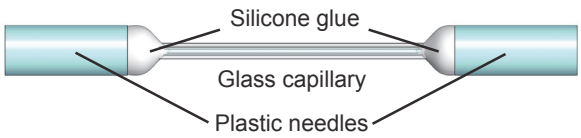

Figure 3.2: Illustration of the fluidic interface between the commercially available capillary and tubes through silicone glue and plastic needles. The fluidic connected capillary is placed and fixed with silicone glue above the integrated microcoil.

3.2.2 Electronic set-up

Figure 3.3 shows an illustration of the EPR experimental set-up. The chip is wire bonded on a PCB and the glass capillary is aligned with the integrated microcoil. The PCB is inserted into an electromagnet (Bruker, 0-2 T). The signal at the output of the chip is buffered using a commercial amplifier (THS4304) and mixed with a RF signal at about 200 MHz. The downconverted signal has a frequency of about 10 MHz. A phase-locked loop (PPL) is used for frequency-to-voltage conversion. The PLL frequency-to-voltage conversion factor is 1 μV/Hz and the integrated frequency division is 16. To improve the signal-to-noise ratio, a magnetic field modulation at kHz frequencies is added to the static magnetic field. The signal at the output of the PLL is demodulated by a lock-in amplifier. The lock-in internal reference signal is amplified and applied to the field modulation coil. The measurements at 77 K are performed by immersing the single-chip EPR probe, interfaced with the glass capillary, into a liquid nitrogen dewar.

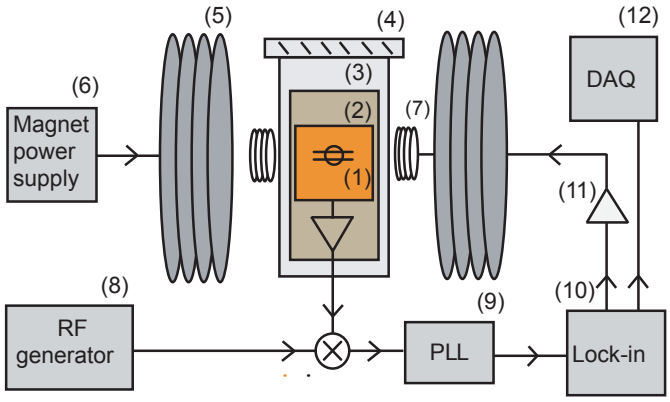

Figure 3.3: Schematic of the experimental set-up used for EPR measurements. (1) Integrated excitation/detection coil interfaced with the glass capillary. (2) Single chip EPR detector (see details in Ref. 2). (3) Printed circuit board (PCB), buffer (THS4304D, Texas Instrument) mounted on the PCB. (4) Liquid nitrogen dewar. (5) Electromagnet (0-2 T, Bruker). (6) Electromagnet power supply (0-150A, Bruker). (7) Magnetic field modulation coil. (8) RF source (SMR-20, Rohde-Schwarz). (9) PLL circuitry. (10) Lock-in (7260, EG&G Instruments). (11) Power amplifier (PA508, Rohrer). (12) Multifunctional board (PCIe-6259, National Instruments).

3.3 EPR measurements of subnanoliter liquid samples and frozen solutions

EPR experiments are performed using the glass capillary interfaced with the single chip EPR detector via the fluidic interface described in Fig. 3.2. Details of the principle of operation and the electronic circuitry of the single-chip detector used to perform EPR experiments are reported in Ref. 2. The presence of a resonating sample placed over the integrated microcoil causes a change in the inductance of the microcoil. The magnetic resonance is detected by measuring the variation of the frequency of the integrated LC oscillator as a function of the applied static magnetic field. More details on the electronic set-up are given in section 3.2.2.

For a microwave magnetic field B_1, sufficiently low to avoid saturation, the signal contribution per elementary volume $dS(\boldsymbol{r})$ is proportional to $B_{uxy}(\boldsymbol{r})^2$, where $B_{uxy}(\boldsymbol{r}) = \left(B_{ux}^2 + B_{uy}^2\right)^{\frac{1}{2}}$. This dependence is used to evaluate the sensitivity of the EPR coil with the magnetic field $B_{uxy}(\boldsymbol{r})$ calculated using a Biot-Savart based code implemented in Matlab, as explained in details in section 1.3.2.

If we define the active volume as the fraction of the sample that contributes to the 70% of the total signal and we consider the geometry of the capillary and its position with respect to the microcoil, we estimate an active volume of about 200 pL.

The total integrated EPR signal S can be determined by integrating $dS(\boldsymbol{r})$ over the whole active volume. Considering $S_{(d=0\mu m)} = 1$ for the ideal case of the sample placed in direct contact with the chip, the EPR signal $S_{(d=25\mu m)}$ is equal to 0.5. Thus, for a sample volume placed at a distance of 25 μm from the detector surface, the loss in signal is equal to 50%, with respect to the ideal case where the sample is placed in direct contact with the chip surface. This shows again the importance of having the sample close to the detector coil.

3.3.1 EPR measurements of subnanoliter liquid samples

Fig. 3.4 shows a collection of spectra obtained from aqueous solutions of the free radical TEMPO (4-Hydroxy-TEMPO, Sigma-Aldrich). The experimental EPR signal, in kHz, is the amplitude at the field modulation frequency of the LC-oscillator frequency (21 GHz) computed from the experimental signal at the output of a lock-in amplifier. The experimental conditions are specified in the figure caption.

The experimental data at TEMPO concentration of 1 mM (Fig. 3.4a) and 10 mM (Fig. 3.4b) are reported. The measured EPR spectra are in agreement with those reported in literature[127].

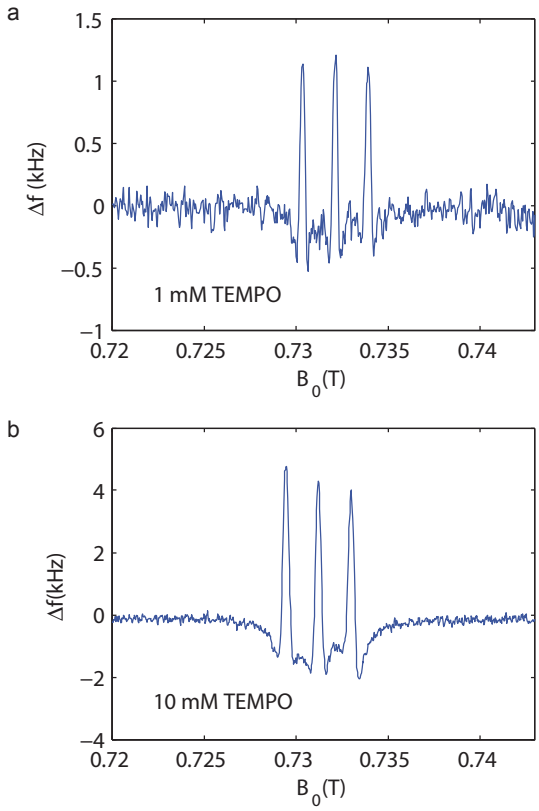

Figure 3.4: EPR measurements on room temperature solutions, performed at 21 GHz. All the EPR spectra are single scan measurements and relative to an active volume of about 200 pL. Experimental condition notation: T is the sample temperature, ν_m is the frequency of the magnetic field modulation, B_m is the amplitude of the modulation magnetic field, B_1 is the microwave magnetic field. (a) 1 mM TEMPO in H_2O: T = 297 K, ν_m = 101.3 kHz, B_m = 0.49 mT, B_1 = 0.06 mT. (b) 10 mM TEMPO in H_2O: T = 297 K, ν_m = 101.3 kHz, B_m = 0.49 mT, B_1 = 0.06 mT.

3.3.2 EPR measurements of frozen solutions

Many paramagnetic ions in biological samples have such high relaxation rates that their spectra are too broad to be measured at room temperature[128]. Hence, EPR of frozen solutions can enable the investigation of a larger panel of samples. To demonstrate the capability of the system to perform EPR investigation at cryogenic temperature, we report the frozen solution spectrum of 15 mM Gd_3Cl in H_2O (G7532 Gadolinium (III) chloride hexa-hydratate, Aldrich) at 77 K (Fig 3.5). Gd^{3+} is a promising alternative to the commonly used nitroxide spin labels for the measurement of interspin distances. The gadolinium magnetic moment is seven times bigger than the one of the nitroxide thus leading to longer-range dipolar interactions[129].

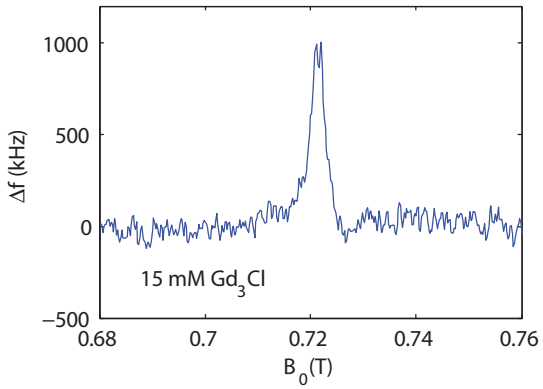

Figure 3.5: EPR spectrum of 15 mM Gd_3Cl in H_2O, performed at 21 GHz and at 77 K. The spectrum is a single scan measurement and relative to an active volume of about 200 pL. Experimental condition notation: υ_m is the frequency of the magnetic field modulation, B_m is the amplitude of the modulation magnetic field, B_1 is the microwave magnetic field. υ_m = 101.3 kHz, B_m = 0.16 mT, B_1 = 0.12 mT.

3.3.3 Sensitivity of the single-chip probe

The spin sensitivity N_{min}, defined as the number of electron spins that gives an SNR equal to 1, is equal to[101]

$$N_{min} = \frac{N_S V_S}{SNR\sqrt{\Delta F}}, \qquad (3.1)$$

where N_s is the spin density, V_s is the sample volume and $\sqrt{\Delta F}$ is the detection bandwidth.

We determined the spin sensitivity N_{min} experimentally from the SNR of the EPR spectrum of 1 mM aqueous solution of the free radical TEMPO. The SNR, shown in Fig. 3.4a, is equal to 93. Considering a detection bandwidth ΔF of 2.5 Hz and an active volume V_s of 200 pL, the spin sensitivity N_{min} is about $8{\cdot}10^8$ spins/$\sqrt{\text{Hz}}$. The EPR spectra are not infinitely sharp, they are broadened by relaxation, unresolved hyperfine splitting or distributions in g factor value over the sample volume. For a precise determination of the spin sensitivity, the effective linewidth of the EPR signal needs to be considered. The spin sensitivity $N_{min\Delta B}$ in function of the linewidth ΔB, measured at half height of the resonance, can be expressed by:

$$N_{min\Delta B} = \frac{N_S V_S}{SNR\sqrt{\Delta F}\Delta B} \qquad (3.2)$$

$N_{min\Delta B}$ determined from the EPR spectrum of 1 mM aqueous solution of the free radical TEMPO is equal to $2.9{\cdot}10^8 \frac{\text{spins}}{\sqrt{\text{Hz}}\,G}$.

The SNR of the EPR spectrum of 10 mM aqueous solution of TEMPO is equal to 587. For this value the calculated spin sensitivity is about $1.2{\cdot}10^9$ spins/$\sqrt{\text{Hz}}$. The spin sensitivity expressed in function of the linewidth $N_{min\Delta B}$ equals to $3{\cdot}10^8 \frac{\text{spins}}{\sqrt{\text{Hz}}\,G}$.

3.4 Conclusion and outlook

In this chapter we showed EPR measurements on subnanoliter room temperature and frozen solutions by a combination of glass microcapillaries and single chip CMOS EPR detectors. Commercially available capillaries are a good solution for EPR analysis on sub-nL liquid samples, when the customization of the microfluidic structure is not required.

We demonstrated the capability of the system (*i.e.* CMOS EPR detector, microcapillary, fluidic interface) to withstand cryogenic temperature, by performing experiments on subnanoliter frozen solutions. This is essential for the investigation of biological samples with short spin-spin relaxation times, where the EPR spectra would be too broad to be detected at room temperature[128].

The development of a specific microfluidic structure could potentially open up new ways of detecting free radicals in single living cells grown in a microfluid channel under cell-culture conditions. This is an ambitious goal if we consider that the typical concentrations of free radicals generated by cells during their regular metabolism are from nM to pM[130], which correspond respectively to about 10^5 and 10^2 spins in a sample volume of 100 pL (to about 10^4 and 10 spins in a sample volume of 10 pL). However, this target could be envisioned by increasing the operation frequency, decreasing the resonator diameter to maximize the filling factor for single cell experiments and performing the measurements at cryogenic temperatures (down to 4 K) to detect short-lived radical species.

Chapter 4 FMR of single magnetic beads

Magnetic nanoparticles and microparticles (beads) have enabled the development of a variety of applications in medical diagnostic and biological research[131]. Functionalized magnetic beads are commercially available and widely used to selectively label biological targets. Magnetic labels have several advantages over other labels. Among these they are stable over time and can be easily manipulated by an external magnetic field. Thus, they can be conveniently used to position or selectively filter biological material attached to them[132].

4.1 Introduction

Several magnetic sensors were used to measure the concentration of the magnetic beads, which corresponds to the concentration of the labeled biological targets[133-138]. Measurements of single beads were demonstrated using giant magnetoresistance (GMR)[135] over a sensing area of 10^4 μm^2, miniaturized Hall sensors with a sensing area of 8 μm^2 [136], on-chip 1 GHz LC oscillators with a sensing area of about 10^4 μm^2. LC oscillators provide a sensitive detection of the beads by measuring changes in the magnetic susceptibility[133, 134] at zero static magnetic field.

We report an alternative method for the detection of magnetic beads that is based on the detection of their ferromagnetic resonance (FMR) by a CMOS integrated circuit detector. The main advantage of this sensing technique is that the change of susceptibility is measured in ferromagnetic resonance condition. Due to the frequency and field dependence of the susceptibility[139], the detected variation is about 20 times greater than the respective change in static magnetization detected by other approaches[133, 140]. The developed solution allows for single bead sensitivity over an active area of about 5 x 10^4 μm^2, and is compatible with integration of microfluidics and array of CMOS detectors.

4.2 Experimental

In this section we present the FMR detection of magnetic beads. Dynabeads M-270, superparamagnetic polymer beads with a diameter of 2.8 μm, are used for the measurements. They consist of Fe_2O_3 and Fe_3O_4 nanoparticles, with a diameter of 8 nm, dispersed in a polystyrene matrix. The ferromagnetic resonance is detected by measuring the variation of the frequency of the 21 GHz LC oscillator, induced by the presence of the bead, as a function of the applied static

magnetic field. Details of the experimental set-up are reported in section 3.2.2. Fig. 4.1 shows the rendering of the CMOS single chip detector with an off-scale illustration of the bead placed in the center of the excitation/detection microcoil.

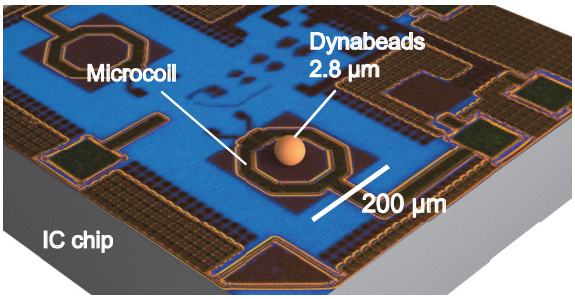

Figure 4.1: Illustration of a magnetic bead (not in-scale) placed on the active area of the on-chip detection coil. The coil lies in the *yz* plane with the static magnetic field B_0 along the *z* axis.

For a microwave magnetic field B_1, sufficiently low to avoid saturation, the signal contribution per elementary volume $dS(\boldsymbol{r})$ is proportional to B_{uxy}^2 as explained in section 1.3.2. This dependence is used to evaluate the sensitivity map of the detector coil using a Biot-Savart based code implemented in Matlab.

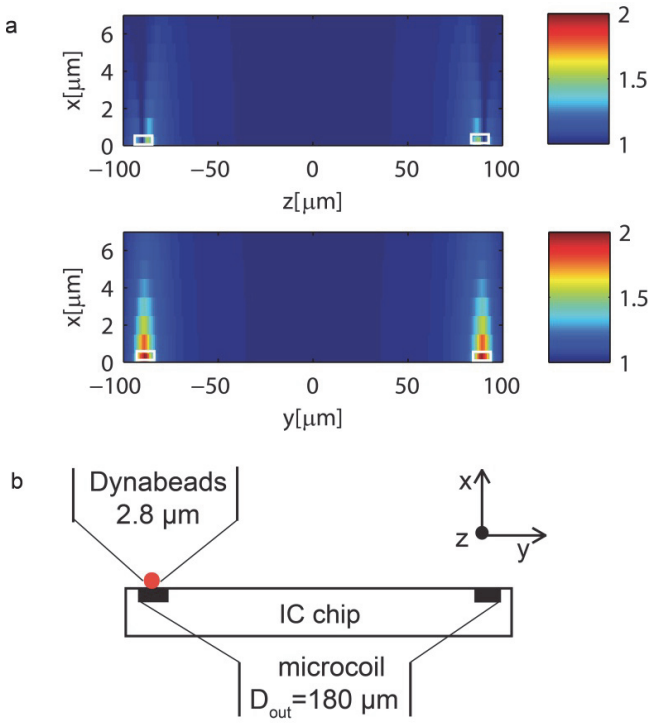

Figure 4.2: (a) Map of the sensitivity for the FMR integrated microcoil in the xz (top) and xy (bottom) planes computed via a Biot-Savart based code implemented in Matlab. The FMR signal contribution is proportional to B_{uxy}^2 , where $B_{uxy} = \left(B_{ux}^2 + B_{uy}^2\right)^{\frac{1}{2}}$ is the unitary field produced by the coil. The white rectangles indicate the position of the coil. (b) Illustration (not in scale) of a magnetic bead placed on the metal of the on-chip excitation/detection microcoil. The coil lies in the *yz* plane with the static magnetic field B_0 along the *z* axis.

Figure 4.2a shows the maps of sensitivity respectively in the *xz* (top) and *xy* (bottom) plane and in close proximity of the chip surface. For clarity of illustration, the two axes of the graphs are not in scale; the white rectangules indicate the position of the coil. The actual distance between the bead and the coil is approximately 2 μm, corresponding to the thickness of the oxide passivation layer on top of the coil. In this configuration, the signal contribution in the volume occupied by the bead is about 1.5 times greater than the value we would have if the bead was placed in the center of the coil. Fig. 4.2b shows the illustration (not in scale) of a magnetic bead placed on the metal of the on-chip excitation/detection microcoil.

4.2.1 Sample preparation and single bead isolation

Dynabeads M-270 are supplied in phosphate buffered saline (PBS) at a concentration of 10 mg/mL. With the aim of isolating and placing the magnetic beads on top of the integrated excitation/detection microcoil, we follow the procedure described below.

The solution of magnetic beads is diluted in H_2O to obtain a concentration of 1 μg/mL. With the use of a pipette, 0.1 μL of diluted solution is transferred onto a 5 μm-thick Mylar foil. After the evaporation of the solvent, the Mylar foil is flipped upside down and the surface containing the beads is approached to the CMOS single chip detector.

The beads are aligned with the detector under an optical microscope and transferred onto the chip by gently pressing the Mylar foil with a swab into contact with the chip surface. Finally, an eyelash is stuck with adhesive tape on a tungsten tip of a micromanipulator which is used to position the beads on top of the integrated detection coil and to move the beads in excess away from the sensitive area of the detector.

4.2.2 FMR measurements of magnetic beads

In this section, we present FMR experiments of magnetic beads (Dynabeads M-270) in the configuration illustrated in figure 4.2b. The experimental FMR signal, in Hz, is the amplitude at the field modulation frequency of the LC-oscillator frequency (21 GHz) computed from the experimental signal at the output of a lock-in amplifier. The experimental conditions are specified in the figure caption.

The experimental data related to the measurement of 13 beads (Fig. 4.3a), 2 beads (Fig. 4.3b) and single bead (Fig. 4.3c) are reported. To improve the SNR a magnetic field modulation is applied at the site of the sample. The SNR increases with higher magnetic field modulation amplitudes; however, if the modulation amplitude is too large the detected FMR signal broadens and becomes distorded. A good compromise between SNR and signal distortion occurs when the amplitude of the magnetic field modulation is equal to the width of the FMR signal.

The high sensitivity of the detector combined with the large active area allows for the detection of up to 4000 beads with a resolution down to one single bead, as shown in Fig. 4.3c.

Due to the broad resonance line of the magnetic beads (80 mT), the main limitation in the SNR is given by the maximum magnetic field modulation achievable with our current setup (1.1 mT).

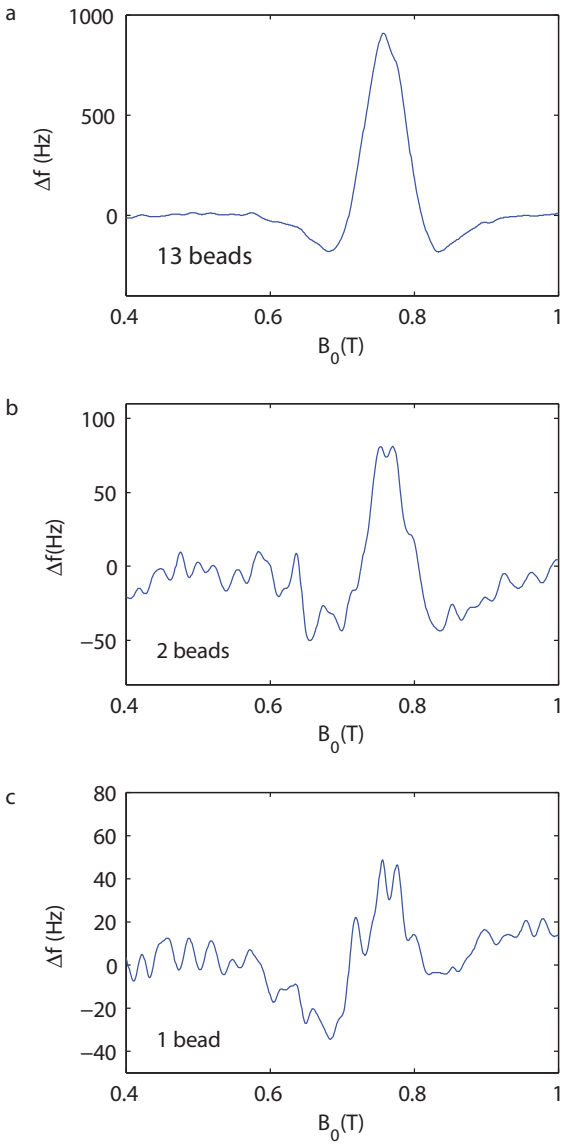

Fig. 4.3: FMR measurements of magnetic beads, performed at 21 GHz. Magnetic beads (Dynabeads, 2.8 μm) are placed on the metal coil with the help of a micromanipulator. The number of sweeps is equal to 25. Experimental condition notation: υ_m is the frequency of the magnetic field modulation, B_m is the amplitude of the modulation magnetic field, B_1 is the microwave magnetic field. υ_m = 101.3 kHz, B_m = 1.1 mT, B_1 = 0.06 mT. The effective time constant of the lock-in is 3 s. (a) 13 beads. (b) two beads. (c) single bead.

4.3 Conclusion and outlook

In this chapter we showed a novel method for the sensing of magnetic beads, based on the detection of the change in susceptibility in ferromagnetic resonance (FMR) conditions. The main advantage of this method is that, due to the frequency and field dependence of the susceptibility[139], the detected variation is about 20 times greater than the change in magnetization in static conditions sensed by other approaches[133, 140].

Using a single chip CMOS detector, we reported the detection of a single bead, as well as *n* beads with an active area of about 5 x 10^4 μm^2. This is an improvement compared to previously reported magnetic bead detection schemes[133-138], which suffer either from a limited sensitivity, or from limited sensing area.

To maximize the SNR a magnetic field modulation, with amplitude equal to the width of the FMR signal, should be applied. The maximum amplitude of the magnetic field modulation achievable with our current set-up is equal to 1.1 mT, while the width of the magnetic beads FMR signal is equal to 80 mT. Shrinking the size of the modulation coils would enable a higher modulation field, with an increase in the SNR up to a factor of 30, if a 30 G modulation field is produced (as in the newly installed magnet in our laboratory). This would allow detecting smaller beads and/or increase the speed of detection.

The realization of a portable device is envisioned by miniaturizing the entire set-up, including the source of the external magnetic field[174]. Furthermore, our approach is compatible with the integration of microfluidic devices for the handling of the beads and easily extendible to arrays of identical CMOS detectors.

Chapter 5 Sub-micrometer FMR

5.1 Introduction

Several non-inductive methods have been proposed in literature to perform experiments with better spin sensitivity. Among these, magnetic resonance force microscopy (MRFM)[141-143], scanning tunnel microscopy (ESR-STM)[144, 145], diamond-vacancy center[144, 146-148] detection methods achieved single spin sensitivity. Despite their excellent sensitivity, these methods might not represent a valid and versatile alternative to more conventional, although less sensitive, inductive approaches, in particular for experiments on samples having volumes from few μL to few pL.

Given the broad range of potential applications, the improvement of conventional inductive techniques is nowadays an active research domain[65-68, 91, 92, 94-97, 149, 150].

Nanoscale magnetic structures are of interest both in terms of fundamental physics and device applications. The enlarged surface-to-volume ratio, confined geometries, roughness and morphology of nanostructures have influence on magnetic properties that were investigated using Brillouin light scattering[151, 152], microstrip[153, 154] or coplanar waveguide ferromagnetic resonance[155, 156] on arrays of stripes and dots.

Measurements on array of samples are not ideal to study individual nanoscale structures, given the averaged signal read-out. Different methods were used to investigate single micro and nanostructures, such as MRFM[157, 158] and spSTM-FMR[159]. These techniques can also detect arrays of nanostructures but not simultaneously, being characterized by a single point read-out.

In this chapter we elucidate the possibility of using a CMOS single chip detector to perform FMR experiments on submicrometer volumes. The high sensitivity of the integrated inductive detector combined with the relatively large active volume would enable to inductively study single ferromagnetic nanostructures as well as their coupling.

5.2 Preliminary experiments

In this section of the chapter we describe ferromagnetic resonance (FMR) experiments at the μm scale on YIG microparticles (Iron Yttrium oxide 99.9% REO, Alfa Aesar) and permalloy nanotubes. These measurements confirm the detection capability of the CMOS single chip integrated detector at the micrometer scale.

5.2.1 FMR measurements of YIG microparticles

YIG particles are purchased in a powder form with unknown size distribution. 1 g of YIG particles powder is suspended in 5 mL of pure water. After mixing, the solution is left idle for 30 min to promote the sedimentation of bigger particles at the bottom of the beaker.

1 μL of YIG particle solution is transferred from the surface of the beaker to a 5-μm-thick Mylar foil. Once the water is evaporated, a microparticle of the desired dimension is manually moved to an empty area of the Mylar foil using a toothpick. The same procedure used to transfer the magnetic beads and described in the previous chapter, is applied here for the positioning of the YIG particles. The Mylar foil is flipped to have the surface containing the YIG particles in proximity of the surface of the chip. The isolated particle is aligned with the detector under an optical microscope and transferred onto the chip by pressing the Mylar foil with a swab. A micromanipulator is used to position the sample on top of the integrated detector and eventually move excess particles from the sensitive area.

Figure 5.1 shows FMR spectra of an agglomerate of YIG microparticles measured on the metal (Fig. 5.1a) and in the center of the detector coil (Fig. 5.1b). Due to the procedure used to isolate the sample under investigation, we cannot exclude the undesidered FMR spectral contribution from nanoparticles present in the sensitive area of the detector but not visible under the optical microscope.

In the first configuration, where the YIG agglomerate is placed on the metal, B_0 lies along the z axis and B_1 along the y axis. While in the second configuration, where the YIG agglomerate is placed in the center of the coil, B_0 lies along the z axis and B_1 along the x axis. As shown in the insets in figure 5.1a and 5.1b, during the reallocation of the sample from the metal to the center of the detector, we induce a rotation to the YIG agglomerate. Consequently, in the two configurations the sample has a different orientation with respect to the direction of B_0. The ferromagnetic resonant field strongly depends on the shape and the orientation of the specimen with respect to the direction of the applied static magnetic field B_0. This explains the diversity of the spectra in figure 5.1a and 5.1b. Moreover, as shown in figure 4.2, the sensitivity of the detector increases in proximity of the metal with the consequent increase of the FMR signal amplitude.

In this case, the estimation of the spin sensitivity is not possible due to the unknown precise value of the sample volume and the complexity of the FMR spectrum.

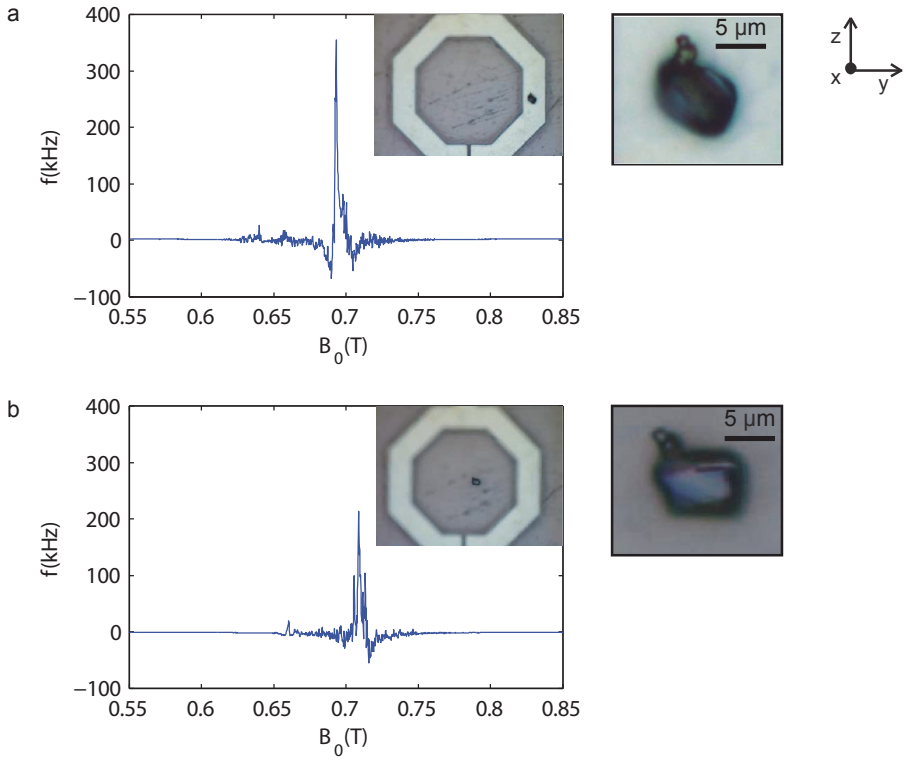

Figure 5.1: FMR measurements of YIG microparticles, performed at 21 GHz. YIG microparticle agglomerate is placed in the desired location with the help of a micromanipulator. (a) YIG agglomerate placed on the metal of the coil. (b) YIG agglomerate placed in the center of the coil. The number of sweeps is equal to 25. Experimental condition notation: υ_m is the frequency of the modulation of the magnetic field, B_m is the amplitude of the modulation of the magnetic field, B_1 is the microwave magnetic field. υ_m = 98.53 kHz, B_m = 0.3 mT, B_1 = 0.06 mT.

5.2.2 FMR measurements of permalloy nanotubes

In this section we report FMR experiments on a 15-µm-long single permalloy ($Ni_{80}Fe_{20}$) nanotube. The non-magnetic core (GaAs) of the nanotube has a diameter of 125 nm and was grown by the group of Prof. A. Fontcuberta i Morral's group (EPFL). A 28-nm-thick permalloy (Py) layer was deposited by F. Heimbach (TUM), to form the ferromagnetic nanotube. The positioning of the nanotube, in the center of the integrated coil, was done by Prof. M. Poggio's group (UNIBAS). Figure 5.2a shows the SEM picture of the cross section of the Py nanotube, taken by Prof. D. Grundler's group (EPFL). Figure 5.2b shows an optical picture of the nanotube positioned on the detector coil.

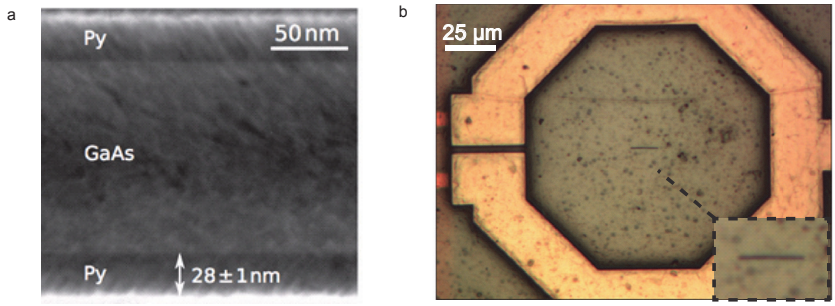

Figure 5.2: Pictures of the permalloy nanotube. (a) SEM picture of the cross section of a permalloy (Py) nanotube. 28 nm of Py are deposited onto a non-magnetic GaAs nanotube of diameter of 125 nm. The SEM picture is taken by Prof. D. Grundler's group (EPFL). (b) Optical picture of a nanotube placed at the center of the integrated detector coil. The positioning of the nanotube was done by Prof. M. Poggio's group (UNI-BAS).

FMR measurements of the Py nanotube are performed, at different angles Θ, defined as the angle between the directions of the static magnetic field B_0 (z axis) and of the axis along the nanotube. The volume of the ferromagnetic sample is equal to 0.07 μm^3 (0.07 fL). Figure 5.3 shows the FMR measurements of the Py nanotube for $\Theta = 0°$ (Fig. 5.3a), $\Theta = 20°$ (Fig. 5.3b) and $\Theta = 45°$ (Fig. 5.3c). As predicted by the theory[160], due to the shape anisotropy, the resonance field B_r of the major resonance signal increases with the increase of the angle Θ. Beside this main resonance peak, additional resonances with much smaller intensities are present. Due to the sensitivity limit, it is not possible to study the angular dependence of these resonance signals.

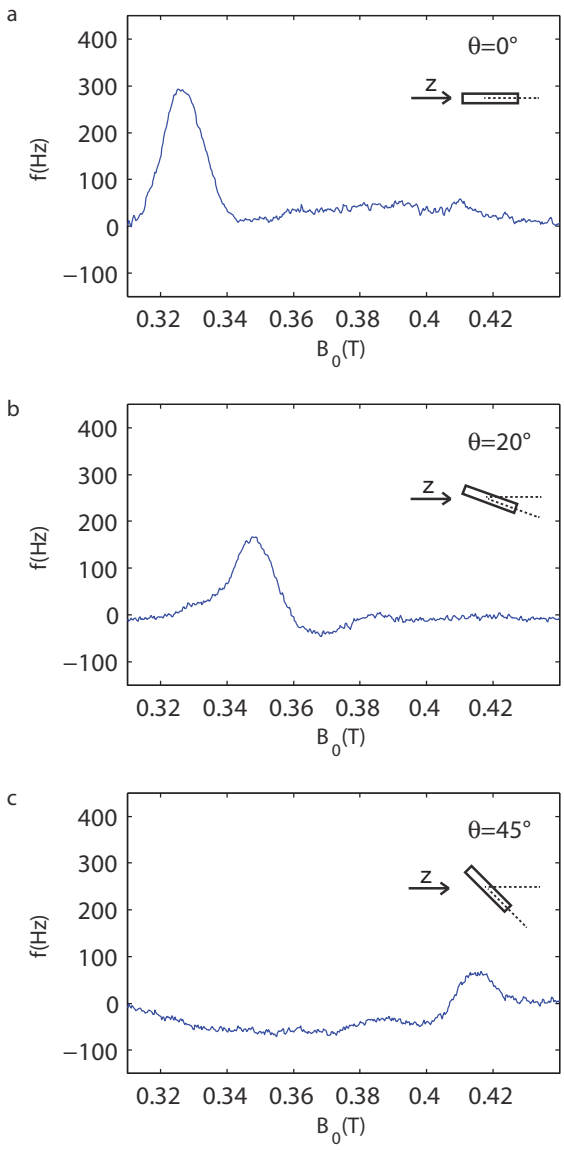

Figure 5.3: FMR measurements of a single permalloid nanotube, performed at 21 GHz. The Py nanotube is placed in the center of the detection coil. The angular dependence of the main resonance signal is studied. ϴ is the angle between the direction of B_0 and the long length of the nanotube. The number of sweeps is equal to 200. Experimental condition notation: υ_m is the frequency of the magnetic field modulation, B_m is the amplitude of the modulation magnetic field, B_1 is the microwave magnetic field. υ_m = 98 kHz, B_m = 0.6 mT, B_1 = 0.06 mT. (a) ϴ = 0°. (b) ϴ = 20°. (c) ϴ = 45°.

5.3 FMR spectroscopy of single permalloy micro/nanodots

Permalloy has been widely used for the investigation of magnetization dynamics on the nanoscale for understanding the basic physics of magnetic phenomena, as well as for the potential applications of the magnetic nanostructures for information transport, processing and storage[161-164].

In this section, we describe the fabrication of permalloy micro and nanodots and the FMR measurements of these nanopatterned structures. The NiFe dots have a height of 30 nm and diameters from 3 μm down to 30 nm, which correspond to a volume of 0.2 μm^3 down to $2 \cdot 10^{-5}$ μm^3.

5.3.1 Fabrication of permalloy micro/nanodots

The permalloy nanodots are fabricated using a single-side polished 4 inch <100> silicon (Si) wafer with 525 μm thickness as a substrate. Photolithography masks are printed on a chromium plate by a direct writer system (VPG 200, Heidelberg Instruments).

The fabrication process, developed to nanopattern the 30-nm-thick NiFe film, is described in figure 5.4. The proposed method is based on e-beam lithography and lift-off for the patterning of the micro and nanodots, photolithography and etching for the patterning of 200 μm x 200 μm Si dies and labels to identify the dimensions of the dots placed in the center of each Si die.

The Si wafer is treated with oxygen plasma and dehydrated for 5 minutes at 180 °C to improve the adhesion of the resist. A double layer of resist is spin coated and patterned to improve the quality of the subsequent lift-off step. A 120-nm-thick MMA EL6 (MicroChem) is spin coated and baked for 5 min at 180 °C. A 60-nm-thick PMMA 495K A2 (MicroChem) is spin coated and baked for 5 min at 180 °C.

E-beam exposure (EBPG5000, Vistec) of the PMMA/MMA double layer, to pattern micro and nanodots and alignment marks for the following photolithography step, is performed with a beam energy of 100 keV and an exposure dose of 1400 $\mu C/cm^2$. The resist development is done in MiBK (MicroChem):IPA 1:3 for 1 min (Fig. 5.4a).

A Ta/NiFe/Ta multilayer with thickness respectively of 5 nm/30 nm/5 nm is e-beam evaporated (LAB 600H, Leybold). The tantalum is used as an adhesive and protective layer for the permalloy film ($Ni_{80}Fe_{20}$). The substrate is then immersed in a heated bath (65 °C) of Remover 1165 (MicroChem) for 2 h for lift-off (Fig. 5.4b).

A 2-µm-thick AZ 9260 layer is spin coated and exposed on a Suss MJB4 manual aligner to define identification labels and a trench in a way that the dot is centered on the die. 60-µm-deep trenches are etched (Alcatel AMS, Bosch process for 12 min) into the silicon (Fig. 5.4c) and a grinding step from the backside of the substrate (Fig. 5.4d) is performed to release individual 200 µm x 200 µm Si dies with a remaining thickness of 55 µm (Fig. 5.4e). Due to the reduced thickness of the Si die, the FMR measurement could be performed placing the backside of the die in contact with the chip surface. This would ease the alignment procedure but worsen the FMR signal, being the ferromagnetic sample placed in a less sensitive region of the integrated detector.

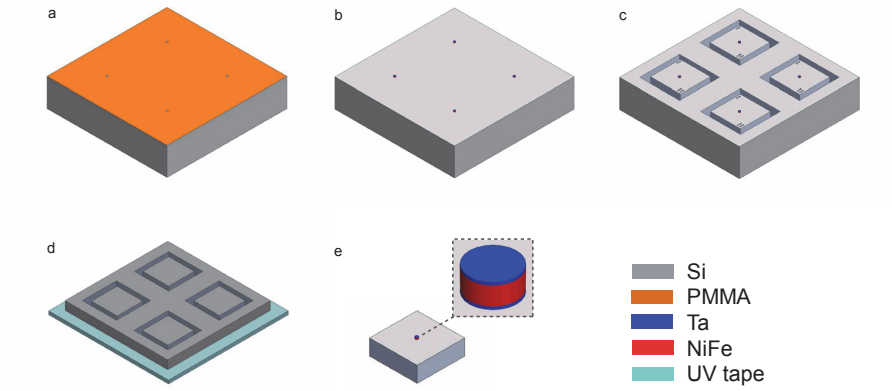

Figure 5.4: Process flow for the fabrication of the NiFe micro and nanodots. A single-side polished 4 inch <100> silicon (Si) wafer with 525 µm thickness is used as substrate. (a) A 120-nm/60-nm-thick MMA/PMMA double layer is e-beam exposed to pattern the dots and marks for the alignment during the following photolithography step. (b) A 5-nm/30-nm/5-nm-thick Ta/NiFe/Ta is e-beam evaporated and the structures defined by lift-off. (c) Trenches and identification labels are patterned by lithography and etching. (d) A grinding from the backside of the substrate is performed. (f) Released individual 200 µm x 200 µm Si die with a remaining thickness of 55 µm and a single dot in its center.

Figure 5.5 shows SEM pictures of the patterned NiFe micro and nanodots having a thickness of 30 nm and a diameter of 3 µm (Fig. 5.5a), 1 µm (Fig. 5.5b), 300 nm (Fig. 5.5c), 100 nm (Fig. 5.5d) 30 nm (Fig. 5.5e).

Figure 5.6 shows an optical picture of released 200 µm x 200 µm Si dies with a thickness of 55 µm, a single NiFe dot in the center of each die and etched identifying labels.

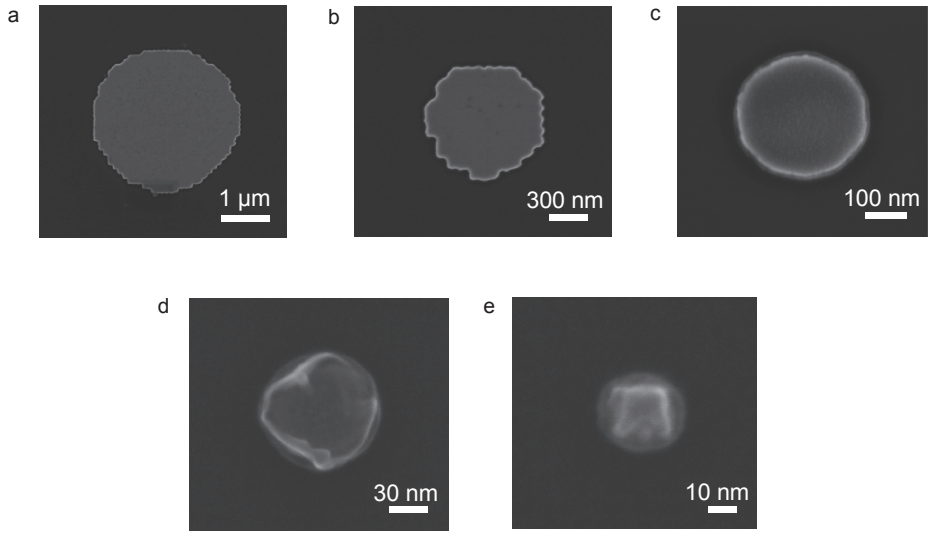

Figure 5.5: SEM pictures of nanopatterned permalloid dots, having different values of diameter (D). (a) D = 3 µm. (b) D = 1 µm. (c) D = 300 nm. (d) D = 100 nm. (e) D = 30 nm.

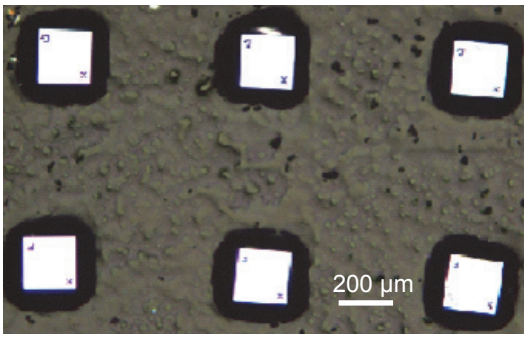

Figure 5.6: Optical microscope picture of the 200 µm x 200 µm Si dies with single permalloid nanodots in the center, attached on a UV tape. Idendifying labels are etched in the Si die.

5.3.2 Measurements of single permalloid micro/nanodots

The Si die, with the permalloy dot of the selected size in its center, is detached from the UV tape. The face of the die, containing the dot, is brought into contact with the surface of the chip and aligned with the integrated detection coil under a microscope, as shown in figure 5.7. A small drop of diluted paper glue (Pritt) is poured onto the chip to keep the die in the desired position.

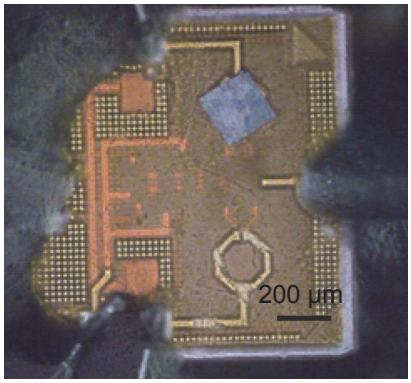

Figure 5.7: Optical microscope picture of a Si die, containing a single permalloid nanodot in its center, placed on top of integrated detector coil.

Figure 5.8 shows the FMR measurements of single 30-nm-thick permalloy dots, performed at 21 GHz. Figure 5.8a and 5.8b show the FMR spectra of a 30-nm-thick permalloy dot with diameter of 1 µm placed in the center of the coil (Fig. 5.8a) and onto the metal of the coil (Fig. 5.8b). The volume of the sample is equal to 0.0235 μm^3 (0.0235 fL).

Figure 5.8c and 5.8d show the FMR spectra of a 30-nm-thick permalloy dot with diameter of 3 µm, with a volume of 0.212 μm^3 (0.212 fL), placed in the center of the coil (Fig. 5.8c) and onto the metal of the coil (Fig. 5.8d).

Given the dimensions of the dots, we can approximate their geometry to a thin film. For this geometry the ferromagnetic resonant field B_r depends on the orientation of the specimen with respect to the direction of the applied static field B_0. For the two configurations used for the measurements (*i.e.* sample placed in the center of the detector coil and sample placed onto the metal of the coil) B_0 is applied parallel to the plane of the dot.

From the Kittel equation[165], it is possible to derive the value of B_r for B_0 applied parallel to the plane of the dot.

$$B_r = \frac{-B_S + \sqrt{{B_S}^2 + 4\left(\frac{f}{\gamma}\right)^2}}{2} \qquad (5.1)$$

where B_s is the saturation field, f the working frequency of the LC oscillator (21 GHz) and γ the electron gyromagnetic ratio (28 GHz/T).

The experimental value of the ferromagnetic resonance field B_r is equal to 0.37 T. Knowing B_r, it is possible to derive the actual value of saturation field B_s of the permalloy thin film, which is equal to 1.1 T.

The signal contribution is proportional to the volume of the sample. Consequently, for the permalloy dot with a diameter of 3 μm we expect an amplitude of the resonance signal 9 times larger than the amplitude obtained in the case of a dot with a diameter of 1 μm. This expectation is confirmed by the experiments reported in Fig. 5.8a and 5.8c.

In the first configuration, where the dot is placed in the center of the coil, the induction field B_1 lies perperdicular to the plane of the dot and to the direction of B_0. In the second configuration, where the dot is placed onto the metal of the coil, B_1 lies in the direction of the plane of the dot and perperdicular to the direction of B_0. Considering the anisotropic shape of the dots, the two configurations correspond to different excitation conditions. Micromagnetic simulations would be needed to study the magnetization dynamics and analize the different FMR spectra expected in the two configurations.

As shown in figure 4.2, we have an increase of signal contribution on the metal of the coil, with consequent increase of the amplitude of the resonance signal, which strongly depends on the positioning of the sample.

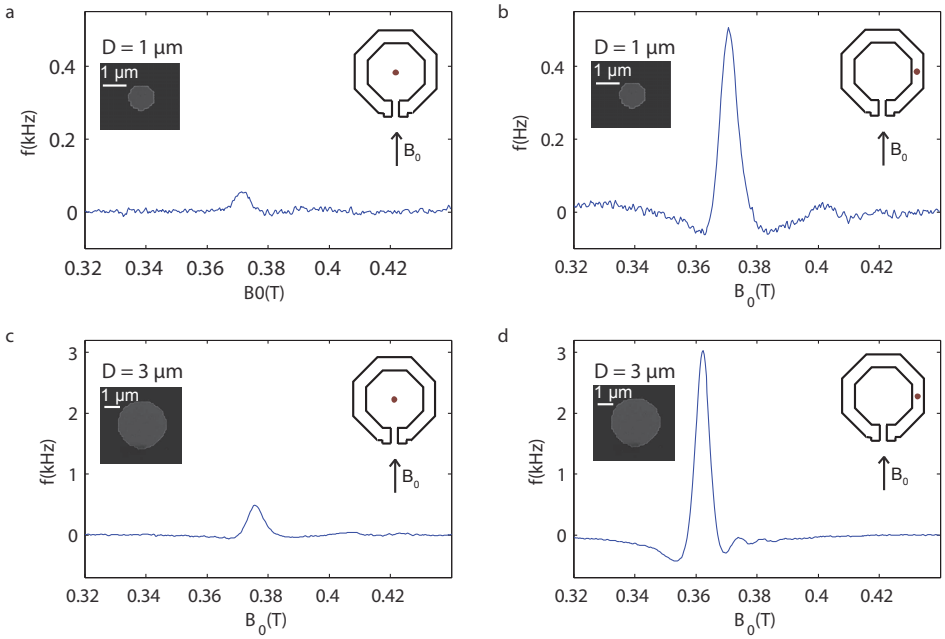

Figure 5.8: FMR measurements of single permalloid nanodots, performed at 21 GHz. The number of sweeps is equal to 20. Experimental condition notation: D is the diameter of the dot, pos is the position of the dot, υ_m is the frequency of the magnetic field modulation, B_m is the amplitude of the modulation magnetic field, B_1 is the microwave magnetic field. (a) D = 1 μm, pos = center, υ_m = 98.52 kHz, B_m = 1.2 mT, B_1 = 0.06 mT. (b) D = 1 μm, pos = metal, υ_m = 98.52 kHz, B_m = 1.6 mT, B_1 = 0.06 mT. (c) D = 3 μm, pos = center, υ_m = 98.52 kHz, B_m = 1.6 mT, B_1 = 0.06 mT. (d) D = 3 μm, pos = metal, υ_m = 98.52 kHz, B_m = 1.2 mT, B_1 = 0.06 mT.

5.3.3 Sensitivity calculation

The spin sensitivity N_{min} (see definition in section 3.3.3) is determined experimentally from the SNR of the FMR spectrum acquired from a single 30-nm-thick NiFe dot having a diameter of 1 μm and placed onto the metal of the coil. The SNR, shown in Fig. 5.8b, is equal to 38 per single scan. Considering a detection bandwidth ΔF of 2.5 Hz, an active volume V_s of 0.0235 μm^3 (0.0235 fL) and a spin density of $1.82 \cdot 10^{11}$ spins/μm^3, the resulting spin sensitivity N_{min} is about $7 \cdot 10^7$ spins/$\sqrt{\text{Hz}}$.

The spin sensitivity $N_{min\Delta B}$ as a function of the linewidth ΔB (see definition in section 3.3.3), determined from the FMR spectrum of the 30-nm-thick NiFe dot with a diameter of 1 μm, placed onto the metal of the coil, is equal to $7.3 \cdot 10^5 \frac{\text{spins}}{\sqrt{\text{Hz}}\, G}$.

For a 30-nm-thick NiFe dot with a diameter of 500 nm, the active volume V_s is equal to 0.0058 μm^3 (0.0058 fL). Under the same experimental conditions used to measure the 1 μm diameter dot, the expected SNR per single scan would be 9. Despite the theoretical estimations, we could not detect an FMR spectrum for dots having a diameter smaller than 1 μm. Further experiments would be needed to clarify this unexpected result.

5.4 FMR spectroscopy of single YIG nanodots

Yttrium iron garnet ($Y_3Fe_5O_{12}$), commonly referred as YIG, is the material of choice for magnonics[166]. This discipline aims at using spin waves to carry and process information. Moreover YIG gained considerable interest for its sharp ferromagnetic resonance (FMR) and its application in microwave devices. In fact, it is widely used in microwave and optical-communication devices such as filters, tunable oscillators, or non-reciprocal devices.

In this section we report the fabrication of YIG micro and nanodots, as well as the FMR measurements of the resulting nanopatterned structures. The YIG dots have a thickness of 30 nm and diameters ranging from 3 μm down to 300 nm, which respectively correspond to a volume of 0.2 μm^3 (0.2 fL) down to 0.0021 μm^3 (2.1 aL).

5.4.1 Fabrication of YIG nanodots

A 30-nm-thick YIG film was deposited by Dr. Hoffmann's (Argonne National Laboratory) group on a 500-μm-thick (111)-oriented gadolinium gallium garnet ($Gd_3Ga_5O_{12}$, GGG) single crystal substrate at room temperature from a commercial YIG sputter target. Details of the deposition process can be found in Ref. 167. High-quality YIG thin films can be only grown on lattice-matched GGG substrates. The growth of YIG films on other substrates results in an alteration of the magnetic properties[168-171].

The fabrication process developed to nanostructure the YIG film is described in figure 5.9. The proposed method is based on e-beam lithography for the patterning of the micro and nanodots and a combination of photolithography steps for the fabrication of marks used to identify the position and the size of the YIG dots.

Given the limited availability and the high value of the YIG/GGG substrates, the entire process is performed on a small die (5 mm x 2.5 mm). The major challenge of this fabrication process is related to the need of using only die-level compatible processes and reversible testing steps.

The process starts with the microfabrication of metal marks used to define the position of the YIG dots during e-beam lithography. The YIG/GGG substrate is treated with oxygen plasma to improve the adhesion of the resist. A double layer of resist is employed to improve the quality of the following lift-off step. An AZ1512/LOR-5A (MicroChem) double layer is spin coated to obtain a thickness of 1.1 μm/0.48 μm and photopatterned with a direct writing system (MLA 150, Heidelberg Instruments) and an exposure dose of 98 mJ/cm^2, followed by a development and a drying step (Fig. 5.9a).

A 5-nm-thick Ti adhesion layer followed by a 40-nm-thick Au layer are evaporated (LAB 600H, Leybold). The substrate is then immersed in a heated bath (65 °C) of Remover 1165 (MicroChem) for 2 h for photoresist lift-off (Fig. 5.9b).

To improve the adhesion of the e-beam resist HSQ XR1541 006 (Dow Corning), the substrate is immersed for 1 min in MF CD26 (MicroChem). Rinsing, drying, dehydration and cooling steps are then performed. A 190-nm-thick HSQ layer is spin coated. Due to the non-conductivity of the substrate, a 10-nm-thick Al layer is evaporated (LAB 600H, Leybold) on top of the HSQ resist as shown in figure 5.9c. The 10-nm-thick Al layer is thick enough to provide a conductive surface, essential to avoid charging effects in e-beam lithography, and thin enough to maintain the optical transparency, needed for the detection of Au marks during the alignment procedure.

E-beam exposure (EBPG5000, Vistec) of the HSQ resist layer is performed with e-beam energy of 100 keV and an exposure dose of 500 μC/cm^2. This value is the result of a dose test for parameters optimization. The resist development is done in TMAH; in the same step the Al layer is etched away, being the TMAH also an Al etchant (Fig. 5.9d).

YIG dots are defined (Fig. 5.9e) by ion milling (Nexus IBE-530, Veeco) with an Ar plasma of 500 V and a current of 800 mA/cm^2 for 134 s. The substrate fixture is kept at low temperature (lower than 90 °C) with a rotating speed of 10 rpm and a tilt angle of 10°.

Due to the limited number of the YIG/GGG substrates, it was not possible to perform an etching test on the YIG film to derive the etching rate of YIG at these experimental conditions. It is essential, though, that the 30-nm-thick YIG film is completely etched and that at the end of the etching process the HSQ resist mask is still present to prevent the removal of the YIG dots. An overetching is not an issue, provided that the HSQ resist mask is not removed completely. For these reasons, an etching test on HSQ was performed and the value of the etching rate was derived (70nm/min). With an etching time of 134 s we have a HSQ residual layer of about 30 nm. This layer does not influence the magnetic properties of the YIG dots, it is then not removed to avoid further processing. HSQ masks the gold marks during the etching step.

At this point, circular marks with a diameter of 10 µm are fabricated to help localizing the YIG dots for inspection. To improve the adhesion of the resist, the substate is treated with oxygen plasma. A 3-µm-thick layer of AZ 9221 (MicroChem) is spin coated and exposed with a direct writer system (MLA 150, Heidelberg Instruments) and an exposure dose of 133 mJ/cm^2.

The marks are defined by ion milling (Nexus IBE-530, Veeco) by Ar plasma for 30 min with the same parameters used for the etching of the YIG film (Fig. 5.9f). The residual AZ resist is removed with acetone.

Using the same procedure and an Ar ion milling (Nexus IBE-530, Veeco) for 60 min, backside alignment marks are patterned to define dicing marks and labels used to identify the YIG dots and to align the dots with the integrated detection coil (Fig. 5.9g).

Lastly, the substrate is diced, using an automatic dicing saw (Disco DAD321), to 200-µm-wide and 4-mm-long rods containing YIG micro and nanodots spaced enough to have only a single dot in the sensitive area of the CMOS single chip detector (Fig. 5.9k).

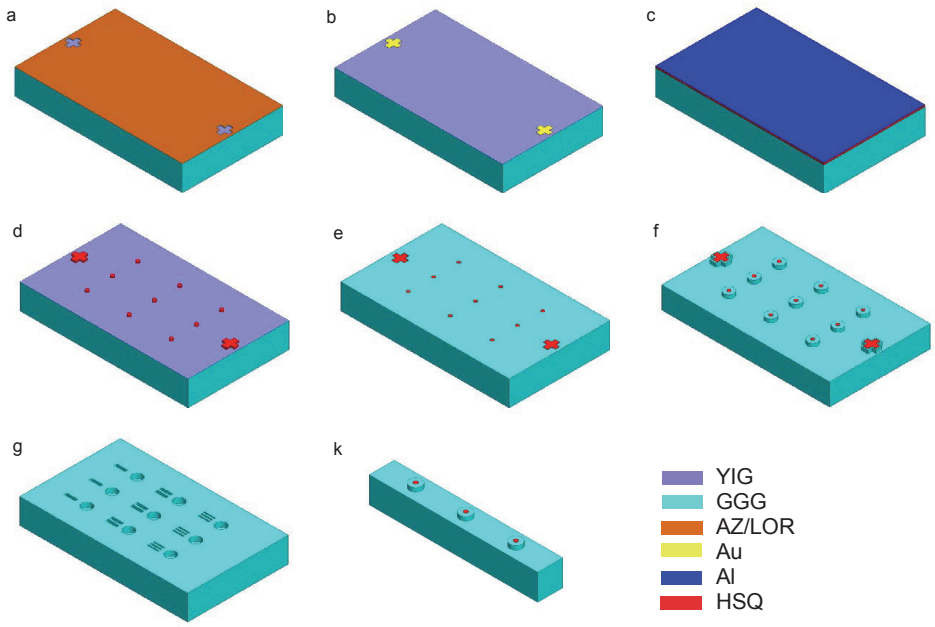

Figure 5.9: Process flow for the fabrication of the YIG micro and nanodots: a 5 mm x 2.5 mm substrate of 30 nm/500 µm (111) YIG/GGG is used as substrate. (a) A 1.1/0.48-µm-thick AZ/LOR double layer is patterned to structure marks for alignment during e-beam lithography. (b) A 40/5-nm-thick Au/Ti double layer is evaporated and Au marks are patterned by lift-off. (c) A 10 nm-thick Al layer is evaporated on top of a 190-nm-thick HSQ resist layer for conductivity improvement. (d) Micro and nanodots are defined by e-beam lithography. (e) The 30-nm-thick YIG film is etched by Ar ion milling; HSQ resist masks the Au marks during the ething step. (f) Circular marks are patterned by photolithography and Ar ion milling to localize the dots during inspection. (g) On the backside of the substrate, dicing marks are defined by photolithography and Ar ion milling. In the same step marks, needed for the alignment procedure with the detector, are patterned.

Figure 5.10 shows AFM pictures of the patterned YIG dots having a thickness of 30 nm and a diameter of 3 μm (Fig. 5.10a) and 1μm (Fig. 5.10b).

Figure 5.11 shows the frontside (a) and backside (b) optical microscope pictures of a section of the 0.2 mm x 4 mm GGG rod. In the frontside of the rod (Fig. 5.11a), in correspondence of the YIG nanodot, a circular mark with diameter of 10 μm is patterned to localize the dot during inspection (indicated by the arrow). In the backside of the rod (Fig. 5.11b), labels and marks are patterned to identify the dimension of the dot and to permit the alignment with the sensitive area of the detector. The rough layer visible in the picture is the photoresist used as a mask and not removed after the etching step.

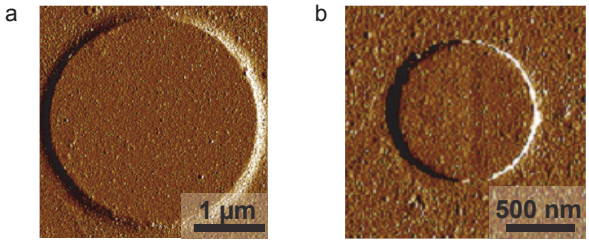

Figure 5.10: AFM pictures of nanopatterned YIG dots, having a thickness of 30 nm and diameter of 3 μm (a) and 1 μm (b).

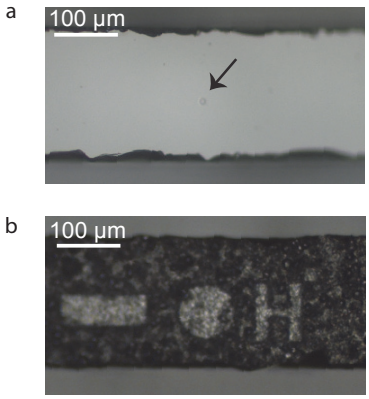

Figure 5.11: Optical microscope pictures of a section of the GGG rod. (a) Picture of the frontside of the rod. The arrow indicates the circular mark patterned to localize the dot during inspection. (b) Picture of the backside of the rod showing the identifying labels and the alignment marks.

5.4.2 Measurements of single YIG micro/nanodots

A 200-µm-wide and 4-mm-long GGG rod contains YIG dots, spaced enough to have a single dot in the sensitive area of the detector. The rod is flipped upside down, to have the surface containing the dots in direct contact with the surface of the CMOS single chip detector. A dot of the desired size is aligned with the integrated detector coil under a microscope, using backside identifying labels and alignment marks, as shown in figure 5.12. A small drop of diluted glue (Pritt) is poured onto the chip to keep the rod in the desired position.

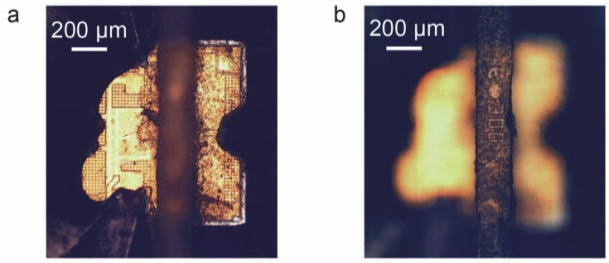

Figure 5.10: GGG rod positioned onto the chip. Optical microscope picture focused (a) on the surface of the chip and (b) on the backside surface of the GGG rod, containing identifying labels and positioning marks.

Figure 5.13 shows the FMR measurements of a single 30-nm-thick YIG dot having a diameter of 1 µm, placed in the center (Fig. 5.13a) and on the metal of the coil (Fig. 5.13b). The volume of the sample is equal to 0.0235 μm^3 (0.0235 fL). The experimental parameters are listed in the figure caption. As explained in detail in section 5.3.2, considering the dot as a thin film, the ferromagnetic resonance field B_r depends on the direction of the applied static magnetic field B_0. B_0 lies in the direction of the plane of the YIG thin film for both of the configurations used in the experiments (*i.e.*, dot in the center and dot on the metal of the coil).

The measured value of the B_r is equal to 0.65 T. Knowing the value of the B_r, from the Kittel equation[165] it is possible to calculate the value of the saturation field B_s for the 30-nm-thick YIG thin film, which is equal to 0.2 T.

As discussed in section 5.3.2, given the anisotropy of the sample, the two configurations (*i.e.*, dot placed in the center and onto the metal of the coil) correspond to different excitation conditions. Therefore, the magnetization dynamics and the FMR spectra are different (as shown in Fig 5.13).

Moreover, a better sensitivity is obtained on the metal of the coil (see section 4.2), which implies an increase of the resonance signal, dependent on the positioning of the sample onto the metal. Micromagnetic simulations would be required to analize in details the obtained FMR spectra.

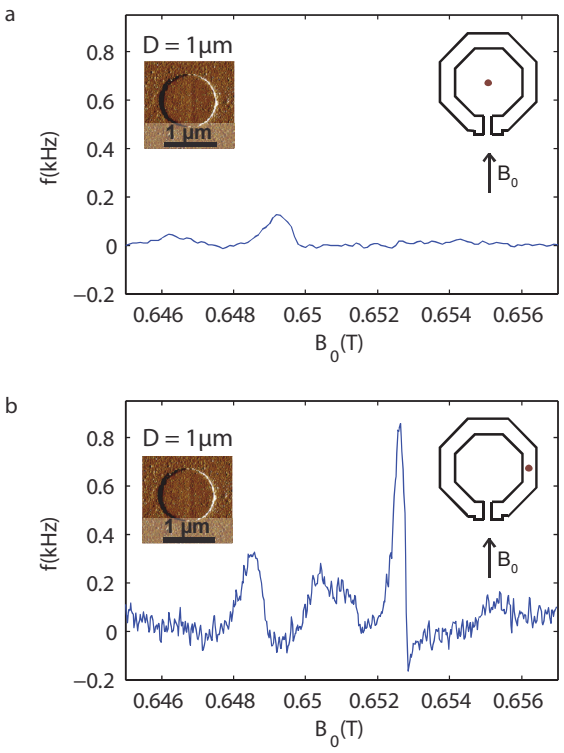

Figure 5.11: FMR measurements of a single YIG dot, having a diameter of 1 µm, are performed at 21 GHz. Experimental condition notation: avg is the number of sweeps, pos is the position of the dot, υ_m is the frequency of the magnetic field modulation, B_m is the amplitude of the modulation magnetic field, B_1 is the microwave magnetic field. (a) avg = 20, pos = center, υ_m = 98.52 kHz, B_m = 0.48 mT, B_1 = 0.06 mT. (b) avg = 1, pos = metal, υ_m = 98.52 kHz, B_m = 0.5 mT, B_1 = 0.06 mT.

5.4.3 Sensitivity calculation

The spin sensitivity N_{min} (see definition section 3.3.3) is determined starting from the SNR of the FMR spectrum acquired from a single 30-nm-thick YIG dot having diameter of 1 µm and placed onto the metal of the coil. The SNR, shown in Fig. 5.13b, is equal to 20 per single scan. Considering a detection bandwidth ΔF of 2.5 Hz, an active volume V_s of 0.0235 µm^3 (0.0235 fL) and a spin densitiy of $4.27 \cdot 10^9$ spins/µm^3, the spin sensitivity N_{min} is about $3.1 \cdot 10^6$ spins/$\sqrt{\text{Hz}}$.

The spin sensitivity $N_{min\Delta B}$ as a function of the linewidth ΔB (see definition in section 3.3.3), determined from the FMR spectrum of the 30-nm-thick YIG dot with diameter of 1 µm is equal to $9.3 \cdot 10^5 \frac{\text{spins}}{\sqrt{\text{Hz}}\, G}$.

For a 30-nm-thick YIG dot with diameter of 300 nm, the active volume V_s is equal to 0.0021 µm^3 (0.021 fL). Under the same experimental conditions used to measure the 1 µm diameter dot, we would expect a SNR of 1.8 per single scan and a SNR of 18 after 100 averages. Even in this case we didn't detect an FMR spectrum for dots having a diameter smaller than 1 µm. The identification of the causes would require further studies.

5.5 Conclusion

In this chapter we demonstrated the capability of the CMOS single chip detector to perform ferromagnetic resonance measurements on samples (*i.e.* nanopatterned permalloy and YIG dots) with volumes down to 0.0235 fL. The system enables to inductively study single ferromagnetic nanostructures as well as the coupling between them, in an active area of about $5 \cdot 10^4$ μm^2. This is an achievement compared to previously reported methods[157-160], which are either limited by sensitivity or by detection speed.

Chapter 6 Conclusion

6.1 Summary

During the PhD work we developed methods and fabrication techniques to address sub-nL scale nuclear magnetic resonance (NMR), electron paramagnetic resonance (EPR) and ferromagnetic resonance (FMR) spectroscopy. We realized and integrated microfluidic systems with single chip CMOS detectors to perform NMR investigations of subnanoliter liquids and biological entities immersed in liquids, as well as EPR measurements of liquids and frozen solutions. Finally, FMR studies on nanopatterned permalloy ($Ni_{80}Fe_{20}$) and YIG ($Y_3Fe_5O_{12}$) dots demonstrated the μm and sub-μm scale detection capabilities of the CMOS integrated detector.

6.2 Conclusion

Magnetic resonance experiments on subnanoliter volumes are mainly hindered by the limited sensitivity of the detector and the difficulties in controlling and holding such small volumes in proximity of the excitation/detection microcoils.

In this work, we showed nuclear magnetic resonance (NMR) experiments on liquids and biological entities (i.e. tardigrade *Richtersius coronifer* ova and *C. elegans* subsection) immersed in liquid with active volumes down to 100 pL. It opens up the possibility of assessing a multitude of biological entities present at the subnanoliter scale such as single cells, embryos and small living microorganisms[64]. This was achieved by employing combinations of microfluidic systems with miniaturized CMOS integrated single-chip NMR detectors.

We developed two methods for the fabrication of the microfluidics, one based on conventional microfabrication technique and the other based on two-photon polymerization, a 3D printing technique with lateral resolution of 300 nm. Both the techniques permit the realization of microchannels that confine samples at distances smaller than 10 μm from the detector. This particular feature allows for an only slightly inferior detected signal (30%) than the one achieved in the optimal condition of the sample in direct contact with the integrated detection microcoil.

The new SU-8 based microfabrication process is suitable for the large scale production and for the realization of microfluidic systems where the 3D design and the resolution limit are not an issue. The 3D-printing-based microfabrication process enables the rapid realization of microfluidic systems for the trapping and culturing of biological entities of different sizes, geometries and

fluidic beaviours. The non-invasive handling of the samples and an efficient trapping of the living entities during the NMR investigation was shown. We demonstrated that this technique is an exceptional solution for NMR applications. In fact, due to its flexibility in terms of design of the microfluidic structure, it is possible to minimize the magnetic field non-uniformities and the dead volume, crucial for NMR experiments on volume-limited subnanoliter liquid samples. We developed a robust fluidic interface, which ensures perfect sealing over several days and tolerates flows as strong as 7 μL/s.

Using the 3D printed microfluidic systems interfaced with the single chip CMOS NMR detector, we showed a spectral resolution down to 0.007 ppm FWHM on liquid samples with volume of 100 pL. Better spectral resolutions (down to 0.6 Hz) have been reported in literature,[69, 76, 118, 119] but with probes having lower spin sensitivities.

A spectral resolution of 0.1 ppm and 0.12 ppm is obtained respectively for the *Rc* ovum and the *C. elegans* subsection. Microscopic components inside the samples may cause magnetic field non-uniformities, which limit the achievable spectral resolution as reported in Ref. 6. Neverthless, with a sensitivity of $2.5 \cdot 10^{13}$ spins/$\sqrt{\text{Hz}}$ we are able to detect highly concentrated endogenous compounds that are present in the biological entities, with an active volume down to 100 pL and measurement times as short as 3 hours.

We reported EPR experiments on subnanoliter active volumes by a single chip CMOS detector, interfaced with a glass capillary. A wide choice of capillaries, having different sizes, geometries and materials, are commercially available. They provide a good alternative for magnetic resonance investigations on liquids at the sub-nL scale, for applications that do not require customized channel geometry. The capability of the system to perform measurements at cryogenic temperature was demonstrated by experiments on frozen solutions. This can be an enabling step for the study of various biological samples, whose paramagnetic ions have such high relaxation rates that they cause the broadening of the EPR spectra beyond detectability at room temperature[128].

Furthermore, the same CMOS detector was used for the detection of FMR at the μm and sub-μm scale. We proposed a new method for the sensing of magnetic beads, based on detection of the change in susceptibility in FMR conditions. Due to the frequency and field dependence of the susceptibility[139], the detected variation is about 20 times greater than the change in magnetization in static conditions sensed by other approaches[133, 140]. The system allows for the detection of a single bead, as well as *n* beads containable in an active area of about 5×10^4 μm^2. This is an alternative approach compared to previously reported magnetic bead detection schemes[133-138], which suffer either from limited sensitivity or from reduced sensing area.

Lastly, we demostated the capability of the single chip integrated detector to perfom FMR measurements on nanopatterned permalloy and YIG structures, with volumes down to 0.0235 fL. Compared with previously reported methods[157-160], which are limited either by sensitivity or by detection speed, our solution enables to inductively study single ferromagnetic nanostructures as well as their coupling.

6.3 Outlook

The development of the microfluidic systems enables a non-invasive handling and trapping of the biological entities, providing biocompatible culturing conditions during the experiments. The main limitation of the NMR spectroscopy for the study of subnanoliter samples is given by the long measurement time required. This is mainly due to the small number of spins contained in sub-nL volumes and the poor spectral resolution − 0.12 ppm in the *Rc* ovum and 0.1 ppm in the *C. elegans* subsection. In our current experimental condition, characterized by a field of 7 T, a microcoil with active volume of 0.25 nL, a spectral resolution of about 30 Hz and repetition time equal to 200 ms, a SNR of three is achieved on 500 pmol of ^{1}H nuclei per single scan. This corresponds to a limit of detection (LOD_f) of approximately 25 pmol in 10 min and 8 pmol in 60 min. The use of a field of 23.5 T (the highest field commercially available) would improve the sensitivity by a factor 6[112], with a LOD_f of about 4 pmol in 10 min and 1 pmol in 1 h.

Previous studies of extracellular culture media suggest that the uptake or production rate of metabolites in human oocytes − such as glucose, pyruvate and lactate − change during the developmental stages and can reach 50 pmol/h per single oocyte[126]. NMR investigations on single oocyte could give a contribution in the in-vivo study of metabolic processes and the development of early embryos at the single-entity level, essential for the optimization of in vitro fertilization.

The developed solutions, which combine microfluidic systems with CMOS single chip NMR detectors, are compatible with the implementation of arrays of miniaturized probes. A multichannel microfluidic structure could confine and trap single biological entities onto an array of integrated microcoils, which would enable the simultaneous investigation of heterogeneity among individuals. Their response to different environmental conditions and administation of drugs could be monitored through a fluidic system which permits the realization of different controlled microenviroments on the same platform. Furthermore, it would be possible to simultaneously study highly concentrated metabolites contained in different subsections of the same C. elegans individual.

A microfluidic system could be developed and combined with the single chip CMOS EPR detector to perform studies of single biological entitities. EPR spectroscopy is a tool for the investigation of free radicals that are generated by cells during their regular metabolism. With typical concentrations from nM to pM[130], the detection of free radicals in single cells is an ambitious target, considered the exceedingly small active volume and the concentration sensitivity of 10 μM per single scan. However, this goal could be achieved by working at higher operation frequencies, by further miniaturizing the detector coil and performing the experiments at cryogenic temperatures (down to 4 K) to detect radical species with short spin-spin relaxation times.

Sensing of magnetic beads was performed by detecting the change in susceptibility in FMR condition using the CMOS integrated detector. The main limitation of this approach is given by the maximum amplitude of the magnetic field modulation achievable with our current setup (1.1 mT), which should be equal to the width of the FMR signal (80 mT) for a maximization of the detected signal. The miniaturization of the modulation coils would enable a higher modulation field, thus it would increase the speed of detection and permit the detection of smaller beads. A portable device for the detection of magnetic beads can be envisioned by decreasing the working

frequency of the LC oscillator and by miniaturizing the entire set-up, including the source of the static magnetic field[172]. Furthermore, the integration of a microfluidic structure would provide a tool for the handling of the labelled biological targets. Parallelization of the read-out is also possible by implementing an array of FMR integrated probes.

Finally, CMOS single chip EPR detectors at working frequency up to 146 GHz were recently developed in our group (see Ref. 93) and show sensitivity of $2 \cdot 10^7$ spins/$Hz^{1/2}$. These high sensitive detectors would permit the FMR detection of NiFe and YIG nanodots with volumes down to 2 aL in a single scan.

References

1. Grisi, M.; Gualco, G.; Boero, G. *Rev. Sci. Instrum.* **2015,** 86, (4).

2. Boero, G.; Gualco, G.; Lisowski, R.; Anders, J.; Suter, D.; Brugger, J. *Journal of Magnetic Resonance* **2013,** 231, 133-140.

3. Beckonert, O.; Keun, H. C.; Ebbels, T. M.; Bundy, J.; Holmes, E.; Lindon, J. C.; Nicholson, J. K. *Nature protocols* **2007,** 2, (11), 2692-2703.

4. Thurber, K. R.; Harrell, L. E.; Smith, D. D. *J Magn Reson* **2003,** 162, (2), 336-40.

5. Antzutkin, O. N.; Leapman, R. D.; Balbach, J. J.; Tycko, R. *Biochemistry-Us* **2002,** 41, (51), 15436-50.

6. Lee, S. C.; Cho, J. H.; Mietchen, D.; Kim, Y. S.; Hong, K. S.; Lee, C.; Kang, D. M.; Park, K. D.; Choi, B. S.; Cheong, C. *Biophys J* **2006,** 90, (5), 1797-1803.

7. Lee, S. C.; Mietchen, D.; Cho, J. H.; Kim, Y. S.; Kim, C.; Hong, K. S.; Lee, C.; Kang, D.; Lee, W.; Cheong, C. *Differentiation* **2007,** 75, (1), 84-92.

8. Grant, S. C.; Aiken, N. R.; Plant, H. D.; Gibbs, S.; Mareci, T. H.; Webb, A. G.; Blackband, S. J. *Magnet Reson Med* **2000,** 44, (1), 19-22.

9. Ishikawa, M.; Price, W. S.; Ide, H.; Arata, Y. *Plant physiology* **1997,** 115, (4), 1515-1524.

10. Appel, T. R.; Baumann, M. A. *Oral surgery, oral medicine, oral pathology, oral radiology, and endodontics* **2002,** 94, (2), 256-61.

11. Potter, K.; Landis, W. J.; Spencer, R. G. *J Bone Miner Res* **2001,** 16, (6), 1092-100.

12. Blaise, B. J.; Giacomotto, J.; Elena, B.; Dumas, M.-E.; Toulhoat, P.; Ségalat, L.; Emsley, L. *Proceedings of the National Academy of Sciences* **2007,** 104, (50), 19808-19812.

13. Blaise, B. J.; Giacomotto, J.; Triba, M. N.; Toulhoat, P.; Piotto, M.; Emsley, L.; Ségalat, L.; Dumas, M.-E.; Elena, B. *Journal of proteome research* **2009,** 8, (5), 2542-2550.

14. Rajon, D. A.; Jokisch, D. W.; Patton, P. W.; Shah, A. P.; Bolch, W. E. *Med Phys* **2000,** 27, (11), 2624-35.

15. Castellani, F.; van Rossum, B.; Diehl, A.; Schubert, M.; Rehbein, K.; Oschkinat, H. *Nature* **2002,** 420, (6911), 98-102.

16. Traikia, M.; Warschawski, D. E.; Recouvreur, M.; Cartaud, J.; Devaux, P. F. *European biophysics journal : EBJ* **2000,** 29, (3), 184-95.

17. Takahashi, M.; Wehrli, F. W.; Wehrli, S. L.; Hwang, S. N.; Lundy, M. W.; Hartke, J.; Borah, B. *J Bone Miner Res* **1999,** 14, (5), 680-9.

18. ORFI, L.; LARIVE, C. K.; LEVINE, S. M. *LIPIDS* **1997,** 32, (10), 1035-40.

19. JOSELEAU, J. P.; RUEL, K. *PLANT PHYSIOLOGY* **1997,** 114, (3), 1123-33.

20. SCHIFFENBAUER, Y. S.; TEMPEL, C.; ABRAMOVITCH, R.; MEIR, G.; NEEMAN, M. *CANCER RES* **1995,** 55, (1), 153-8.

21. SCHIEMANN, O.; PRISNER, T. F. *QUARTERLY REVIEWS OF BIOPHYSICS* **2007,** 40, (01), 1-53.

22. MCHAOURAB, H. S.; STEED, P. R.; KAZMIER, K. *STRUCTURE* **2011,** 19, (11), 1549-1561.

23. HENSLEY, K.; CARNEY, J.; MATTSON, M.; AKSENOVA, M.; HARRIS, M.; WU, J.; FLOYD, R.; BUTTERFIELD, D. *PROCEEDINGS OF THE NATIONAL ACADEMY OF SCIENCES* **1994,** 91, (8), 3270-3274.

24. VELAN, S. S.; SPENCER, R. G.; ZWEIER, J. L.; KUPPUSAMY, P. *MAGNET RESON MED* **2000,** 43, (6), 804-809.

25. YANG, D.; MATSUBARA, K.; YAMAKI, M.; EBINA, S.; NAGAYAMA, K. *BIOCHIMICA ET BIOPHYSICA ACTA* **1994,** 1206, (2), 173-9.

26. WEIL, J. A., ELECTRON PARAMAGNETIC RESONANCE. WILEY, ED. 2007.

27. BLACK, R. D.; EARLY, T. A.; ROEMER, P. B.; MUELLER, O. M.; MOGRO-CAMPERO, A.; TURNER, L. G.; JOHNSON, G. A. *SCIENCE* **1993,** 259, (5096), 793-5.

28. LASKER, S. E.; IATROPOULOS, M. J.; HECHT, S. S.; MISRA, B.; AMIN, S.; ZANG, E.; WILLIAMS, G. M. *CANCER LETTERS* **1992,** 67, (2-3), 125-31.

29. CROZIER, S.; FIELD, J.; SHANNON, G. F.; DODDRELL, D. M. *MEDICAL & BIOLOGICAL ENGINEERING & COMPUTING* **1992,** 30, (2), 226-30.

30. PEARLMAN, J. D.; SOUTHERN, J. F.; ACKERMAN, J. L. *ANGIOLOGY* **1991,** 42, (9), 726-33.

31. CHENG, H. M.; AGUAYO, J. B.; MOORE, G. J.; MATTINGLY, M. *MAGN RESON MED* **1991,** 17, (1), 62-8.

32. BEHLING, R. W.; TUBBS, H. K.; COCKMAN, M. D.; JELINSKI, L. W. *BIOPHYS J* **1990,** 58, (1), 267-71.

33. CHI, L. M.; WU, W. G. *BIOPHYS J* **1990,** 57, (6), 1225-32.

34. YAMADA, B.; WESTMORELAND, D. G.; KOBATAKE, S.; KONOSU, O. *PROGRESS IN POLYMER SCIENCE* **1999,** 24, (4), 565-630.

35. WEIL, J. A.; BOLTON, J. R., *ELECTRON PARAMAGNETIC RESONANCE: ELEMENTARY THEORY AND PRACTICAL APPLICATIONS*. JOHN WILEY & SONS: 2007.

36. ABRAGAM, A., *THE PRINCIPLES OF NUCLEAR MAGNETISM*. OXFORD UNIVERSITY PRESS: 1961.

37. Callaghan, P. T., *Principles of Nuclear Magnetic Resonance Microscopy*. Oxford, 1991.

38. Back, P. J.; Coy, A.; Xia, Y.; Callaghan, P. T.; Diamante, L. M.; Umbach, S. L. *International journal of biological macromolecules* **1991,** 13, (3), 181-9.

39. Callaghan, P. T., *Principles of nuclear magnetic resonance microscopy*. Clarendon Press Oxford: 1991; Vol. 3.

40. Ernst, R. R.; Bodenhausen, G.; Wokaun, A. *Principles of nuclear magnetic resonance in one and two dimensions*; 1991.

41. Pykett, I. L. *Sci Am* **1982,** 246, (5), 78-88.

42. Liebetanz, D.; Fauser, S.; Michaelis, T.; Czeh, B.; Watanabe, T.; Paulus, W.; Frahm, J.; Fuchs, E. *J Psychiat Res* **2003,** 37, (4), 277-286.

43. Badilita, V.; Meier, R. C.; Spengler, N.; Wallrabe, U.; Utz, M.; Korvink, J. G. *Soft Matter* **2012,** 8, (41), 10583-10597.

44. G Webb, A. *Progress in Nuclear Magnetic Resonance Spectroscopy* **1997,** 31, (1), 1-42.

45. Tkac, I.; Starcuk, Z.; Choi, I. Y.; Gruetter, R. *Magnet Reson Med* **1999,** 41, (4), 649-656.

46. Brown, J. R.; Callaghan, P. T. *J Magn Reson* **2010,** 204, (1), 21-5.

47. Pfeuffer, J.; Tkac, I.; Provencher, S. W.; Gruetter, R. *Journal of Magnetic Resonance* **1999,** 141, (1), 104-120.

48. Ganji, S. K.; An, Z. X.; Banerjee, A.; Madan, A.; Hulsey, K. M.; Choi, C. H. *Nmr Biomed* **2014,** 27, (10), 1167-1175.

49. Branzoli, F.; Ercan, E.; Webb, A.; Ronen, I. *Nmr Biomed* **2014,** 27, (5), 495-506.

50. Massin, C.; Vincent, F.; Homsy, A.; Ehrmann, K.; Boero, G.; Besse, P.-A.; Daridon, A.; Verpoorte, E.; De Rooij, N.; Popovic, R. *Journal of Magnetic Resonance* **2003,** 164, (2), 242-255.

51. Krojanski, H. G.; Lambert, J. r.; Gerikalan, Y.; Suter, D.; Hergenröder, R. *Anal Chem* **2008,** 80, (22), 8668-8672.

52. Tkac, I.; Andersen, P.; Adriany, G.; Merkle, H.; Ugurbil, K.; Gruetter, R. *Magnet Reson Med* **2001,** 46, (3), 451-456.

53. Grannell, P. K.; Mansfield, P. *Physics in medicine and biology* **1975,** 20, (3), 477-82.

54. Finch, M. J. *Libr J* **2014,** 139, (6), 12-12.

55. Ehrmann, K.; Saillen, N.; Vincent, F.; Stettler, M.; Jordan, M.; Wurm, F. M.; Besse, P. A.; Popovic, R. *Lab Chip* **2007,** 7, (3), 373-380.

56. MAGUIRE, Y.; CHUANG, I. L.; ZHANG, S.; GERSHENFELD, N. *PROCEEDINGS OF THE NATIONAL ACADEMY OF SCIENCES* **2007,** 104, (22), 9198-9203.

57. VAN BENTUM, P.; JANSSEN, J.; KENTGENS, A.; BART, J.; GARDENIERS, J. *JOURNAL OF MAGNETIC RESONANCE* **2007,** 189, (1), 104-113.

58. WONG, A.; LI, X.; MOLIN, L.; SOLARI, F.; ELENA-HERRMANN, B. N. D.; SAKELLARIOU, D. *ANAL CHEM* **2014,** 86, (12), 6064-6070.

59. SENDELBACH, S.; FINCH-GUTHRIE, P.; TRACY, M. F. *CLIN NURSE SPEC* **2012,** 26, (2), E34-E35.

60. AGUAYO, J. B.; BLACKBAND, S. J.; SCHOENIGER, J.; MATTINGLY, M. A.; HINTERMANN, M. **1986**.

61. SCHOENIGER, J.; AIKEN, N.; HSU, E.; BLACKBAND, S. *JOURNAL OF MAGNETIC RESONANCE, SERIES B* **1994,** 103, (3), 261-273.

62. BEYER, K.; KLINGENBERG, M. *BIOCHEMISTRY-US* **1983,** 22, (3), 639-45.

63. FLORENTZ, M.; GRANGER, P.; HARTEMANN, P. *APPLIED AND ENVIRONMENTAL MICROBIOLOGY* **1984,** 47, (3), 519-25.

64. FLINDT, R., *AMAZING NUMBERS IN BIOLOGY*. SPRINGER SCIENCE & BUSINESS MEDIA: 2006.

65. MORITA, Y.; OHNO, K. *JOURNAL OF MAGNETIC RESONANCE, SERIES A* **1993,** 102, (3), 344-347.

66. BOERO, G.; BOUTERFAS, M.; MASSIN, C.; VINCENT, F.; BESSE, P.-A.; POPOVIC, R.; SCHWEIGER, A. *REV. SCI. INSTRUM.* **2003,** 74, (11), 4794-4798.

67. NARKOWICZ, R.; SUTER, D.; STONIES, R. *JOURNAL OF MAGNETIC RESONANCE* **2005,** 175, (2), 275-284.

68. TWIG, Y.; DIKAROV, E.; BLANK, A. *MOL PHYS* **2013,** 111, (18-19), 2674-2682.

69. OLSON, D. L.; PECK, T. L.; WEBB, A. G.; MAGIN, R. L.; SWEEDLER, J. V. *SCIENCE* **1995,** 270, (5244), 1967-1970.

70. MASSIN, C.; BOERO, C.; VINCENT, F.; ABENHAIM, J.; BESSE, P. A.; POPOVIC, R. S. *SENSOR ACTUAT A-PHYS* **2002,** 97-8, 280-288.

71. WEBB, A. G. *J PHARMACEUT BIOMED* **2005,** 38, (5), 892-903.

72. BART, J.; KOLKMAN, A. J.; OOSTHOEK-DE VRIES, A. J.; KOCH, K.; NIEUWLAND, P. J.; JANSSEN, H.; VAN BENTUM, J.; AMPT, K. A.; RUTJES, F. P.; WIJMENGA, S. S. *J. AM. CHEM. SOC.* **2009,** 131, (14), 5014-5015.

73. KRATT, K.; BADILITA, V.; BURGER, T.; KORVINK, J.; WALLRABE, U. *J MICROMECH MICROENG* **2009,** 20, (1), 015021.

74. GRISI, M.; GUALCO, G.; BOERO, G. *REV. SCI. INSTRUM.* **2015,** 86, (4), 044703.

75. Olson, D. L.; Peck, T. L.; Webb, A. G.; Magin, R. L.; Sweedler, J. V. *Science* **1995,** 270, (5244), 1967.

76. Rogers, J. A.; Jackman, R. J.; Whitesides, G. M.; Olson, D. L.; Sweedler, J. V. *Applied Physics Letters* **1997,** 70, (18), 2464-2466.

77. Ciobanu, L.; Seeber, D.; Pennington, C. *Journal of Magnetic Resonance* **2002,** 158, (1), 178-182.

78. Malba, V.; Maxwell, R.; Evans, L. B.; Bernhardt, A. F.; Cosman, M.; Yan, K. *Biomed Microdevices* **2003,** 5, (1), 21-27.

79. Sorli, B.; Chateaux, J.; Pitaval, M.; Chahboune, H.; Favre, B.; Briguet, A.; Morin, P. *Measurement Science and Technology* **2004,** 15, (5), 877.

80. Demas, V.; Bernhardt, A.; Malba, V.; Adams, K. L.; Evans, L.; Harvey, C.; Maxwell, R. S.; Herberg, J. L. *Journal of Magnetic Resonance* **2009,** 200, (1), 56-63.

81. Sillerud, L. O.; McDowell, A. F.; Adolphi, N. L.; Serda, R. E.; Adams, D. P.; Vasile, M. J.; Alam, T. M. *Journal of Magnetic Resonance* **2006,** 181, (2), 181-190.

82. Ehrmann, K.; Saillen, N.; Vincent, F.; Stettler, M.; Jordan, M.; Wurm, F. M.; Besse, P.-A.; Popovic, R. *Lab Chip* **2007,** 7, (3), 373-380.

83. Badilita, V.; Kratt, K.; Baxan, N.; Mohmmadzadeh, M.; Burger, T.; Weber, H.; Elverfeldt, D. v.; Hennig, J.; Korvink, J. G.; Wallrabe, U. *Lab Chip* **2010,** 10, (11), 1387-1390.

84. Massin, C.; Vincent, F.; Homsy, A.; Ehrmann, K.; Boero, G.; Besse, P. A.; Daridon, A.; Verpoorte, E.; de Rooij, N. F.; Popovic, R. S. *Journal of Magnetic Resonance* **2003,** 164, (2), 242-255.

85. Wensink, H.; Benito-Lopez, F.; Hermes, D. C.; Verboom, W.; Gardeniers, H. J.; Reinhoudt, D. N.; van den Berg, A. *Lab Chip* **2005,** 5, (3), 280-284.

86. Sorli, B.; Chateaux, J. F.; Pitaval, M.; Chahboune, H.; Favre, B.; Briguet, A.; Morin, P. *Meas Sci Technol* **2004,** 15, (5), 877-880.

87. Bart, J.; Janssen, J.; Van Bentum, P.; Kentgens, A.; Gardeniers, J. *Journal of Magnetic Resonance* **2009,** 201, (2), 175-185.

88. Shtein, R. M.; Callaghan, B. C. *Diabetes* **2013,** 62, (1), 25-6.

89. Finch, G.; Yilmaz, A.; Utz, M. *Journal of Magnetic Resonance* **2016,** 262, 73-80.

90. Blank, A.; Twig, Y.; Ishay, Y. *Journal of Magnetic Resonance* **2017,** 280, 20-29.

91. Blank, A.; Suhovoy, E.; Halevy, R.; Shtirberg, L.; Harneit, W. *Phys. Chem. Chem. Phys.* **2009,** 11, (31), 6689-6699.

92. Anders, J.; Angerhofer, A.; Boer, G. *Journal of Magnetic Resonance* **2012,** 217, 19-26.

93. MATHEOUD, A. V.; GUALCO, G.; JEONG, M.; ZIVKOVIC, I.; BRUGGER, J.; RØNNOW, H. M.; ANDERS, J.; BOERO, G. *JOURNAL OF MAGNETIC RESONANCE* **2017,** 278, 113-121.

94. ABRAGAM, A. *CC/PHYS CHEM EARTH* **1982**, (30), 18-18.

95. STEINHAUSER, M.; ERNST, B.; IBALD, K. W. *J EXP PSYCHOL LEARN* **2017,** 41, (4), 653-659.

96. KLINKHAMMER-SCHALKE, M.; KOLLER, M.; STEINGER, B.; EHRET, C.; ERNST, B.; WYATT, J. C.; HOFSTADTER, F.; LORENZ, W.; GRP, R. Q. S. *BRIT J CANCER* **2012,** 106, (5), 826-838.

97. FISCHER, E.; JELITTE, M.; VOGEL, H.; ERNST, B.; SCHWAB, M. *Z GERONTOL GERIATR* **2010,** 43, 93-93.

98. TWIG, Y.; DIKAROV, E.; HUTCHISON, W. D.; BLANK, A. *REV. SCI. INSTRUM.* **2011,** 82, (7), 076105.

99. ARTZI, Y.; TWIG, Y.; BLANK, A. *APPLIED PHYSICS LETTERS* **2015,** 106, (8), 084104.

100. SKIBBE, U.; CHRISTELLER, J. T.; ECCLES, C. D.; LAING, W. A.; CALLAGHAN, P. T. *MAGNETIC RESONANCE IMAGING* **1995,** 13, (3), 471-9.

101. YALCIN, T.; BOERO, G. *REV. SCI. INSTRUM.* **2008,** 79, (9).

102. GUALCO, G.; ANDERS, J.; SIENKIEWICZ, A.; ALBERTI, S.; FORRÓ, L.; BOERO, G. *JOURNAL OF MAGNETIC RESONANCE* **2014,** 247, 96-103.

103. D.I. HOULT, R. E. R. *JOURNAL OF MAGNETIC RESONANCE* **1976,** 24, 71-85.

104. ANTZUTKIN, O. N. *MAGNETIC RESONANCE IN CHEMISTRY : MRC* **2004,** 42, (2), 231-46.

105. A, A. *OXFORD UNIVERSITY PRESS* **1961**.

106. SAKAKIBARA, D.; SASAKI, A.; IKEYA, T.; HAMATSU, J.; HANASHIMA, T.; MISHIMA, M.; YOSHIMASU, M.; HAYASHI, N.; MIKAWA, T.; WÄLCHLI, M. *NATURE* **2009,** 458, (7234), 102-105.

107. LEUSCHNER, R. G.; LILLFORD, P. J. *INTERNATIONAL JOURNAL OF FOOD MICROBIOLOGY* **2001,** 63, (1-2), 35-50.

108. BREHM-STECHER, B. F.; JOHNSON, E. A. *MICROBIOLOGY AND MOLECULAR BIOLOGY REVIEWS* **2004,** 68, (3), 538-559.

109. AGUAYO, J. B.; BLACKBAND, S. J.; SCHOENIGER, J.; MATTINGLY, M. A.; HINTERMANN, M. *NATURE* **1986,** 322, (6075), 190-191.

110. SEHY, J. V.; ACKERMAN, J. J.; NEIL, J. J. *MAGNET RESON MED* **2001,** 46, (5), 900-906.

111. DANG, Q. Q.; DEDIEU, J. C.; DOUSTE-BLAZY, L. *BIOCHIMICA ET BIOPHYSICA ACTA* **1980,** 597, (3), 464-76.

112. Grisi, M.; Vincent, F.; Volpe, B.; Guidetti, R.; Harris, N.; Beck, A.; Boero, G. *Scientific Reports* **2017,** 7.

113. Lee, J. N.; Park, C.; Whitesides, G. M. *Anal Chem* **2003,** 75, (23), 6544-6554.

114. Carlier, J.; Arscott, S.; Thomy, V.; Fourrier, J.; Caron, F.; Camart, J.; Druon, C.; Tabourier, P. *J Micromech Microeng* **2004,** 14, (4), 619.

115. Blanco, F.; Agirregabiria, M.; Garcia, J.; Berganzo, J.; Tijero, M.; Arroyo, M.; Ruano, J.; Aramburu, I.; Mayora, K. *J Micromech Microeng* **2004,** 14, (7), 1047.

116. Chuang, Y.-J.; Tseng, F.-G.; Cheng, J.-H.; Lin, W.-K. *Sensors and Actuators A: Physical* **2003,** 103, (1), 64-69.

117. Lloyd, S. G.; Zeng, H. D.; Wang, P. P.; Chatham, J. C. *Magnet Reson Med* **2004,** 51, (6), 1279-1282.

118. Bart, J.; Janssen, J. W. G.; van Bentum, P. J. M.; Kentgens, A. P. M.; Gardeniers, J. G. E. *Journal of Magnetic Resonance* **2009,** 201, (2), 175-185.

119. Spengler, N.; Höfflin, J.; Moazenzadeh, A.; Mager, D.; MacKinnon, N.; Badilita, V.; Wallrabe, U.; Korvink, J. G. *PloS one* **2016,** 11, (1), e0146384.

120. Xia, Y.; Jeffrey, K. R.; Callaghan, P. T. *Magnetic resonance imaging* **1992,** 10, (3), 411-26.

121. Lee, S.-C.; Cho, J.-H.; Mietchen, D.; Kim, Y.-S.; Hong, K. S.; Lee, C.; Kang, D.; Park, K. D.; Choi, B.-S.; Cheong, C. *Biophys J* **2006,** 90, (5), 1797-1803.

122. Jayasundar, R.; Ayyar, S.; Raghunathan, P. *Magnetic resonance imaging* **1997,** 15, (6), 709-717.

123. Brecker, L.; Weber, H.; Griengl, H.; Ribbons, D. W. *Microbiology* **1999,** 145, (12), 3389-3397.

124. Spencer, R. G. *Concept Magn Reson A* **2010,** 36, (5), 255-265.

125. Grisi, M.; Volpe, B.; Guidetti, R.; Harris, N.; Boero, G. *arXiv preprint arXiv:1511.06719* **2015**.

126. Devreker, F.; Englert, Y. *European Journal of Obstetrics & Gynecology and Reproductive Biology* **2000,** 92, (1), 51-56.

127. Ablett, S.; Barratt, M.; Franks, F. *J Solution Chem* **1975,** 4, (9), 797-807.

128. Hagen, W. R., *Biomolecular EPR spectroscopy*. CRC press: 2008.

129. Edwards, D. T.; Ma, Z.; Meade, T. J.; Goldfarb, D.; Han, S.; Sherwin, M. S. *Phys. Chem. Chem. Phys.* **2013,** 15, (27), 11313-11326.

130. Callaghan, P. T.; Clark, C. J.; Forde, L. C. *Biophysical chemistry* **1994,** 50, (1-2), 225-35.

131. ITO, A.; SHINKAI, M.; HONDA, H.; KOBAYASHI, T. *JOURNAL OF BIOSCIENCE AND BIOENGINEERING* **2005,** 100, (1), 1-11.

132. GIJS, M. A. *MICROFLUIDICS AND NANOFLUIDICS* **2004,** 1, (1), 22-40.

133. SIDERIS, C.; HAJIMIRI, A. *BIOMEDICAL CIRCUITS AND SYSTEMS, IEEE TRANSACTIONS ON* **2013,** 7, (6), 773-784.

134. WANG, H.; KOSAI, S.; SIDERIS, C.; HAJIMIRI, A. IN *AN ULTRASENSITIVE CMOS MAGNETIC BIOSENSOR ARRAY WITH CORRELATED DOUBLE COUNTING NOISE SUPPRESSION*, MICROWAVE SYMPOSIUM DIGEST (MTT), 2010 IEEE MTT-S INTERNATIONAL, 2010; IEEE: PP 616-619.

135. BASELT, D. R.; LEE, G. U.; NATESAN, M.; METZGER, S. W.; SHEEHAN, P. E.; COLTON, R. J. *BIOSENSORS AND BIOELECTRONICS* **1998,** 13, (7), 731-739.

136. BESSE, P.-A.; BOERO, G.; DEMIERRE, M.; POTT, V.; POPOVIC, R. *APPLIED PHYSICS LETTERS* **2002,** 80, (22), 4199-4201.

137. LANY, M.; BOERO, G.; POPOVIC, R. *REV. SCI. INSTRUM.* **2005,** 76, (8), 084301.

138. CHATTERJEE, E.; MARR, T.; DHAGAT, P.; REMCHO, V. T. *SENSORS AND ACTUATORS B: CHEMICAL* **2011,** 156, (2), 651-656.

139. FANNIN, P.; COHEN-TANNOUDJI, L.; BERTRAND, E.; GIANNITSIS, A.; MAC OIREACHTAIGH, C.; BIBETTE, J. *JOURNAL OF MAGNETISM AND MAGNETIC MATERIALS* **2006,** 303, (1), 147-152.

140. WANG, H. *MICROWAVE MAGAZINE, IEEE* **2013,** 14, (5), 110-130.

141. RUGAR, D.; BUDAKIAN, R.; MAMIN, H. J.; CHUI, B. W. *NATURE* **2004,** 430, (6997), 329-332.

142. ERNST, B. E. *DUNS BUS MONTH* **1983,** 121, (1), 5-5.

143. PUGLIESE, P. T.; WHITLOCK, C. M.; ERNST, B.; WILLIAMS, R. R. *ARCH ENVIRON HEALTH* **1968,** 16, (3), 374-&.

144. FOLLETTE, W. C.; CALLAGHAN, G. M. *PSYCHOTHER RES* **1996,** 6, (2), 133-143.

145. DURKAN, C.; WELLAND, M. *APPLIED PHYSICS LETTERS* **2002,** 80, (3), 458-460.

146. RONDIN, L.; TETIENNE, J.; HINGANT, T.; ROCH, J.; MALETINSKY, P.; JACQUES, V. *REPORTS ON PROGRESS IN PHYSICS* **2014,** 77, (5), 056503.

147. MAZE, J. R.; STANWIX, P. L.; HODGES, J. S.; HONG, S.; TAYLOR, J. M.; CAPPELLARO, P.; JIANG, L.; DUTT, M. V. G.; TOGAN, E.; ZIBROV, A. S.; YACOBY, A.; WALSWORTH, R. L.; LUKIN, M. D. *NATURE* **2008,** 455, (7213), 644-U41.

148. THAHA, K. A.; VARMA, R. L.; NAIR, M. G.; SAM JOSEPH, V. G.; KRISHNAN, U. *JOURNAL OF ENDODONTICS* **2017,** 43, (1), 135-140.

149. Ernst, B. J. G.; Steinhauser, M. *Psychophysiology* **2009,** 46, S63-S63.

150. Debess, J. E.; Ernst, B.; Ewertz, M. *Psycho-Oncology* **2006,** 15, (2), S217-S218.

151. Jorzick, J.; Demokritov, S.; Hillebrands, B.; Bartenlian, B.; Chappert, C.; Decanini, D.; Rousseaux, F.; Cambril, E. *Applied Physics Letters* **1999,** 75, (24), 3859-3861.

152. Wang, Z.; Kuok, M.; Ng, S.; Lockwood, D.; Cottam, M.; Nielsch, K.; Wehrspohn, R.; Gösele, U. *Physical review letters* **2002,** 89, (2), 027201.

153. Kostylev, M.; Ding, J.; Ivanov, E.; Samarin, S.; Adeyeye, A. *Journal of Applied Physics* **2014,** 115, (17), 173903.

154. Pechan, M. J.; Yu, C.; Owen, D.; Katine, J.; Folks, L.; Carey, M. *Journal of applied physics* **2006,** 99, (8), 08C702.

155. Safar, G. A.; Malachias, A.; Magalhaes-Paniago, R.; Martins, D. C.; Idemori, Y. M. *Physical chemistry chemical physics : PCCP* **2013,** 15, (47), 20691-7.

156. Kostylev, M.; Magaraggia, R.; Ogrin, F. Y.; Sirotkin, E.; Mescheryakov, V. F.; Ross, N.; Stamps, R. L. *IEEE Transactions on Magnetics* **2008,** 44, (11), 2741-2744.

157. Hahn, C.; Naletov, V.; de Loubens, G.; Klein, O.; Kelly, O. d. A.; Anane, A.; Bernard, R.; Jacquet, E.; Bortolotti, P.; Cros, V. *Applied Physics Letters* **2014,** 104, (15), 152410.

158. Bray, J. M.; Petrone, C.; Filiaggi, M.; Beyea, S. D. *Solid state nuclear magnetic resonance* **2007,** 32, (4), 118-28.

159. Meckenstock, R.; Spoddig, D.; Dietzel, D.; Pelzl, J.; Bucher, J. *Review of scientific instruments* **2003,** 74, (1), 789-791.

160. Straadt, I. K.; Rasmussen, M.; Andersen, H. J.; Bertram, H. C. *Meat science* **2007,** 75, (4), 687-95.

161. Vogt, K.; Schultheiss, H.; Jain, S.; Pearson, J.; Hoffmann, A.; Bader, S.; Hillebrands, B. *Applied Physics Letters* **2012,** 101, (4), 042410.

162. Vauclare, P.; Bligny, R.; Gout, E.; De Meuron, V.; Widmer, F. *Planta* **2010,** 231, (6), 1495-504.

163. Chen, B.; Tycko, R. *Protein science : a publication of the Protein Society* **2010,** 19, (4), 716-30.

164. Hertel, R.; Wulfhekel, W.; Kirschner, J. *Physical review letters* **2004,** 93, (25), 257202.

165. Xia, Y.; Callaghan, P. T. *Magn Reson Med* **1992,** 23, (1), 138-53.

166. Harris, R. J.; Sederman, A. J.; Mantle, M. D.; Crawshaw, J.; Johns, M. L. *Magnetic resonance imaging* **2005,** 23, (2), 355-7.

167. Li, S.; Zhang, W.; Ding, J.; Pearson, J. E.; Novosad, V.; Hoffmann, A. *Nanoscale* **2016,** 8, (1), 388-394.

168. Goto, T.; Onbaşli, M. C.; Ross, C. *Optics express* **2012,** 20, (27), 28507-28517.

169. Bi, L.; Hu, J.; Kimerling, L.; Ross, C. In *Fabrication and characterization of As2S3/Y3Fe5O12 and Y3Fe5O12/SOI strip-loaded waveguides for integrated optical isolator applications*, OPTO, 2010; International Society for Optics and Photonics: pp 760406-760406-10.

170. Kumar, N.; Prasad, S.; Misra, D.; Venkataramani, N.; Bohra, M.; Krishnan, R. *Journal of Magnetism and Magnetic Materials* **2008,** 320, (18), 2233-2236.

171. Kumar, N.; Misra, D.; Venkataramani, N.; Prasad, S.; Krishnan, R. *Journal of Magnetism and Magnetic Materials* **2004,** 272, E899-E900.

172. Lee, H.; Sun, E.; Ham, D.; Weissleder, R. *Nat. Med.* **2008,** 14, (8), 869-874.

Enrica Montinaro +41-78-976-53-40 enrica.montinaro@epfl.ch

Curriculum vitae

Education

2013-2017 – PhD in Microelectronic and Microsystems,
EPFL, Lausanne, Switzerland

2010-2012 – MSc in Micro and Nano Technologies for Integrated Systems,
POLITO, Turin, Italy; INPG, Grenoble, France; EPFL, Lausanne, Switzerland

2007-2010 – BSc in Physics Engineering
POLITO, Turin, Italy

Publications

3D printed microchannels for sub-nL NMR spectroscopy,
E. Montinaro, M. Grisi et al. arXiv preprint: 1707.05500 (2017)

Conferences

Magnetic beads sensing by ferromagnetic resonance miniaturized detector
E, Montinaro. J. Brugger et al. *MicroTAS*, Dublin, Ireland (2016)

Nuclear magnetic resonance spectroscopy of subnanoliter samples by a single chip detector and microfluidic channels
E, Montinaro. M. Grisi et al. *Latsis*, Lausanne, Switzerland (2016)

Wafer scale fabrication of 3D inlets in nanofluidic devices
E. Montinaro, I. Fernandez-Cuesta et al. *NNT*, Napa, California (2012)

Sensing with 30 nm nanochannels with plasmonic bowtie nanoantenna
I. Fernandez-Cuesta, E. Montinaro et al. *MNE*, Toulouse, France (2012)